

**FIRST PRINCIPLES STUDY OF STRUCTURAL, ELECTRONIC,
OPTICAL, AND ELECTRON TRANSPORT PROPERTIES OF
NOVEL HYBRID MONOLAYERS $\text{Si}_x\text{Ge}_y\text{Sn}_{1-x-y}$ WITH NH_3
SENSING APPLICATION**

A thesis submitted in partial fulfillment of the requirement for the degree
of
MASTER OF SCIENCE IN ELECTRICAL AND ELECTRONIC ENGINEERING

by

Touhid Ahmed

STUDENT NUMBER: 1018062224 P



Department of Electrical and Electronic Engineering
Bangladesh University of Engineering and Technology

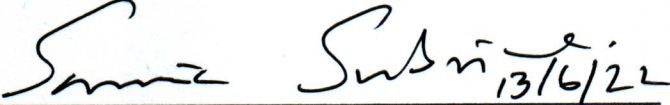
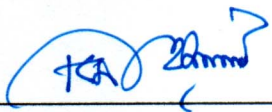
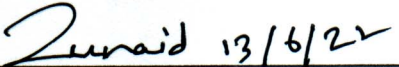
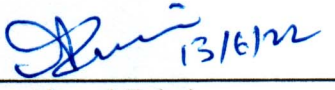
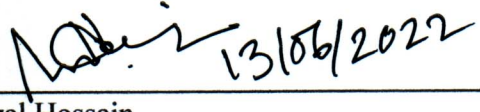
Dhaka-1205

June, 2022

Certification

The thesis titled “FIRST PRINCIPLES STUDY OF STRUCTURAL, ELECTRONIC, OPTICAL, AND ELECTRON TRANSPORT PROPERTIES OF NOVEL HYBRID MONOLAYERS, $\text{Si}_x\text{Ge}_y\text{Sn}_{1-x-y}$ WITH NH_3 SENSING APPLICATION” submitted by Touhid Ahmed, Roll No.: 1018062224 P, Session: October, 2018, has been accepted as satisfactory in partial fulfillment of the requirement for the degree of Master of Science in Electrical and Electronic Engineering on June 13, 2022.

BOARD OF EXAMINERS

1. 
13/6/22
Chairman
(Supervisor)
Dr. Samia Subrina
Professor
Department of EEE, BUET, Dhaka
2. 
Dr. Md. Kamrul Hasan
Professor and Head
Department of EEE, BUET, Dhaka
Member
(Ex- officio)
3. 
13/6/22
Member
Dr. Md. Zunaid Baten
Associate Professor
Department of EEE, BUET, Dhaka
4. 
13/6/22
Member
Dr. Ahmed Zubair
Assistant Professor
Department of EEE, BUET, Dhaka
5. 
13/06/2022
Member
(External)
Dr. M. Mofazzal Hossain
Professor
Electrical and Electronic Engineering, University of
Liberal Arts Bangladesh (ULAB), Dhaka

DECLARATION

This thesis, in whole or in part, has not been submitted anywhere for the granting of any degree, and all sources have been acknowledged.

Signature of the Candidate

Touhid Ahmed

Touhid Ahmed
(Student Number: 1018062224 P)

To my beloved parents

Acknowledgement

I want to express my gratitude to Almighty for providing me with the strength, endurance, and tenacity required to complete my thesis.

Then, I would like to convey my heartfelt thanks to Dr. Samia Subrina, Professor, Department of Electrical and Electronic Engineering, BUET, for her unwavering support, insightful guidance, and encouragement during the course of my thesis. I also want to express my sincere gratitude to the other members of the thesis committee for taking the time to review my work.

Furthermore, I would like to extend my sincere appreciation to my beloved family and friends for their unconditional support, trust, and encouragement.

Abstract

At the nanoscale, two-dimensional (2D) materials are showing great promise in improving device mobility, on current density, on/off current ratio, subthreshold swing, and contact resistance, etc. Furthermore, contemporary three-dimensional integration of logic, memory, and optoelectronic devices into a single nanoscaled chip requires 2D materials for transistor channel, thermal insulator, light emitters, and photodetectors etc. Since the emergence of graphene, researchers have been investigating novel 2D materials that can combine structural stability with superior electronic, thermal and optical properties. Group-IV elemental monolayers (graphene, silicene, germanene, and stanene) offer many fascinating characteristics such as tunable energy bandgap, very high charge carrier mobility, superconductivity, enhanced optical conductivity. However, these materials have limited their application in digital electronics due to their semimetallic property. Other two-dimensional materials have been studied, including transition metal dichalcogenides, hexagonal boron nitrides, and phosphorene, but they do not surpass graphene in terms of other electrical, thermal, and optical characteristics. Stable two-dimensional materials with graphene-like characteristics and a considerable energy bandgap are of great scientific interest. In this work, the structural, electronic, optical, and electron transport properties of three different atomically thin novel hybrid monolayers comprising of Si, Ge, and Sn atoms with varying proportions are studied using first principles calculations within the framework of density functional theory that combine superior electronic and optical properties with considerable energy bandgap. The fabrication of similar hybrid materials is practically realizable but the study of different properties of these novel monolayers is yet to explore. The proposed hybrid buckled honeycomb monolayers with sp^2 - sp^3 like orbital hybridization, are mechanically and dynamically stable, confirmed by the analysis of in-plane elastic constants, phonon dispersion curve and cohesive energy of the monolayers. The electronic bandstructures of these hybrid 2D monolayers, namely $Ge_{0.25}Sn_{0.25}Si_{0.50}$, $Si_{0.25}Ge_{0.25}Sn_{0.50}$, and $Sn_{0.25}Si_{0.25}Ge_{0.50}$ show considerable direct energy bandgap ranging from 120 meV to 283.8 meV while preserving the linear energy-momentum relation at the K point of the Brillouin zone. The calculated significantly low effective mass ($0.063 \times m_0 - 0.101 \times m_0$), where m_0 is the rest mass of electron, and very high acoustic phonon limited mobility ($\sim 10^6 \text{ cm}^2 \text{ V}^{-1} \text{ s}^{-1}$) of the charge carriers inside the hybrid monolayers ensure the presence of relativistic-massless Dirac fermion. In order to further

investigate the electronic properties, we have calculated atom projected density of states and differential charge density. Optical properties e.g. dielectric function, electron loss function, absorption coefficient, refractive index, reflectivity, and optical conductivity are also explored for parallelly and perpendicularly polarized incident light. These hybrid monolayers show anisotropic optical response for parallel and perpendicular polarization as a function of frequency of the incident light. Polarization tunable plasma frequency, high absorption coefficient ($\sim 10^4 \text{ cm}^{-1}$) over a wide range of frequency, high refractive indices (~ 1.8) suggest these hybrid monolayers as potential candidates for optoelectronic applications. Three different armchair nanoribbons have been designed using these novel monolayers to study the effect of the adsorption of NH_3 molecules on these hybrid nanoribbons. Calculated electron transport properties ensure the applications of these nanoribbons as NH_3 sensor at the molecular level. Electron transport properties are also investigated in the presence of point defects to understand the effect of defects on the transport properties of these nanoribbons. Thus, these results suggest that the proposed $\text{Si}_x\text{Ge}_y\text{Sn}_{1-x-y}$ hybrid monolayers can be a potential candidate for nanoelectronics, optoelectronics and, sensor-based applications.

Table of Contents

Abstract.....	vi
List of Tables.....	xi
List of Figures.....	xii
Abbreviations of Technical Symbols and Terms.....	xv
CHAPTER 1 Introduction.....	1
1.1 Preface.....	1
1.2 Literature Review.....	3
1.3 Thesis Objectives.....	6
1.4 Thesis Outline.....	7
CHAPTER 2 Theoretical Foundation.....	8
2.1 Density Functional Theory.....	8
2.1.1 Schrödinger Equation for Many-Body systems.....	8
2.1.2 Born-Oppenheimer Approximation.....	10
2.1.3 Hohenberg-Kohn Theory.....	11
2.1.4 Kohn-Sham Equations.....	12
2.1.5 Exchange-Correlational Functionals.....	14
2.1.6 Plane-wave Basis Sets.....	17
2.1.7 Projected Augmented Wave Basis and Pseudo-Potentials.....	18
2.1.8 Ultrasoft Pseudo-Potentials.....	20
2.1.9 Electronic Minimization.....	20
2.1.10 Variable Cell Structural Optimization.....	21
2.1.11 Brillouin Zone sampling.....	22
2.1.12 Deformation Potential Theory.....	22
2.1.13 Non-Equilibrium Green's Function.....	23
2.2 Electronic and Optical Properties.....	25

2.2.1	Electronic Band Structure	25
2.2.2	Density of States and Atom Projected Density of States.....	25
2.2.3	Charge Density.....	26
2.2.4	Spin-Orbit Coupling (SOC).....	26
2.2.5	Effective Mass of the charge carriers.....	27
2.2.6	Acoustic phonon limited charge carrier mobility	28
2.2.7	Optical Properties.....	28
2.2.8	Transmission function and Current-Voltage characteristics.....	29
CHAPTER 3 Structural and Computational Details.....		30
3.1	Structural Details.....	30
3.1.1	$\text{Si}_x\text{Ge}_y\text{Sn}_{1-x-y}$ monolayers	30
3.2	Computational Methodology.....	31
3.2.1	DFT simulation tools and parameters	31
3.2.2	Structure Optimization.....	33
3.2.3	In-Plane Elastic Constants	34
3.2.4	Cohesive Energy	35
3.2.5	Phonon Dispersion Calculation.....	35
3.2.6	Band Structure Calculation	36
3.2.7	Density of States and Atom Projected Density of States.....	36
3.2.8	Differential Charge Density.....	36
3.2.9	Spin-Orbit Coupling (SOC) incorporation.....	37
3.2.10	Effective Mass of the charge carriers.....	37
3.2.11	Acoustic phonon limited mobility of charge carriers	38
3.2.12	Optical Properties.....	39
3.2.13	Electron Transport Properties	40
CHAPTER 4 Results and Discussion.....		41
4.1	Geometrically Optimized Structures.....	41

4.2	Mechanical and dynamic stability	42
4.2.1	In-Plane Elastic Constants	42
4.2.2	Phonon Dispersion Curves.....	43
4.2.3	Cohesive Energy	44
4.3	Electronic Properties	45
4.3.1	Energy Band Structure	45
4.3.2	Effective Mass of the Charge Carrier	48
4.3.3	Acoustic Phonon limited Charge Carrier	48
4.3.4	Density of States and Atom Projected Density of States.....	50
4.3.5	Differential Charge Density	52
4.4	Optical Properties	54
4.4.1	Real part of Complex Dielectric Function and Electron Energy Loss Function 54	
4.4.2	Imaginary part of Complex Dielectric Function and Absorption Coefficient 57	
4.4.3	Complex Refractive Index	60
4.4.4	Reflectivity.....	62
4.4.5	Optical Conductivity	63
4.5	Electron Transport Properties and Sensing Applications.....	65
4.5.1	NH ₃ Sensing.....	66
4.5.2	Effects of Point Defect.....	72
	CHAPTER 5 Conclusion.....	75
5.1	Summary	75
5.2	Scope for Future Works	76
	List of References.....	77

List of Tables

Table 3.1: Used parameters and their values in DFT calculation.....	33
Table 3.2: Used parameters and their values in for structure minimization.....	34
Table 4.1: Structural properties of Novel Hybrid monolayers of Si, Ge and Sn and comparison with monolayer silicene, germanene, stanene, and graphene: Lattice constant (Å), bond length (Å), buckling height (Å), elastic constants, and cohesive energy (eV/ unit cell).....	49
Table 4.2: Electronic properties of Novel Hybrid monolayers of Si, Ge and Sn and comparison with similar 2D materials: Energy bandgap (with and without SOC), Energy band splitting due to SOC, effective mass and acoustic phonon limited mobility of the charge carrier.....	48
Table 4.3: Real part of dielectric function, peak in Eloss function, plasma frequency, forbidden region and in novel hybrid monolayers of Si, Ge and Sn	56
Table 4.4: Imaginary part of dielectric function, absorption coefficient and Static Refractive index of Novel Hybrid monolayers of Si, Ge and Sn.....	59
Table 4.5: Value of maximum reflectivity and frequency at which maximum reflection occurs, Positions of peaks in Real part of complex conductivity and Zero crossings in Imaginary part of complex conductivity in Novel Hybrid monolayers of Si, Ge and Sn..	65

List of Figures

Figure 3.1: Top and side view of monolayer hybrid structures of Si, Ge and Sn. Fig. 3.1(a), (b), (c) represent top views and Fig.3.1(d), (e), (f) represents side views of $\text{Ge}_{0.25}\text{Sn}_{0.25}\text{Si}_{0.50}$, $\text{Si}_{0.25}\text{Ge}_{0.25}\text{Sn}_{0.50}$ and $\text{Sn}_{0.25}\text{Si}_{0.25}\text{Ge}_{0.50}$ respectively. The black hexagons represent the unit cells.....31

Figure 3.2: Flowchart of computational method.....32

Figure 3.3: A visual representation of parabolic approximation of non-parabolic band structure for performing the effective mass calculation.....38

Figure 4.1: Phonon dispersion curves of monolayer hybrids of Si, Ge and Sn- (a) $\text{Ge}_{0.25}\text{Sn}_{0.25}\text{Si}_{0.50}$, (b) $\text{Si}_{0.25}\text{Ge}_{0.25}\text{Sn}_{0.50}$ and (c) $\text{Sn}_{0.25}\text{Si}_{0.25}\text{Ge}_{0.50}$ respectively.....44

Figure 4.2: Electronic Band Structure of $\text{Ge}_{0.25}\text{Sn}_{0.25}\text{Si}_{0.50}$ (a) without SOC, (b) with SOC, (c) magnified view at K point; of $\text{Si}_{0.25}\text{Ge}_{0.25}\text{Sn}_{0.50}$ (d) without SOC, (e) with SOC (f) magnified view at K point; of $\text{Sn}_{0.25}\text{Si}_{0.25}\text{Ge}_{0.50}$ (g) without SOC, (h) with SOC, (i) magnified view at K point.....47

Figure 4.3: Change of CBM and VBM as a function of strain for (a) $\text{Ge}_{0.25}\text{Sn}_{0.25}\text{Si}_{0.50}$, (b) $\text{Si}_{0.25}\text{Ge}_{0.25}\text{Sn}_{0.50}$, (c) $\text{Sn}_{0.25}\text{Si}_{0.25}\text{Ge}_{0.50}$ and Shift in energy as a function of strain for (d) $\text{Ge}_{0.25}\text{Sn}_{0.25}\text{Si}_{0.50}$, (e) $\text{Si}_{0.25}\text{Ge}_{0.25}\text{Sn}_{0.50}$, (f) $\text{Sn}_{0.25}\text{Si}_{0.25}\text{Ge}_{0.50}$ hybrid monolayer.....50

Figure 4.4: Atom projected Density of states as a function of energy for (a) $\text{Ge}_{0.25}\text{Sn}_{0.25}\text{Si}_{0.50}$, (b) $\text{Si}_{0.25}\text{Ge}_{0.25}\text{Sn}_{0.50}$, and (c) $\text{Sn}_{0.25}\text{Si}_{0.25}\text{Ge}_{0.50}$ hybrid monolayer.....51

Figure 4.5: Top (top) and side (bottom) view of Differential Charge Density of (a) $\text{Ge}_{0.25}\text{Sn}_{0.25}\text{Si}_{0.50}$, (b) $\text{Si}_{0.25}\text{Ge}_{0.25}\text{Sn}_{0.50}$, and (c) $\text{Sn}_{0.25}\text{Si}_{0.25}\text{Ge}_{0.50}$ hybrid monolayer.....53

Figure 4.6: Real Part of Dielectric Function when Electromagnetic field is polarized in (a) 001(\perp) and (b) 100(\parallel) direction of Monolayer Hybrid of Si, Ge and Sn.....56

Figure 4.7: Electron Loss Function when Electromagnetic field is polarized in (e) 001(\perp) and (f) 100(\parallel) direction, of Monolayer Hybrid of Si, Ge and Sn.....57

Figure 4.8: Imaginary part of Dielectric Function when Electromagnetic field is polarized in (a) 001(\perp) and (b) 100(\parallel) direction, of Monolayer Hybrid of Si, Ge and Sn.....	58
Figure 4.9: Absorption coefficient when Electromagnetic field is polarized in (a) 001(\perp) and (b) 100(\parallel) direction, Log of Absorption coefficient when Electromagnetic field is polarized in (c) 001(\perp) and (d) 100(\parallel) direction, of Monolayer Hybrid of Si, Ge and Sn.....	58
Figure 4.10: Real part of Refractive index when Electromagnetic field is polarized in (a) 001(\perp) and (b) 100(\parallel) direction, (c) Birefringence characteristics of Monolayer Hybrid of Si, Ge and Sn.....	60
Figure 4.11: Imaginary part of Refractive index when Electromagnetic field is polarized in (a) 001(\perp) and (b) 100(\parallel) direction, of Monolayer Hybrid of Si, Ge and Sn.....	61
Figure 4.12: Reflectivity when Electromagnetic field is polarized in (a) 001(\perp) and (b) 100(\parallel) direction, of Monolayer Hybrid of Si, Ge and Sn.....	63
Figure 4.13: Real part of Optical Conductivity when Electromagnetic field is polarized in (a) 001(\perp) and (b) 100(\parallel) direction of Monolayer Hybrid of Si, Ge and Sn.....	64
Figure 4.14: Imaginary part of Optical Conductivity when Electromagnetic field is polarized in (a) 001(\perp) and (b) 100(\parallel) direction, of Monolayer Hybrid of Si, Ge and Sn.....	64
Figure 4.15: Top and side views of the $\text{Ge}_{0.25}\text{Sn}_{0.25}\text{Si}_{0.50}$ (a) pristine (b) with NH_3 molecule and; top and side views of the $\text{Si}_{0.25}\text{Ge}_{0.25}\text{Sn}_{0.50}$ (c) pristine (d) with NH_3 molecule; top and side views of the $\text{Sn}_{0.25}\text{Si}_{0.25}\text{Ge}_{0.50}$ ANR electron transport device (e) pristine (f) with NH_3 molecule.....	66
Figure 4.16: Top and side views of the Differential Charge Density in the presence of NH_3 molecule of (a) $\text{Ge}_{0.25}\text{Sn}_{0.25}\text{Si}_{0.50}$ (b) $\text{Si}_{0.25}\text{Ge}_{0.25}\text{Sn}_{0.50}$, (c) $\text{Sn}_{0.25}\text{Si}_{0.25}\text{Ge}_{0.50}$ ANR electron transport device.....	67
Figure 4.17: I-V characteristics of (a) $\text{Ge}_{0.25}\text{Sn}_{0.25}\text{Si}_{0.50}$, (b) $\text{Si}_{0.25}\text{Ge}_{0.25}\text{Sn}_{0.50}$, (c) $\text{Sn}_{0.25}\text{Si}_{0.25}\text{Ge}_{0.50}$ ANR	68
Figure 4.18: Conductance plot of (a) $\text{Ge}_{0.25}\text{Sn}_{0.25}\text{Si}_{0.50}$, (b) $\text{Si}_{0.25}\text{Ge}_{0.25}\text{Sn}_{0.50}$, (c) $\text{Sn}_{0.25}\text{Si}_{0.25}\text{Ge}_{0.50}$	69

Figure 4.19: Transmission Function of (a) $\text{Ge}_{0.25}\text{Sn}_{0.25}\text{Si}_{0.50}$, (b) $\text{Si}_{0.25}\text{Ge}_{0.25}\text{Sn}_{0.50}$, (c) $\text{Sn}_{0.25}\text{Si}_{0.25}\text{Ge}_{0.50}$ electron transport device pristine (blue) and with NH_3 molecules (red).70

Figure 4.20: ΔI -V characteristics of (a) $\text{Ge}_{0.25}\text{Sn}_{0.25}\text{Si}_{0.50}$, (b) $\text{Si}_{0.25}\text{Ge}_{0.25}\text{Sn}_{0.50}$, (c) $\text{Sn}_{0.25}\text{Si}_{0.25}\text{Ge}_{0.50}$ ANR in the presence of NH_3 molecules.....71

Figure 4.21: Optical absorption in log scale of (a) $\text{Ge}_{0.25}\text{Sn}_{0.25}\text{Si}_{0.50}$, (b) $\text{Si}_{0.25}\text{Ge}_{0.25}\text{Sn}_{0.50}$, (c) $\text{Sn}_{0.25}\text{Si}_{0.25}\text{Ge}_{0.50}$ monolayer for perpendicular polarization and (d) $\text{Ge}_{0.25}\text{Sn}_{0.25}\text{Si}_{0.50}$, (e) $\text{Si}_{0.25}\text{Ge}_{0.25}\text{Sn}_{0.50}$, (f) $\text{Sn}_{0.25}\text{Si}_{0.25}\text{Ge}_{0.50}$ monolayer for parallel polarization of incident light.72

Figure 4.22: (a) $\text{Ge}_{0.25}\text{Sn}_{0.25}\text{Si}_{0.50}$, (b) $\text{Si}_{0.25}\text{Ge}_{0.25}\text{Sn}_{0.50}$, (c) $\text{Sn}_{0.25}\text{Si}_{0.25}\text{Ge}_{0.50}$ electron transport devices.....73

Figure 4.23: I-V characteristics of (a) $\text{Ge}_{0.25}\text{Sn}_{0.25}\text{Si}_{0.50}$, (b) $\text{Si}_{0.25}\text{Ge}_{0.25}\text{Sn}_{0.50}$, (c) $\text{Sn}_{0.25}\text{Si}_{0.25}\text{Ge}_{0.50}$ ANR; , and Transmission Function of (d) $\text{Ge}_{0.25}\text{Sn}_{0.25}\text{Si}_{0.50}$, (e) $\text{Si}_{0.25}\text{Ge}_{0.25}\text{Sn}_{0.50}$, (f) $\text{Sn}_{0.25}\text{Si}_{0.25}\text{Ge}_{0.50}$ electron transport device pristine (blue) and with point defect (red).....74

Abbreviations of Technical Symbols and Terms

2D	Two Dimensional
BO	Born–Oppenheimer
BFGS	Broyden–Fletcher–Goldfarb–Shanno
BZ	Brilloin Zone
CASTEP	Cambridge Serial Total Energy
CBM	Conduction Band Minima
CVD	Chemical Vapor Deposition
DCD	Differential Charge Density
DOS	Density of States
EELS	Electron Energy Loss
eV	electron Volt
GGA	Generalized Gradient Approximation
h-BN	hexagonal Boron Nitride
HSE	Heyd–Scuseria–Ernzerhof
LDA	Local Density Approximation
MBE	Molecular Beam Epitaxy
NEGF	Non-Equilibrium Green’s Function
PAW	Projected Augmented Wave
PBE	Perdew–Burke–Ernzerhof
PDOS	Partial Density of States
PWSCF	Plane Wave Self-Consistent Field
QE	Quantum Espresso
SCF	Self-consistent Field
SOC	Spin-Orbit Coupling
TMDC	Transition Metal di-Chalcogenide
VBM	Valence Band Maxima

CHAPTER 1

Introduction

1.1 Preface

The necessity for nanoscaled, high-performance and low-cost field effect transistors (FET) is steadily increasing. Researchers have been constantly exploring for ingenious ways and novel materials for the next generation devices to serve this ever-increasing demand [1]–[3]. According to the Moore's law, the scaling of the FET channel length, dielectric thickness results in smaller, faster transistors than the preceding generation [4]. Due to manufacturing and other performance constraints, such scaling approach has achieved saturation [5]. The scalability of the conventional form of MOSFETs presents significant challenges. Short channel field effect transistors frequently suffer from reduced electrostatic control that results in high leakage current, threshold voltage roll-off, drain induced barrier lowering and impaired drain current saturation [6]–[9]. The off-state current increases as the gate control over the short channel is decreased, increasing the switching power loss of the devices. The thermal management of the devices will be problematic due to increased switching power loss. In addition, ineffective thermal management will further deteriorate the device's performance. This has been one of the major impediments to further field effect transistor's scaling down. Many innovative ways based on Silicon technology have been developed to mitigate such effects, including the use of high-k dielectrics [10] and multi-gate transistor [11], gate all-around cylindrical transistors [12]. In addition, several novel materials [13] other than Silicon have been recommended to address the challenges mentioned above.

To continue with the Moore's law, researchers have been working on three-dimensional (3D) integration of nanoscaled memory and logic devices to enhance the performance of the devices and systems. In such platforms, atomically thin two-dimensional materials are excellent choices that can be combined with conventional Silicon devices. Since the discovery of graphene, researchers have been focusing their efforts on novel two-dimensional (2D) materials due to their remarkable properties in comparison to their bulk

counterparts [14], [15]. At the nanoscale, 2D materials can complement silicon CMOS technology by improving device mobility, on current, on/off current ratio, subthreshold swing, and contact resistance, etc. [16]. Additionally, current 3D integration of logic, memory, and optoelectronic devices into a single nanoscaled chip [17] necessitates the use of two-dimensional materials for transistor channel material, thermal insulator, light emitters, and photodetectors [18], [19]. However, group-IV elemental monolayers (graphene, silicene, germanene, and stanene) have restricted their applications in digital electronics due to their semimetallic nature [20], [21]. Other two-dimensional materials have been studied, including transition metal dichalcogenides, hexagonal boron nitrides (h-BN), and phosphorene, but they do not surpass graphene in terms of other electrical, thermal, and optical characteristics [22], [23]. Stable two-dimensional materials with graphene-like characteristics and a considerable energy bandgap are of great scientific interest [24].

Recent investigations indicate that 2D binary and ternary compounds of Group-IV elements (C, Si, Ge, and Sn) have promising mobility and energy bandgap properties [25], [26]. Additionally, the Molecular Beam Epitaxy (MBE) approach has been used to fabricate monolayers and few layers of GeSiSn, SiSn, and Ge on Si (100) substrates [27]. The characteristics of ternary hybrid monolayers of Si, Ge, and Sn atoms have not been studied yet, which may hold great promise for next-generation nanotechnology. Thus, a comprehensive investigation of the structural, electrical, optical, and electron transport properties of novel hybrid monolayers of Si, Ge, and Sn, $\text{Si}_x\text{Ge}_y\text{Sn}_{1-x-y}$, based on first-principles calculations, can be significant in giving insight into the intriguing properties of these hybrid monolayers and their potential applications.

1.2 Literature Review

After the emergence of graphene, exploring atomically thin novel and stable two-dimensional (2D) materials and investigating their properties have drawn intensive attention of the researchers since 2D materials possess fascinating electronic, optical, mechanical and thermal properties as compared to their bulk counterparts [28]–[30]. Utilizing 2D materials, it is possible to exploit the intriguing characteristics of the quantum mechanical realm such as tunable energy bandgap, very high charge carrier mobility, superconductivity, topology protected conductivity, enhanced optical conductivity in the visible region [31]–[34], and thus 2D materials offer a great promise for the future of nano-scaled technology and physical science [35], [36]. Graphene, atomically thin honeycomb structure of carbon atoms, has initiated the quest for the extraordinary properties such as relativistic-massless Dirac fermion, high charge carrier mobility, ballistic electron transport at room temperature [37], [38] which hold great promises for future nanoscaled electronics. But the application of graphene is limited due to its chemically inert character and semimetallic property [23]. Presence of energy bandgap is necessary to implement digital switching devices such as field effect transistor (FET). To open considerable energy bandgap in graphene various approaches have been taken which include patterning graphene layers into nanoribbons [39]–[42], applying external electric field [43]–[46], applying uniaxial and biaxial strain [47]–[49], functionalizing with other materials [50], [51], forming van der Waals heterostructures [52]. In general, the wider the band gap opened by external factors, the more parabolic (rather than cone shaped) the valence and conduction bands become: this reduces the curvature around the K point and increases the effective mass of the charge carriers [53], lowering the charge carrier mobility eventually. Higher charge carrier mobility holds promise for future electronic and optoelectronic devices such as ultrafast transistors [54], negative differential resistance, [55] spin filter effects, [56] large magneto-resistance response [57], [58], and photodiodes. Furthermore, 2D materials' superior thermal and optical properties might complement conventional silicon devices [59], [60].

With the emergence of graphene, researchers have explored other alternative 2D materials such as transition metal dichalcogenides (TMDCs), hexagonal boron nitrides (h-BN), phosphorene, metal carbides, nitrides etc. Researchers have recently been utilizing TMDCs

as transistor channel material, but these materials offer very low mobility [61]. Monolayer h-BN is being utilized in thermal applications [62] and phosphorene nanoribbons are reported to become unstable under external strain [63]. These monolayers cannot outperform graphene in terms of electronic, thermal, and optical properties. In recent years, graphene analogue of Si, Ge and Sn atoms also known as silicene, germanene and stanene, respectively have also attracted great interest due to their extra-ordinary characteristics [20], [21]. These stable monolayers have been experimentally realized using Molecular Beam Epitaxy (MBE) growth and mechanical exfoliation method [64]–[68]. Silicene, germanene and stanene are buckled honeycomb structures composed of Si, Ge and Sn atoms respectively due to the presence of sp^2 - sp^3 like orbital hybridization and these monolayers have very small energy bandgap in their energy band structures in the presence of spin-orbit coupling (SOC) as reported by Balendhran et al [69]. Although linear energy-momentum relation is observed near the K point of the Brillouin Zone (BZ), the energy bandgap present in silicene, germanene and stanene are not sufficient enough to overcome the semimetallic characteristics. So, exploring stable 2D materials which combine the fascinating characteristics of graphene and possess considerable energy bandgap is of great scientific quest. Researchers have applied various techniques on these novel 2D materials as on graphene such as applying uniaxial and biaxial strain, applying vertical electric field, creating multilayer nano-structures [70], [71] to combine high charge carrier mobility with significant energy bandgap. Atomically thin binary compounds of Group-IV elements (C, Si, Ge, Sn) such as monolayer SiC, SiGe, SiB, SnGe have also been studied to harness extraordinary characteristics [72]. Researchers have also studied ternary hybrid monolayers of C, Si, Ge atoms to implement a potential 2D materials that may offer high charge carrier mobility with considerable energy bandgap. These monolayers show significant energy bandgap but lack the linear-energy momentum relation [73]. 2D materials are also being utilized in highly efficient optoelectronic devices [74] to extract near unity photoluminescence quantum yield. These materials have also potential applications in designing highly efficient sensing devices. Recently, 2D MoS₂ nanopores are designed to sense DNA molecules [75], and other 2D materials are widely studied as gas sensors [76]. Electronic, optical, and charge transport characteristics of monolayer ternary compound honeycomb structures of Si, Ge, and Sn atoms have not been studied yet which may hold a great promise for the next-generation nanotechnology. Moreover, Timofeev et al have

reported the growth techniques of monolayer and few layers GeSiSn, SiSn, and Ge on Si(100) substrate using Molecular Beam Epitaxy (MBE) method [27].

Motivated by the above considerations, in this work novel hybrid monolayers have been designed and characterized that offer considerable energy bandgap with high charge carrier mobility, superior optical and electron transport properties. Three different novel hybrid monolayers consisting of Si, Ge, and Sn atoms namely $\text{Ge}_{0.25}\text{Sn}_{0.25}\text{Si}_{0.50}$, $\text{Si}_{0.25}\text{Ge}_{0.25}\text{Sn}_{0.50}$ and, $\text{Sn}_{0.25}\text{Si}_{0.25}\text{Ge}_{0.50}$ were modelled based on Density Functional Theory (DFT). These novel hybrid monolayers are mechanically and dynamically stable which are testified by calculating the elastic constants, phonon dispersion characteristics and cohesive energy. The structural properties, e.g. lattice constant, buckling height and bond length are investigated in detail. These proposed novel hybrid monolayers of Si, Ge and Sn possess significant energy bandgap at the K point of the BZ as well as linear energy-momentum relation which ensures very high charge carrier mobility. The energy band structure with and without considering the spin-orbit coupling (SOC), atom projected density of states, differential charge density have been calculated. In order to investigate the charge conductivity of these hybrid monolayers, effective mass and acoustic phonon limited mobility of the charge carriers have been computed. To understand the interaction of these proposed hybrid monolayers with electromagnetic wave i.e. light, the optical properties, such as dielectric function, electron loss function, absorption coefficient, refractive index, reflectivity, and optical conductivity as a function of frequency for parallelly and perpendicularly polarized incident light have been calculated. This study presents detail insight of the optical properties of these hybrid monolayers. Then hydrogen passivated relaxed armchair nanoribbons were designed utilizing the proposed hybrid monolayers and their electron transport characteristics e.g. transmission function, I-V characteristics were calculated using Non-Equilibrium Green's Function (NEGF) formalism within DFT. The calculated electron transport characteristics further ensure the semiconducting characteristics of the hybrid monolayers. The significant changes in electron transport characteristics due to adsorption of NH_3 molecules and the presence of point defects in these proposed hybrid monolayers have also been studied which confirms the sensing application of these hybrid armchair nanoribbons.

1.3 Thesis Objectives

The primary objective of this thesis is to model the geometrically optimized structure of three different novel hybrid monolayers comprising of Si, Ge, and Sn atoms with varying proportions namely $\text{Ge}_{0.25}\text{Sn}_{0.25}\text{Si}_{0.50}$, $\text{Si}_{0.25}\text{Ge}_{0.25}\text{Sn}_{0.50}$, and $\text{Sn}_{0.25}\text{Si}_{0.25}\text{Ge}_{0.50}$ using first principle calculations within the framework of density functional theory (DFT). The modelled atomically thin structures will be geometrically relaxed with optimum energy and atomic force thresholds and the structural properties, e.g. lattice constant, buckling height, and bond length of respective monolayers will be determined with accuracy. The mechanical and dynamic stability of the modeled hybrid monolayers will be examined by studying their in-plane elastic constants, phonon dispersion characteristics and cohesive energy. The positive value of in-plane elastic constants, absence of imaginary frequency in the phonon dispersion curves and the negative cohesive energy will be the indicators of mechanical and dynamic stability of the structures. Then the electronic properties of the novel hybrid monolayers will be computed in detail, e.g., electronic band structure considering spin-orbit coupling, atom projected density of states, differential charge density, effective mass, and acoustic phonon limited mobility of the charge carriers. The computed parameters will be compared and validated by the reported parameters of the neighboring monolayers. To gain insights on the interaction of these novel hybrid monolayers with electromagnetic wave, i.e. light optical properties will be calculated as a function of frequency for parallelly and perpendicularly polarized incident light. Optical properties such as, dielectric function, electron energy loss function, absorption coefficient, refractive index, reflectivity, and optical conductivity will be calculated for the hybrid monolayers of Si, Ge, and Sn. Then charge transport characteristics of these novel hybrid monolayers will be studied. In order to do these three novel hybrid monolayers will be patterned into nanoribbons to build transport devices, voltage will be applied across the transport devices and output current is measured. Electron transport properties of the novel hybrid monolayers, e.g., current-voltage characteristics, transmission function will be calculated for pristine nanoribbons and also in the presence of NH_3 molecules and point defects. Such studies may open the prospects sensing applications of these novel hybrid monolayers of Si, Ge, and Sn.

1.4 Thesis Outline

The layout of the thesis is as follows. The theory and the details of density functional theory for the characterization of electronic, optical, charge transport properties of novel hybrid monolayers of Si, Ge, and Sn are discussed in Chapter 2. A brief discussion of the properties and the theory to obtain them with DFT are also given in this chapter. Chapter 3 deals with the atomic structures of novel hybrid monolayers of Si, Ge, and Sn along with the computational details and methodologies for obtaining the results. Chapter 4 contains the detailed results of the electronic, optical, and charge transport properties of novel hybrid monolayers of Si, Ge, and Sn. Finally, the conclusions are drawn in Chapter 5 with a brief discussion on the future scope for work in this direction.

CHAPTER 2

Theoretical Foundation

The density functional theory (DFT) is addressed in this chapter, which is essential for the characterization of structural, electrical, optical, and electron transport characteristics.

Following that, descriptions of various characteristics and ways for getting them using DFT are briefly presented.

2.1 Density Functional Theory

In solid-state and condensed matter physics, the density functional theory (DFT) has been one of the most successful and promising ways to examine electronic, thermal, spintronic, and optical structure computations. This theory determines the features of a many-electron system that is spatially dependent on the three-dimensional electron density functional. The phrase "density functional theory" was coined as a result. Apart from providing a distinct and rigorous technique to handling interacting issues and parametrizing empirical facts, it has been a thorough alternative to the Schrodinger equation for many particle systems. This approach is widely used to accurately determine the ground-state electrical structure of many-body systems, such as atoms, molecules, and condensed phases.

2.1.1 Schrödinger Equation for Many-Body systems

All the necessary information about a system can be harnessed from the quantum mechanical wave-function of that system. As a result, the most important objective in solid-state physics, and material sciences is to solve the time-independent, non-relativistic Schrödinger equation. The time independent form of Schrödinger equation is as follows,

$$\hat{H}\Psi(\mathbf{r}, \mathbf{R}) = E\Psi(\mathbf{r}, \mathbf{R}) \quad (2.1)$$

Also, the time dependent form of Schrödinger equation is as follows,

$$\hat{H}\Psi(\mathbf{r}, \mathbf{R}) = -i\hbar \frac{\delta}{\delta t} \Psi(\mathbf{r}, \mathbf{R}) \quad (2.2)$$

Here \hat{H} is the Hamiltonian for a system consisting of N nuclei and n electrons which is given by:

$$\hat{H} = T_e + T_N + V(\mathbf{r}, \mathbf{R}) \quad (2.3)$$

Here,

T_e = Kinetic energy of the interacting electrons with mass m

T_N = Kinetic energy of nucleus with mass M

$V(\mathbf{r}, \mathbf{R})$ = Total potential energy

\mathbf{r} = Position vector of electrons

\mathbf{R} = Position vector of nuclei

Again,

$$T_N = - \sum_{\mu} \frac{\hbar^2}{2M_{\mu}} \nabla_{\mathbf{R}\mu}^2 \quad (2.4)$$

$$T_e = - \sum_i \frac{\hbar^2}{2m} \nabla_{\mathbf{r}_i}^2 \quad (2.5)$$

$$V(\mathbf{r}, \mathbf{R}) = - \sum_{i,\mu} \frac{Z_{\mu} e^2}{|\mathbf{r}_i - \mathbf{R}_{\mu}|} + \frac{1}{2} \sum_{i \neq j} \frac{e^2}{|\mathbf{r}_i - \mathbf{r}_j|} + \frac{1}{2} \sum_{\mu \neq \nu} \frac{Z_{\mu} Z_{\nu} e^2}{|\mathbf{R}_{\mu} - \mathbf{R}_{\nu}|} \quad (2.6)$$

where,

\hbar = Reduced Planck's constant

Z = Atomic number of the nucleus

Here, i and j represent the n electrons in the system, whereas μ and ν run over the N nuclei. The three variables in $V(\mathbf{r}, \mathbf{R})$ stand for the attractive electrostatic interaction between

nuclei and electrons, as well as repulsive potential owing to electron-electron and nucleus-nucleus interactions.

The precise solution of the Schrödinger equation may be determined in order to get the wave-function and allowable energy levels of a basic 2D square potential or even a hydrogen atom. This is owing to the fact that the complexity of certain problems, such as the number of electrons, is not very great. Due to the tremendous complexity, it is hard to obtain a precise solution to the Schrödinger equation for a many-body system. As a result, some estimates are required to solve the problem.

2.1.2 Born-Oppenheimer Approximation

In quantum chemistry simulations of molecular wave-functions, the Born–Oppenheimer (BO) approximation has been widely employed to minimize computing difficulties without sacrificing accuracy. Because the nucleus has a far bigger mass than the electron, the wave functions of the nucleus and electrons are considered to be independent. The nucleus is believed to be a point charge that does not move. Because the Coulombic forces on electrons and nuclei are approximately comparable in magnitude, the resulting change in their momenta is likewise expected to be similar. This assumption permits the wave-function of a molecule to be split down into its electronic and nuclear (vibrational, rotational) components in mathematical terms.

$$\Psi_{total} = \Psi_{electronic} \times \Psi_{nuclear} \quad (2.7)$$

This approach greatly simplifies the computation of the energy and wave-function of an average-size molecule. A water molecule, for example, has three nuclei and ten electrons. For this situation, the time-independent Schrödinger equation becomes a partial differential eigenvalue equation with 39 variables — the spatial coordinates of the electrons and nuclei.

The electronic Schrödinger equation is solved first using the BO approximation, resulting in the wave-function $\Psi_{electronic}$, which is purely dependent on electrons. $\Psi_{electronic}$ relies on 30 electronic coordinates for water. Interactions between electrons and nuclei are still

existent. The Coulomb potential of the nuclei, which is clamped at particular points in space, is nonetheless felt by the electrons. The *Clamped Nuclei Approximation* is the name given to the first phase of the BO approximation. The electronic Schrödinger equation is therefore reduced to

$$\left(-\frac{\hbar}{2m} \sum_i \nabla_{r_i}^2 + V(\mathbf{r}, \mathbf{R}) \right) \Psi_{\mathbf{R}}(\mathbf{r}) = E(\mathbf{R}) \Psi_{\mathbf{R}}(\mathbf{r}) \quad (2.8)$$

For a given \mathbf{R} and once obtained, potential energy surface $E(\mathbf{R})$ determines the nuclear motion.

The obtained function from the previous stage is used as a potential of the Schrödinger equation in the following portion of the computation. This time, the equation just comprises the nuclei, such as a 9-variable equation for water. With the aid of this approximation, similar techniques may solve a differential equation of enormous complexity for a huge system. This approximation makes obtaining the answer considerably easier, which leads to the molecule's energy and wave-function.

2.1.3 Hohenberg-Kohn Theory

The charge density of the ground state, $n(\mathbf{r})$, is at the core of density functional theory. It is defined as follows for N electrons:

$$n(\mathbf{r}) = N \int |\Psi(\mathbf{r}, \mathbf{r}_2, \dots, \mathbf{r}_N)|^2 d\mathbf{r}_2 \dots d\mathbf{r}_N \quad (2.9)$$

The Eigen function of Hamiltonian H is $\Psi(r_1, r_2, \dots, r_N)$. The spatial coordinates for n are reduced to merely three variables when state charge density is used $n(\mathbf{r})$. The Eigen function is indicated by Ψ_0 for the ground state of Hamiltonian H , and its corresponding electron density is $n_0(\mathbf{r})$ is defined by Eq (2.9). Eq. (2.3) should be solved self consistently for $n(\mathbf{r})$ instead of $\psi(\mathbf{r})$.

The Hohenberg-Kohn theorems [77] can be applied to any system consisting of electrons moving under the influence of an external potential $V(\mathbf{r}, \mathbf{R})$. It states that:

Theorem I: The external potential $V(\mathbf{r}, \mathbf{R})$, and hence the total energy, is a unique functional of the electron density $n(\mathbf{r})$.

Theorem II: The ground state energy can be obtained variationally; the density that minimizes the total energy is the exact ground state density.

In a summary, there is a single potential $V(\mathbf{r}, \mathbf{R})$ with the charge density $n(\mathbf{r})$ as the ground state. The Hohenberg-Kohn theorems offer a method for determining our desired $n(\mathbf{r})$. The following are the ramifications of these theorems:

- The electronic part of the energy can be written as a functional of $n(\mathbf{r})$:

$$E[n(\mathbf{r})] = F[n(\mathbf{r})] + \int n(\mathbf{r})V(\mathbf{r})d\mathbf{r} \quad (2.10)$$

Where, $F[n(\mathbf{r})]$ is a universal functional of the density, $V(\mathbf{r})$ is the external (nuclear) potential acting on each electron:

$$V(\mathbf{r}) = - \sum_{\mu} \frac{Z_{\mu}e^2}{|\mathbf{r} - \mathbf{R}_{\mu}|} \quad (2.11)$$

- $E[n(\mathbf{r})]$ is minimized by the ground-state charge density $n(\mathbf{r})$.

2.1.4 Kohn-Sham Equations

Kohn-Sham equations [78] are obtained from the Hohenberg-Kohn theorems. The Kohn-Sham density functional theory is based on these equations. For both a many electron interacting system and a non-interacting system, they are derived by inducing similar ground state electron density and assuming the same external potential. Following these theorems and the 'one electron theory,' the orbitals ψ_i for a non-interacting set of electrons with the charge density:

$$n(\mathbf{r}) = \sum_i |\psi_i|^2 \quad (2.12)$$

where, $\langle \psi_i | \psi_j \rangle = \delta_{ij}$. $n(\mathbf{r})$ is identical to the actual system's.

The energy functional can be written as:

$$E = T_s[n(\mathbf{r})] + E_H[n(\mathbf{r})] + E_{xc}[n(\mathbf{r})] + \int n(\mathbf{r})V(\mathbf{r})d\mathbf{r} \quad (2.13)$$

Here $T_s[n(\mathbf{r})]$ is the kinetic energy of the non-interacting electron,

$$T_s[n(\mathbf{r})] = -\frac{\hbar^2}{2m} \sum_i \int \psi_i^*(\mathbf{r}) \nabla^2 \psi_i(\mathbf{r}) d\mathbf{r} \quad (2.14)$$

$E_H[n(\mathbf{r})]$ is the Hartree energy, due to electrostatic interactions,

$$E_H[n(\mathbf{r})] = \frac{e^2}{2} \int \left(\frac{n(\mathbf{r})n(\mathbf{r}')}{|\mathbf{r} - \mathbf{r}'|} \right) d\mathbf{r}d\mathbf{r}' \quad (2.15)$$

Exchange-correlation is denoted by $E_{xc}[n(\mathbf{r})]$. It contains all of the quantum mechanics-related energy concepts that are yet unknown. The Kohn-Sham (KS) equations are obtained by minimizing the energy with respect to ψ_i

$$\left(-\frac{\hbar^2}{2m} \nabla^2 + V(\mathbf{r}) + V_H(\mathbf{r}) + V_{xc}(\mathbf{r}) \right) \psi_i = \epsilon_i \psi_i(\mathbf{r}) \quad (2.16)$$

The Hartree and exchange-correlation potentials are given by,

$$V_H(\mathbf{r}) = \frac{\delta E_H[n(\mathbf{r})]}{\delta n(\mathbf{r})} = e^2 \int \frac{n(\mathbf{r}')}{|\mathbf{r} - \mathbf{r}'|} d\mathbf{r}' \quad (2.17)$$

$$V_{xc}(\mathbf{r}) = \frac{\delta E_{xc}[n(\mathbf{r})]}{\delta n(\mathbf{r})} \quad (2.18)$$

These potentials are strongly intertwined to ψ_i via the charge density. The energy may be represented in a different way using Kohn-Sham (KS) eigenvalues.

$$E = \sum_i E_i - E_H[n(\mathbf{r})] - \int n(\mathbf{r})V_{xc}(\mathbf{r})d\mathbf{r} + E_{xc}[n(\mathbf{r})] \quad (2.19)$$

With the information of $E_{xc}[n(\mathbf{r})]$ and $V_{xc}[n(\mathbf{r})]$, the solution to the Kohn-Sham equation may be obtained.

2.1.5 Exchange-Correlational Functionals

In Kohn-Sham DFT, the exchange correlation functional is essentially an aggregation of all the electronic energy contributions that cannot be represented correctly as a function of the electronic density. Except for the free electron gas, the exact functionals for exchange and correlation are unknown. These might include non-interacting kinetic and potential energy, self-interaction of a single electronic density with itself, anti-symmetry of a fermionic wavefunction, and so on. However, employing approximations to calculate some physical variables yields results that closely resemble genuine data. The uniform-electron-gas is used to simulate Exchange-Correlation functionals. For a wide variety of densities, Monte-Carlo algorithms offer correlation energy (and potential). A density functional was created by parameterizing this correlation energy. Local Density Approximation (LDA), Generalized Gradient Approximation (GGA), meta-GGA, van der Waals functionals, and others are examples of functionals. The choice of functionals has a big impact on the calculation's correctness. LDA [79] and GGA [80], [81] are the most extensively utilized approximations in solid-state computations. Special functionals are employed for specialized goals, such as structural optimization in layered systems with the vdW-DF functional [82].

2.1.5.1 Local Density Approximation

All approximate exchange correlation functionals are based on the local density approximation (LDA). The value of the electronic density in each place in space determines

the exchange-correlation energy functional. LDA is based on the concept of a uniform electron gas. This is a system in which electrons travel against a positive background charge distribution, resulting in a neutral ensemble. LDA is mostly governed by the assumption of substituting the energy functional with a function of the local density $n(\mathbf{r})$. The exchange-correlation energy and potential are given by the following equations using this approximation:

$$E_{xc} = \int n(\mathbf{r})\epsilon_{xc}(n(\mathbf{r}))d\mathbf{r} \quad (2.20)$$

$$V_{xc}(\mathbf{r}) = \epsilon_{xc}(n(\mathbf{r})) + n(\mathbf{r}) \left. \frac{d\epsilon_{xc}(n)}{dn} \right|_{n=n(\mathbf{r})} \quad (2.21)$$

where, $\epsilon_{xc}(n)$ is the exchange-correlation energy per particle of a uniform electron gas density of n .

The quantity $\epsilon_{xc}(n)$ can be further subdivided into contributions to exchange and correlation as follows,

$$\epsilon_{xc}(n) = \epsilon_c(n) + \epsilon_x(n) \quad (2.22)$$

The exchange portion, $\epsilon_x(n)$, which reflects an electron's exchange energy in a homogeneous electron gas of a certain density. Bloch and Dirac [83] were the first to derive it. It can be calculated using the following formula:

$$\epsilon_x(n) = -\frac{3}{4} \left(\frac{3}{\pi} \right)^{\frac{1}{3}} n(\mathbf{r}) \quad (2.23)$$

For the correlation portion, $\epsilon_c(n)$, there is no such explicit formulation. To get the right values for this portion, quantum Monte Carlo computations were used [84]. Then, to get a closed expression, interpolation is performed [85].

2.1.5.2 Generalized Gradient Approximation

LDA is unable to detect rapid changes in charge density and produces inaccurate conclusions. Apart from utilizing the knowledge about the density $n(\mathbf{r})$ at a given site, the first logical step to avoid such scenarios is to utilize the gradient of the charge density, $|\nabla n(\mathbf{r})|$, to account for the non-homogeneity of the actual electron density. As a result, we write the exchange-correlation energy in the generalized gradient approximation form (GGA) as follows,

$$E_{xc} = \int n(\mathbf{r})\epsilon_{GGA}(n(\mathbf{r}), |\nabla n(\mathbf{r})|)d\mathbf{r} \quad (2.24)$$

For molecular structures and ground-state energies, GGA produces excellent results. It outperforms other proven correlated wavefunction algorithms [86] and is a significant improvement over LDA. Unlike LDA, which has just one form, multiple parameterizations of the GGA may be derived using a variety of approaches, such as first principles, semi-empirical form utilizing experimental data, and so on. The increased computational difficulties come at the cost of increased accuracy in outcomes.

2.1.5.3 Other Functionals

By combining a component of the actual exchange energy computed from Hartree–Fock theory with the remainder of the exchange–correlation energy from other sources, difficulties in describing the exchange part of the energy can be alleviated (ab-initio or empirical). Hybrid functionals are those that are obtained from a mix of sources. HSE, B3LYP, PBE0, and another hybrid functionals are extensively employed [87]-[89]. Despite the fact that they produce more accurate results than LDA or GGA, their computational complexity is quite high. Non-local correlation is estimated together with a mixture of LDA and GGA in the van der Waals functional, making it a good choice for layered materials to confront their inter-layer interactions.

2.1.6 Plane-wave Basis Sets

We can identify the quantum $\psi_i(\mathbf{r})$ as $\psi_{nk}(\mathbf{r})$ by applying boundary conditions to the Kohn-Sham equations, where n is the band index and k is the crystal momentum. The equations become,

$$\left(-\frac{\hbar^2}{2m} \nabla^2 + V(\mathbf{r}) + V_H(\mathbf{r}) + V_{xc}(\mathbf{r}) \right) \psi_{nk} = \epsilon_{nk} \psi_{nk}(\mathbf{r}) \quad (2.25)$$

$$V_{KS} = V(\mathbf{r}) + e^2 \int \frac{n(\mathbf{r}')}{|\mathbf{r} - \mathbf{r}'|} d\mathbf{r}' + V_{xc}(\mathbf{r}) \quad (2.26)$$

$$n(\mathbf{r}) = \sum_{nk} |\psi_{nk}|^2 \quad (2.27)$$

How to solve these coupled equations efficiently from this explicit Hamiltonian is a real challenge. In order to solve the Kohn-Sham equations numerically, an appropriate basis for expanding the wave functions ψ_{nk} is required. The simulation time will be limited due to the truncation of the basis. Plane waves are the most appropriate basis option for two reasons: the Bloch states ψ_{nk} contain a periodic portion and may be enlarged in Fourier series.

$$\psi_{nk}(\mathbf{r}) = e^{ik \cdot \mathbf{r}} u_{nk}(\mathbf{r}) = e^{ik \cdot \mathbf{r}} \sum_{\mathbf{G}} C_{nk} \left(\frac{e^{i\mathbf{G} \cdot \mathbf{r}}}{\sqrt{\Omega}} \right) \quad (2.28)$$

where $\Omega = \text{Volume of the unit cell}$.

Inserting $\psi_{nk}(\mathbf{r})$ into the Kohn-Sham equations we find that $C_{nk}(\mathbf{G})$ satisfy,

$$\frac{|\mathbf{K} + \mathbf{G}|^2}{2} C_{nk}(\mathbf{G}) + \sum_{\mathbf{G}'} \tilde{V}_{KS}(\mathbf{G} - \mathbf{G}') C_{nk}(\mathbf{G}') = \epsilon_{nk} C_{nk}(\mathbf{G}) \quad (2.29)$$

Where \tilde{V}_{KS} is the Fourier transform of V_{KS} . To get a finite number of $\{\mathbf{G}\}$ basis, a cut off E_{cut} is obtained,

$$\frac{|\mathbf{K} + \mathbf{G}|^2}{2} \leq E_{cut} \quad (2.30)$$

In theory, it appears that raising E_{cut} can attain any level of precision. However, because the core electrons in molecules are strongly bonded to the nuclei, this strategy does not function in actuality. Furthermore, at the core area, their wave functions vary fast and quickly degrade. With multiple plane waves, expansion is required to adequately characterize the wave functions. Those core electrons, on the other hand, are so securely bonded to the nuclei that their contribution to solid or molecular bonding is negligible. As a result, solely using the plane wave basis will result in massive calculations to describe electrons that only play a small part in determining the desired attributes.

2.1.7 Projected Augmented Wave Basis and Pseudo-Potentials

The materials' bonding characteristics are mostly determined by valence electrons rather than core electrons. The *Frozen Core Approximation* is used to acknowledge this reality. This approximation treats the core electrons as stationary. As a result, they are not included in the calculation. Numerical computations utilizing valence electron wave functions, on the other hand, are enormous. Excess plane wave basis is required to explain the fast oscillation of wave functions in the core area caused by valence electrons.

The PAW (Projected Augmented Wave) technique is used to solve this problem. The valence wavefunctions are then substituted within the core region with smoother node-less pseudo-wavefunctions that are equal to the original wavefunctions outside the core region. The transformation of these quickly oscillating wave-functions into smooth wave-functions is more computationally efficient and allows all-electron characteristics to be calculated. The pseudo-potentials [90] are a formalization of this concept. The pseudo-wavefunctions must be equal to the all-electron wavefunctions outside the core in order for a pseudopotential calculation to generate the same energy differences as an all-electron calculation. This is referred to as 'norm-conservation' [91].

The linear transformation T in the PAW approach converts the fictional pseudo wave-function $\tilde{\psi}$ to the all-electron wave-function ψ as follows,

$$|\psi\rangle = T|\tilde{\psi}\rangle \quad (2.31)$$

In order to have ψ and $\tilde{\psi}$ differ only in the regions near the ion cores, T becomes

$$T = 1 + \sum_R \hat{T}_R \quad (2.32)$$

Only inside some spherical augmentation area Ω_R surrounding atom at R is \hat{T}_R non-zero. Expanding the pseudo wave-function into pseudo partial waves around each atom is beneficial.

$$|\tilde{\psi}\rangle = \sum_i |\tilde{\phi}_i\rangle c_i, \quad \text{within } \Omega_R \quad (2.33)$$

Because T is a linear operator, the coefficients c_i may be expressed as an inner product with a set of projector functions, $|p_i\rangle$.

$$c_i = \langle p_i | \tilde{\psi} \rangle \quad (2.34)$$

where $\langle p_i | \tilde{\phi}_j \rangle = \delta_{ij}$.

The solutions to the Kohn-Sham Schrödinger equation for an isolated atom are commonly considered to be all electron partial waves $|\phi_i\rangle = T|\tilde{\phi}_i\rangle$. As a result, three quantities define the transformation T :

- a) Set of all-electron partial waves $|\phi_i\rangle$
- b) Set of pseudo partial waves $|\tilde{\phi}_i\rangle$
- c) Set of projector functions $|p_i\rangle$

and we can explicitly write it down as

$$T = 1 + \sum_i (|\phi_i\rangle - |\tilde{\phi}_i\rangle) \langle p_i | \quad (2.35)$$

Numerous investigations have shown that using the PAW approach with pseudo-potential in realistic simulations saves computing costs greatly when chemical bonding is well described.

2.1.8 Ultrasoft Pseudo-Potentials

Ultrasoft pseudopotentials (USP) were developed to allow computations to be done with the lowest possible cutoff energy for the plane-wave basis set. A novel approach has been devised since it is well known that optimizing the convergence of norm-conserving pseudopotentials has inherent restrictions. In most cases, a high cutoff energy for the plane-wave basis set is only required when there are densely linked orbitals that have a considerable proportion of their weight inside the atom's core area, according to the theory behind USP. In these circumstances, breaking the norm-conservation criterion by removing the charge associated with these orbitals from the core region is the only way to decrease the basis set. The pseudo wavefunctions within the core are thus allowed to be as soft as possible, resulting in a considerable reduction in the cutoff energy.

This is achieved by proposing an extended orthonormality requirement. The square moduli of the wavefunctions enhance the electron density in the core regions in order to restore the whole electronic charge. As a result, the electron density may be divided into two parts: a soft component that spans the unit cell and a hard part focused in the core.

2.1.9 Electronic Minimization

Ground state can be achieved in one of two ways.

- Direct Minimization
- Self-consistent Cycle

Between these two, the self-consistent cycle is the most frequently employed strategy. It starts with a trial density, then builds and solves the matching Kohn-Sham Hamiltonian to get a collection of orbitals. These orbitals define a new density, which in turn defines a new Hamiltonian, bringing the system back to self-consistency. The cycle finishes and the final

result is attained if the difference between the old and new density for a term (e.g. energy or force) falls below a specific threshold. To obtain the self-consistent charge density (or potential), the following procedures are carried out in a self-consistent manner:

- Initialize with a trial charge density
- Calculate the potential from the charge density
- Solve (diagonalize) the Kohn-Sham equations at fixed potential
- Calculate the charge density from Kohn-Sham orbitals
- Compare the results and either continue or stop the loop based on the tolerance

2.1.10 Variable Cell Structural Optimization

The goal of geometry optimization is to create the optimized (lowest energy) structure of atomic systems from any initial condition. The use of the Born-Oppenheimer approximation to geometry optimization often results in a series of single point energy calculations. For the basic beginning geometry, a single point energy calculation is conducted. By minimizing the function $E(R_1, R_2, \dots, R_N)$, the global ground state may be determined. For a system of N atoms, this function is based on the $3N$ atomic coordinates. The Hellmann-Feynman theorem [92] may be used to compute the forces on the nuclei from the wavefunction. In general, equilibrium is obtained in a crystal when all forces on atoms in the unit cell are zero, as well as all stresses.

The derivatives of the total energy with respect to the atomic coordinates are the forces on atoms. Forces are just the anticipated value of the derivative of the external potential, according to the Hellmann-Feynman theorem.

$$F_\mu = -\frac{\delta E}{\delta R_\mu} = -\sum_i f_i \left\langle \psi_i \left| \frac{\delta V}{\delta R_\mu} \right| \psi_i \right\rangle \quad (2.36)$$

The stress σ is the derivative of the energy w.r.t the strain ϵ ,

$$\sigma = -\frac{1}{\Omega} \left(\frac{\delta E}{\delta \epsilon} \right) \quad (2.37)$$

2.1.11 Brillouin Zone sampling

In the reciprocal lattice, a Brillouin zone is defined as a Wigner-Seitz primitive cell. The first Brillouin zone is the smallest volume totally encompassed by planes traced from the origin that are perpendicular bisectors of reciprocal lattice vectors. It comprises all points in the reciprocal lattice that are closest to the contained reciprocal lattice point. Planes that are perpendicular to the reciprocal lattice vectors define the limits of the first BZ. Bloch's theorem states that the electrons in the unit cell can only be considered at an unlimited number of k-points within the first Brillouin zone. It is also feasible to employ a finite number of k-points if they are chosen to sample the reciprocal space suitably. As a result, an integrated function $f(\mathbf{r})$ over the Brillouin zone may be written as:

$$f(\mathbf{r}) = \frac{\Omega}{(2\pi)^3} \int F(\mathbf{k}) d\mathbf{k} = \sum_j \omega_j(k_j) \quad (2.38)$$

where $F(\mathbf{k})$ is the Fourier transform of $f(\mathbf{r})$, Ω is the cell volume and ω_j are weighting factors. The set of "special" k-points chosen to appropriately sample the Brillouin zone.

2.1.12 Deformation Potential Theory

Bardeen and Shockley [93] originally developed the deformation potential theory. Herring and Vogt [94] generalized this theory. Bir and Pikus [95] studied various semiconductors via group theory and showed how to calculate strain effects on the band structure with deformation potentials. The deformation potential theory introduces an additional Hamiltonian $H(\varepsilon)$, that is attributed to strain and its effects on the band structure. This Hamiltonian is based on first order perturbation theory and its matrix elements are defined by

$$\{H(\varepsilon)\} = \sum_{\alpha,\beta=1}^3 D_{ij}^{\alpha,\beta} \varepsilon_{\alpha,\beta} \quad (2.39)$$

$D_{ij}^{\alpha,\beta}$ denotes the deformation potential operator which transforms under symmetry operations as second rank tensor and $\varepsilon_{\alpha,\beta}$ describes the (α,β) strain tensor component. The subscripts (i,j) in $D_{ij}^{\alpha,\beta}$ denote the matrix element of the operator. Due to the symmetry of

the strain tensor with respect to α and β , also the deformation potential operator has to obey this symmetry $D_{ij}^{\alpha,\beta} = D_{ij}^{\beta,\alpha}$ and thus limits the number of independent deformation potential operators to six.

In the case of cubic semiconductors, the edges of the conduction band and the valence band are located on symmetry lines. These symmetries are reproduced in the energy band structure and in the basis states. Furthermore, the symmetry of the basis states allows to describe the deformation potential operator of a particular band via two or three deformation potential constants [94]. Theoretically the deformation potential constants can be calculated via the empirical pseudo potential method or by ab initio methods. Theoretical predictions and measurements match quite well, deformation potentials can be used to measure mobility of the charge carriers [96].

2.1.13 Non-Equilibrium Green's Function

The NEGF formalism provides a generalized microscopic theory for quantum transport. It addresses the problem of dissipative transport and describes open systems fully quantum mechanically. The theory behind it is deeply rooted in the many-body theory [97]. The information of the many-particle system is put into self-energies, which are part of the equations of motion for the Green's functions. The Green's functions can be calculated from perturbation theory and describe the correlation between two operators at times t and t' . A detailed description and justification of the Green's functions and self-energies can be found for instance in the work of Datta [98].

The Hamiltonian of an open system coupled to a reservoir can be written as [99]

$$\hat{H} = \begin{pmatrix} \hat{H}_D & \sigma \\ \sigma^\dagger & \hat{H}_R \end{pmatrix} \quad (2.39)$$

Where \hat{H}_D and \hat{H}_R denote the Hamilton operators of the device and reservoir, respectively, and σ is the coupling matrix. The corresponding Schrödinger equation of the channel-reservoir system can be expressed as [100]

$$E \begin{pmatrix} \psi_D \\ \psi_R \end{pmatrix} = \begin{pmatrix} \hat{H}_D & \sigma \\ \sigma^\dagger & \hat{H}_R \end{pmatrix} \begin{pmatrix} \psi_D \\ \psi_R \end{pmatrix} \quad (2.40)$$

ψ_D and ψ_R denote the wave functions of the channel and the reservoir. The steady state equation for the Green's function is defined as

$$(1E - \hat{H})G = 1 \quad (2.41)$$

Thus, the corresponding Green's function to the device-reservoir system can be written as

$$\begin{pmatrix} G & G_{DR} \\ G_{RD} & G_R \end{pmatrix} = \begin{pmatrix} 1E - \hat{H}_D & -\sigma \\ -\sigma^\dagger & 1E - \hat{H}_R \end{pmatrix}^{-1} \quad (2.42)$$

The coupling between the device and the reservoir is described by G_{DR} and G_{RD} . The retarded Green's function G reads

$$G = \left(1E - \hat{H}_D - \sum (E) \right)^{-1} \quad (2.43)$$

and includes the self-energy which describes the interaction between the device and the reservoir [101]. The inclusion of the self-energy reduces the Green's function of the reservoir to the dimension of the Hamiltonian of the device. The self-energy is determined iteratively and satisfies

$$\Sigma = \sigma G \sigma^\dagger \quad (2.44)$$

The matrix form of the density of states is the spectral function A_s which is given by

$$A_s(E) = i(G(E) - G^\dagger(E)) \quad (2.45)$$

The electron density is provided by the density matrix

$$n = \int_0^\infty (f_E(E - E_F) A(E) dE) \quad (2.46)$$

where f_E is the Fermi-Dirac distribution function and E_F denotes the Fermi energy.

2.2 Electronic and Optical Properties

2.2.1 Electronic Band Structure

One of the most central tenets in solid state physics is electronic band structure. The band structure of a solid explains the energy bands that an electron within the solid may have (allowed bands) and the energy gaps (forbidden bands or bandgap) that it may not have (forbidden bands or bandgap). It is typically the plot of energy in the first Brillouin zone for a crystalline structure with regard to specified wavevectors (moments). The band structure may be used to explain many electrical, optical, and even magnetic characteristics of crystals. It also offers information about a material's condition. The material is insulating (or semiconducting) if the Fermi energy is positioned in a band gap, but it is metallic otherwise. It also creates the bandgap and determines whether the substance is direct or indirect. It also lays the path for determining a material's effective mass. A key step in characterizing a material's characteristics is to compute its band structure. In recent years, DFT has been widely employed to calculate a material's energy band structure. For both valence and conduction bands, electronic eigenvalues along high symmetry directions in the Brillouin Zone (BZ) are estimated non-self-consistently utilizing electronic charge densities and potentials generated during the DFT simulation. Despite the fact that DFT underestimates the bandgap's magnitude, the band shape and its derivatives match well with experimental data. At the price of high computational complexity, time dependent DFT or hybrid functionals offer superior results for bandgap.

2.2.2 Density of States and Atom Projected Density of States

The number of states per interval of energy at each energy level accessible to be occupied is described by the density of states (DOS) of a system. A density distribution is used to express it quantitatively. It's usually a weighted average of the system's many states in the space and time domains. DOS is a critical indication of a material's electrical characteristics, or conduction. It has a direct relationship with the dispersion relations of a system's attributes. At a given energy level, a high DOS indicates that numerous states are accessible for occupancy. At that energy level, a DOS of zero indicates that no states may

be inhabited. At the bandgap of a material, DOS is zero, while at the bands, it has a finite value. The entire electronic density of states (DOS) is split into the projected density of states associated with each individual molecular orbital in atom projected density of states (PDOS). The bonding process among the components of a system is depicted clearly in PDOS. Electronic eigenvalues, calculated non-self-consistently for both valence and conduction bands using electronic charge densities and potentials created during the simulation, are used to determine the DOS and PDOS of a system in DFT.

2.2.3 Charge Density

The charge distribution throughout the volume of a particle, such as a molecule, atom, or ion, is referred to as charge density. Charge density ρ is linked to wave function Ψ in quantum physics by the equation,

$$\rho(\mathbf{r}) = q|\Psi(\mathbf{r})|^2 \quad (2.47)$$

where q is the charge of the particle and $|\Psi(\mathbf{r})|^2 = \Psi^*(\mathbf{r})\Psi(\mathbf{r})$ is the probability density function i.e. probability per unit volume of a particle located at r .

When the wave-function is normalized the average charge in the region $\mathbf{r} \in R$ is,

$$Q = \int_R q|\Psi(\mathbf{r})|^2 d\mathbf{r}^3 \quad (2.48)$$

Where, $d\mathbf{r}^3$ is the 3D position space integration measure. Charge density in a grid point may be easily determined using these formulae.

2.2.4 Spin-Orbit Coupling (SOC)

Spin-Orbit coupling is an interaction of particles that depends on the values and mutual orientations of the particles' orbital and spin angular momenta and that leads to the fine-structure splitting of the system's energy levels. Spin-orbit coupling is a relativistic effect. A simple physical interpretation of spin-orbit coupling can be obtained by considering, for example, the motion of an electron in a hydrogen atom where the electron is viewed as moving around the nucleus along some "orbit." The electron has an intrinsic angular momentum, or spin, which is responsible for the existence of the electron's spin magnetic

moment. The electric charge of the nucleus generates a Coulomb electric field that should affect the spin magnetic moment of the electron moving along its orbit. This situation can be easily understood if we imagine the frame of reference where the electron is at rest—that is, the frame of reference moves with the electron. For this stationary electron, the nucleus will appear as moving, and, like any moving charge, it will produce a magnetic field \mathbf{H} . The magnetic field will affect the magnetic moment $\boldsymbol{\mu}$ of the electron. The contribution thereby made to the electron energy depends on the orientation of $\boldsymbol{\mu}$, and \mathbf{H} and is equal to $-\boldsymbol{\mu}\cdot\mathbf{H} = -\mu_{\cdot}\mathbf{H}$. Since the projection of the magnetic moment $\boldsymbol{\mu}$, on the vector of the field \mathbf{H} can assume two values ($\pm\hbar/2$, where \hbar is Planck's constant), the spin-orbit coupling leads to the splitting of energy levels in the hydrogen atom and in hydrogen-like atoms into two close-lying sublevels (a doublet structure). For atoms with more than one electron, a complicated multiple splitting of energy levels occurs.

2.2.5 Effective Mass of the charge carriers

The idea of effective mass bridges the gap between quantum mechanics and Newton's equations of motion. The particles, electrons and holes, are viewed as free particles inside a crystal when there is no external field. The effective mass of a particle indicates the particle's responsiveness to external influences. It does not take into consideration the material's intrinsic forces, such as atom-electron interaction. The parabolic dispersion approximation to the band structure is used to get the formula for effective mass. The following is the formula for the inverse effective mass tensor:

$$\frac{1}{\mathbf{m}^*} = \frac{1}{\hbar^2} \cdot \begin{bmatrix} \frac{d^2 \varepsilon_n(k)}{dk_x^2} & \frac{d^2 \varepsilon_n(k)}{dk_x dk_y} & \frac{d^2 \varepsilon_n(k)}{dk_x dk_z} \\ \frac{d^2 \varepsilon_n(k)}{dk_y dk_x} & \frac{d^2 \varepsilon_n(k)}{dk_y^2} & \frac{d^2 \varepsilon_n(k)}{dk_y dk_z} \\ \frac{d^2 \varepsilon_n(k)}{dk_z dk_x} & \frac{d^2 \varepsilon_n(k)}{dk_z dk_y} & \frac{d^2 \varepsilon_n(k)}{dk_z^2} \end{bmatrix} \quad (2.49)$$

Here, k_x , k_y and k_z refer to the direction in the reciprocal Cartesian space. And $\varepsilon_n(\mathbf{k})$ is the dispersion relation for the n th energy band.

2.2.6 Acoustic phonon limited charge carrier mobility

The scattering by acoustic phonons is intrinsic to the semiconductor and cannot be eliminated. The free electrons in covalent semiconductor like Si, Ge, etc. interact dominantly only with acoustic phonons through deformation potential. The momentum relaxation times for acoustic phonon scattering can be calculated according to traditional theory both for parabolic as well as non-parabolic band structure. The acoustic mode lattice vibration induced changes in lattice spacing, which change the band gap from point to point. Since the crystal is "deformed" at these points, the potential associated is called the deformation potential. Using the corresponding relaxation time for parabolic band structure, the mobility associated with the deformation potential scattering can be written as

$$\mu_{DP}^{\rho}(T_L) = A_1 T_L^{-3/2} \quad (2.50)$$

Where A_1 is the deformation potential constant which depends on average sound velocity in crystal and Boltzmann's constant and ρ is the crystal mass density.

2.2.7 Optical Properties

The dielectric function determines the majority of a material's optical characteristics. The dielectric function can readily determine all other parameters such as absorption coefficient, reflectance, transmittance, refractive index, and so on. The absorption coefficient is a measurement of how well a material converts electromagnetic energy, such as light energy, into internal energy, such as electrical or heat energy. The frequency dependent dielectric function may be calculated using DFT by forming the necessary tensor from the transition between the conduction and valence bands. The additional beneficial features are generated as a result of this.

2.2.8 Transmission function and Current-Voltage characteristics

Transmission and current are calculated by using the NEGF formalism. The electrostatic potential that is passed to the NEGF solver is calculated self-consistently with the quantum charge obtained from a previous NEGF calculation. Once the quantum charge and potential have converged, the transmission and current from the last NEGF calculation are treated as the result. Once the quantum charge density for the non-equilibrium and the equilibrium reservoir region is obtained, it is concatenated with the semiclassical density obtained for the at band region in the terminals. From this charge profile, a quasi-Fermi level is extracted and a semiclassical density-Poisson self-consistent calculation is carried out. The transmission function can be calculated by the multiplication of the number of modes and transmission probability. Then the current can be computed using the Green's function and transmission function.

CHAPTER 3

Structural and Computational Details

In the first section of this chapter, the structure of the novel hybrid monolayers of Si, Ge, and Sn atoms namely, $\text{Si}_x\text{Ge}_y\text{Sn}_{1-x-y}$ are discussed. In the next section, detailed computational methods for the characterization of structural, electronic, optical, and electron transport properties of the structures are delineated. Moreover, methodologies and applied parameters for determining electronic, optical, and transport properties i.e. band structure, DOS, effective mass, mobility, charge density, dielectrics, transport characteristics are also discussed in brief.

3.1 Structural Details

3.1.1 $\text{Si}_x\text{Ge}_y\text{Sn}_{1-x-y}$ monolayers

Novel hybrid monolayers of Si, Ge, and Sn atoms shares the similar structures with graphene analogues of Si, Ge, and Sn atoms namely silicene, germanene, and stanene respectively. Three different atomically thin alloys have been considered here based on relative proportion of the constituent atoms. While the elemental analogues of graphene consist of only one type of atom (Si or Ge or Sn), the exception of three kinds of atoms in $\text{Si}_x\text{Ge}_y\text{Sn}_{1-x-y}$ monolayers breaks the inversion symmetry and gives rise to interesting properties for these monolayers. All these hybrid monolayers are buckled honeycomb structures, which are defined as a hexagonal unit cell with eight atoms. Figure 3.1(a) and 3.1(d) show the top and side views of $\text{Ge}_{0.25}\text{Sn}_{0.25}\text{Si}_{0.50}$ monolayer respectively which consists of 25% Ge, 25% Sn and 50% Si atoms. Similarly, Figure 3.1(b) and 3.1(e) show the top and side views of $\text{Si}_{0.25}\text{Ge}_{0.25}\text{Sn}_{0.50}$ monolayer respectively consisting which consists of 25% Si, 25% Ge and 50% Sn atoms and Figure 3.1(c) and 3.1(f) show the top and side views, respectively of $\text{Sn}_{0.25}\text{Si}_{0.25}\text{Ge}_{0.50}$ monolayer which consists of 25% Sn, 25% Si and 50% Ge atoms.

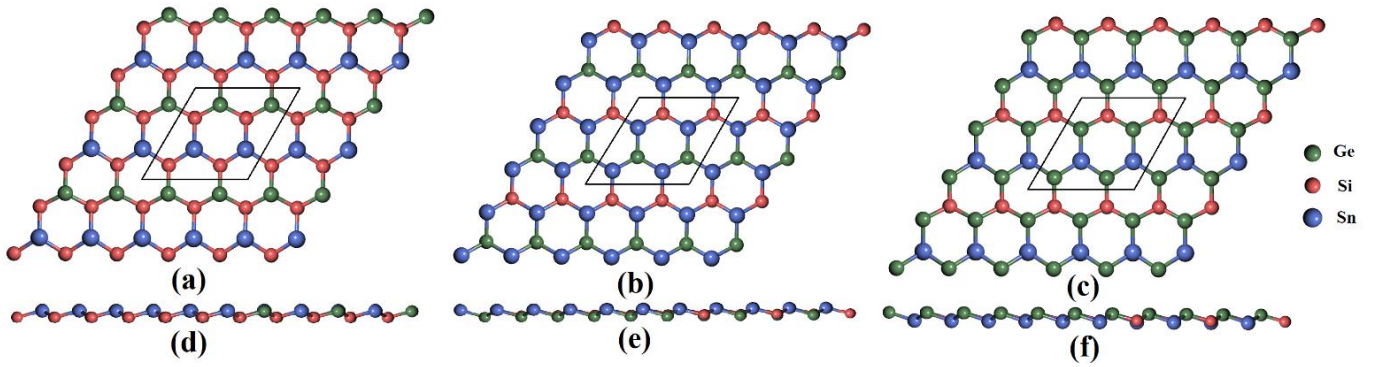


Figure 3.1: Top and side view of monolayer hybrid structures of Si, Ge and Sn. Fig. 3.1(a), (b), (c) represent top views and Fig.3.1(d), (e), (f) represents side views of $\text{Ge}_{0.25}\text{Sn}_{0.25}\text{Si}_{0.50}$, $\text{Si}_{0.25}\text{Ge}_{0.25}\text{Sn}_{0.50}$ and $\text{Sn}_{0.25}\text{Si}_{0.25}\text{Ge}_{0.50}$ respectively. The black hexagons represent the unit cells.

3.2 Computational Methodology

3.2.1 DFT simulation tools and parameters

For structural and electronic calculations, First Principles calculations are carried out using the Density Functional Theory (DFT) [102] framework, which is implemented in the *Quantum Espresso (QE) software package* [103], while optical calculations are carried out using the *Cambridge Serial Total Energy Package (CASTEP)* [104]. Without Spin-Orbit coupling, scalar relativistic ultrasoft pseudopotentials with nonlinear core correction were employed, and complete relativistic projected augmented wave pseudopotentials were used to include Spin-Orbit coupling. Both QE and CASTEP are well-known for their computational material science studies. The following are the key reasons for selecting these softwares:

- These are two of the best electronic structure calculation and material modeling packages which are freely available to researcher around the world under the terms of the GNU General Public License.
- These softwares are equipped with multi-threading tools to run on multiple processors and GPU (graphics processing unit) which is necessary to handle the large data and computational complexity related with the simulation.

- They come with large varieties of exchange-correlation functionals and suitable pseudo-potentials for DFT and MD calculations.
- The acceptance of these tools is quite high in comparison to the other free electronic structure calculation software.
- They can provide results with similar accuracy as compared to the renowned and widely accepted DFT calculation software Vienna ab initio simulation package (VASP).

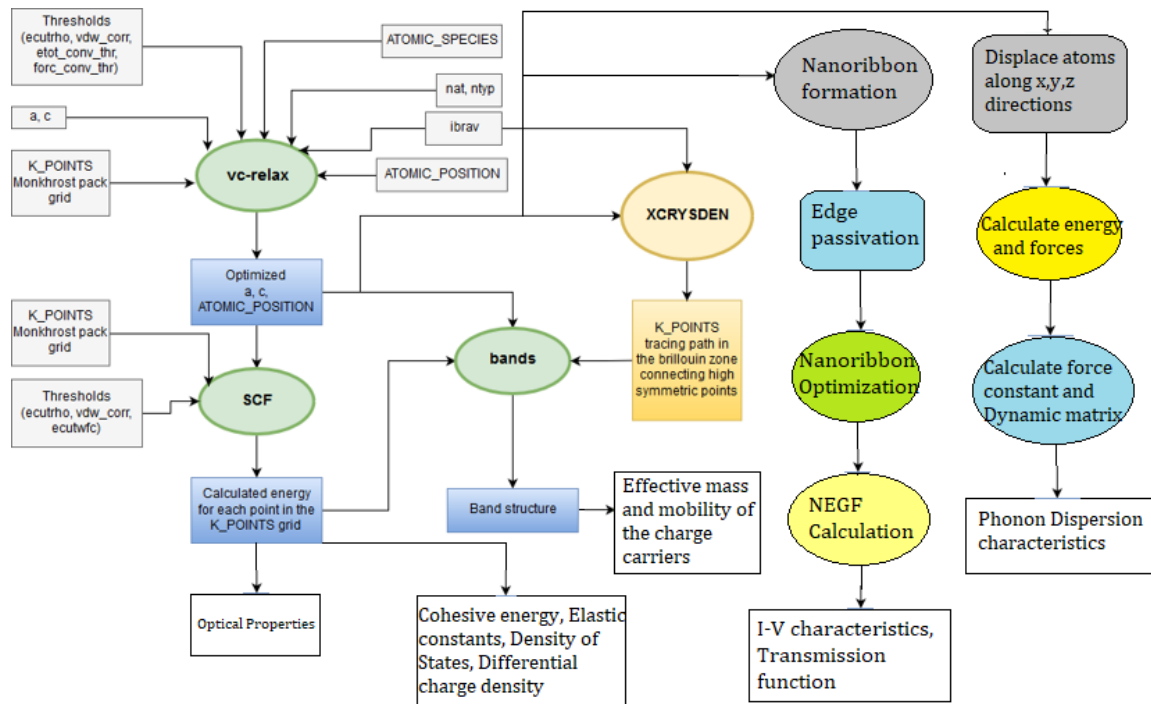


Figure 3.2: Flowchart of computational method

Figure 3.2 briefly describe the processes involved in the computations. For electronic structure computations, ultrasoft type pseudopotentials were utilized without taking into account Spin-Orbit coupling. Scalar relativistic techniques are used to construct these pseudopotentials, which incorporate nonlinear core correction. When computations including Spin-Orbit coupling need completely relativistic treatment of the atoms with non-linear core correction, Projected Augmented Wave (PAW) type pseudopotentials have been used. All of them are from the Quantum Espresso and CASTEP PS library. The generalized gradient approximation (GGA) inside the Perdew-Burke-Ernzerhof (PBE) [105], [106]

functional is used to account for exchange-correlation effects between valence band electrons. As previously documented in the literature [107], PBE is well-known for delivering great outcomes for alloy systems. The Broyden-Fletcher-Goldfarb-Shanno (BFGS) [108] minimal energy structure optimization approach is used. Even for non-smooth examples, BFGS, an iterative approach for tackling unconstrained nonlinear optimization problems, works pretty well. Table 3.1 summarizes all of the parameters that were used.

Table 3.1: Used parameters and their values in DFT calculation

Parameter	Value
Exchange-correlation	GGA
Pseudopotential (without SOC)	Scalar Relativistic Ultrasoft
Pseudopotential (with SOC)	Full Relativistic PAW
Functional	PBE
Optimization	BFGS

3.2.2 Structure Optimization

Optimized structures are obtained by performing variable cell relaxation (vc-relax). This method has been widely used to calculate the optimized electronic structures of Group-IV elemental and hybrid monolayers [20]. The steps involved in this process are given below:

- i. At first, the completely variable cell relaxed structures of novel hybrid monolayers of Si, Ge, and Sn atoms are calculated. As the initial guess, the $2 \times 2 \times 1$ supercell pristine monolayers are used.
- ii. Next, using both cell parameters for each monolayer self-consistent field calculations are performed. The structures obtained from vc-relax serve as the basis for futher calculation.
- iii. Finally, after the SCF calculations are completed, the structural, electronic and optical properties of the systems are extracted.

The value of energy cutoff was set to 640 eV for the expansion of plane wave function. The Brillouin zone (BZ) integration is sampled by $8 \times 8 \times 1$ K-points for structural

optimization and $10 \times 10 \times 1$ K-points for electronic and optical calculations within the Monkhorst-Pack scheme. The convergence tolerance of the self-consistent calculations in energy change is set to 13.6×10^{-6} eV for all calculations. All structural optimizations are carried out until the force on each atom is less than 0.0025 eV/Å. Periodic boundary condition is employed along the in-plane directions and a vacuum region of 30 Å is placed along perpendicular direction between two adjacent monolayers to eliminate the interaction between the periodic images. The unit cell of $\text{Ge}_{0.25}\text{Sn}_{0.25}\text{Si}_{0.50}$ monolayer contains 8 atoms; four Si, two Sn and two Ge atoms. Similarly, the unit cell of $\text{Si}_{0.25}\text{Ge}_{0.25}\text{Sn}_{0.50}$ monolayer contains 8 atoms; four Sn, two Si and two Ge atoms and the unit cell of $\text{Sn}_{0.25}\text{Si}_{0.25}\text{Ge}_{0.50}$ monolayer contains 8 atoms; four Ge, two Si and two Sn atoms. All these parameters along with other necessary ones for calculation are listed in Table 3.2.

Table 3.2: Used parameters and their values in for structure optimization

Parameter	Value
Kinetic energy cutoff	640 eV
Energy threshold	13.6×10^{-6} eV/ <i>unit cell</i>
Force threshold	0.0025 eV/Å
MP grid	$10 \times 10 \times 1$
Mixing factor	0.7
Electron convergence threshold	10^{-6}
Cell factor	8

Another important consideration is that in the case of vc-relax calculation no constraint was placed along any direction.

3.2.3 In-Plane Elastic Constants

The elastic constants are calculated using the stress-strain relationship for 2D materials which is shown in the following matrix form [109].

$$\begin{bmatrix} \sigma_1 \\ \sigma_2 \\ \sigma_3 \end{bmatrix} = \begin{bmatrix} C_{11} & C_{12} & 0 \\ C_{12} & C_{22} & 0 \\ 0 & 0 & \frac{(C_{11}-C_{12})}{2} \end{bmatrix} \begin{bmatrix} \varepsilon_1 \\ \varepsilon_2 \\ \varepsilon_3 \end{bmatrix} \quad (3.1)$$

where σ , C_{ij} and ε represent in-plane stress, elastic constants, and strain, respectively. Then the in-plane Young's modulus, Y_s and the Poisson's ratio, ν are computed from the following equations [110].

$$Y_s = (C_{11} - C_{12}) / C_{11} \quad (3.2)$$

$$\nu = C_{12} / C_{11} \quad (3.3)$$

3.2.4 Cohesive Energy

Cohesive energies of the hybrid monolayers are computed using the following formula.

$$E_{cohesive} = E_{Hybrid\ monolayer} - E_{Si} - E_{Ge} - E_{Sn} \quad (3.4)$$

Here, $E_{Hybrid\ monolayer}$ is the total energy of the hybrid monolayer, and E_{Si} , E_{Ge} , E_{Sn} are the total energy of the monolayer if Si, Ge, or Sn atoms are considered separately in the lattice structure. The negative values of the cohesive energy indicate the thermodynamic stability of these structures, the more negative the cohesive energy is, the more stable the structure is.

3.2.5 Phonon Dispersion Calculation

Phonons of a nonzero wavevector play an important role in the thermophysical properties of crystalline solids and the physics of many solid-state phase transitions. Proving the mechanical stability of a crystal structure by testing for real frequencies requires a vibrational calculation over the full Brillouin Zone. Phonon calculation consists of more than one stage, the usual sequence being a geometry optimization followed by the phonon calculation itself. The structures are geometrically optimized to energy minimum structures - the energy expansion in lattice dynamics makes the explicit assumption that the system is in mechanical equilibrium and that all atomic forces are zero. If a lattice dynamics calculation is performed at the configuration which minimizes the energy the force constant matrix $\Phi_{\kappa,\kappa'} \alpha,\alpha'$ is positive definite, and all of its eigenvalues are positive. Consequently,

the vibrational frequencies which are the square roots of the eigenvalues are real numbers. If on the other hand the system is not at a minimum energy equilibrium configuration $\Phi_{\kappa, \kappa'}$, α, α' is not necessarily positive definite, the eigenvalues may be negative. In that case the frequencies are imaginary and do not correspond to a physical vibrational mode.

3.2.6 Band Structure Calculation

The Self Consistent Field (SCF) computation is used to produce the essential wavefunctions for computing the band structures of the unique hybrid monolayers of Si, Ge, and Sn atoms. This option for occupation is temporal smearing, which incorporates the temperature impact in the DFT computation by spreading or smearing the energy over multiple occupation levels. With a degauss value of 0.02 and Methfessel-Paxton first-order spreading [111], In each iteration, the wave-function was calculated using the mixing mode of 'plain' and a mixing beta of 0.7. Later, a high-verbosity 'bands' computation is used to obtain the data needed for band visualization. The path of integration in the first Brillouin zone is along $\Gamma \rightarrow M \rightarrow K \rightarrow \Gamma$.

3.2.7 Density of States and Atom Projected Density of States

Quantum Espresso's post-processing tools `dos.x` and `projwfc.x` were used to calculate density of states (DOS) and partial density of states (PDS) (PDOS). The occupancy parameter is specified as `tetrahedra` [112], which differs from the band structure and DOS computation. Another thing worth highlighting is that the degauss factor is lowered to 0.004 to prevent PDOS smearing or spreading for each atomic orbital. The collected numbers may then be further analyzed with *MATLAB* scripts to gain more insights into the data.

3.2.8 Differential Charge Density

`pp.x`, a Quantum Espresso post processing tool capable of creating charge density for atomic structures, was used to calculate charge density. The differential charge density $\Delta\rho$ is calculated as follows:

$$\Delta\rho = \rho_{\text{Hybrid Monolayer}} - \rho_{\text{Si}} - \rho_{\text{Ge}} - \rho_{\text{Sn}} \quad (3.5)$$

Where, $\Delta\rho$ is the differential charge density, $\rho_{\text{Hybrid Monolayer}}$ is charge density of the hybrid monolayers of Si, Ge, Sn, and ρ_{Si} , ρ_{Ge} and ρ_{Sn} are charge densities of isolated Si, Ge, and Sn atoms respectively. The difference charge density can then be found in every grid point using *pp.x*. *VESTA* [113] software is used to produce difference charge density iso-surface plots.

3.2.9 Spin-Orbit Coupling (SOC) incorporation

To incorporate Spin-Orbit coupling in SCF calculation Projected Augmented Wave (PAW) pseudopotentials with full relativistic treatment of atoms were utilized. Nonlinear calculations were performed by setting 'lspinorb' to 'true' to account SOC into calculation. Again, *smearing* has been used as the value for *occupation* parameter for band structure and DOS calculation, respectively.

3.2.10 Effective Mass of the charge carriers

The parabolic character of the conduction band minima (CBM) and valence band maxima (VBM) is implicit in the formula for effective mass of electron and hole (VBM). In fact, a considerable region in reciprocal space between the two extreme points does not always represent parabolic nature fully. Another issue is that at its most extreme points, the curvature may not give useful results. For all semiconducting structures in our simulation, the Fermi-energy level is located between the conduction and valence bands. As a result, the electron concentration in the VBM and CBM is increased. To compute the effective mass of an electron, the entire system must take into account the curvature of a large region surrounding CBM. In this case, parabolic fitting across the ideal area surrounding those extreme points is recommended.

When examining the parabolic fitting, another issue arises. For parabola, the distance between the sampled k-points must be carefully evaluated. The quantity of k-points plays a significant influence as well. Furthermore, there is no limitation on the minimum point in the generic parabola fitting approach. As a result, the constraint has been set to mean square minimization for parabola fitting. The constraint pins the computed parabola's

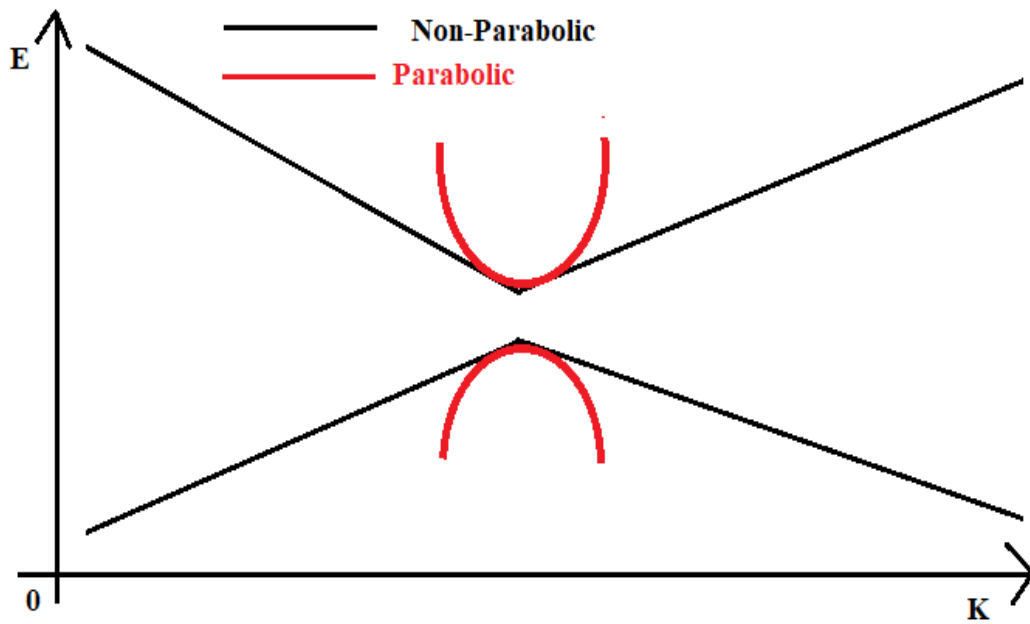


Figure 3.3: A visual representation of parabolic approximation of non-parabolic band structure for performing the effective mass calculation.

minima/maxima to the same place as CBM/VBM, resulting in a better parabolic approximation by include the true position of CBM/VBM in the computation.

To meet the aforementioned conditions, a method has been built that uses the VBM/CBM as an input to produce the appropriate k-points around the VBM/CBM. The parabolic fitting is then done by reducing the mean square error. This has been cleverly implemented by allowing the user to adjust the number of points and the distance between the k-points using a slider, as illustrated in Figure 3.3. The visual help, together with the slider, makes selecting the suitable parabola a breeze. The code's output has been compared to the effective mass of graphene. For this calculation, a great agreement has been reached.

3.2.11 Acoustic phonon limited mobility of charge carriers

Using the calculated values of effective mass of the charge carriers and by applying Deformation Potential theory as proposed by Bardeen and Shockley [93], [114], we have computed the acoustic phonon limited mobility of the charge carriers in our novel hybrid

monolayers of Si, Ge and Sn. The mobility of the charge carriers in the monolayers is calculated using the following formula [115].

$$\mu_{2D} = \frac{e\hbar^3 C_{2D}}{3K_B T m^* m_d (E^i)^2} \quad (3.6)$$

Where, e is the charge of an electron, \hbar is the reduced Planck's constant, K_B is the Boltzmann's constant, T is the absolute temperature considered as 300K, m^* and m_d are effective mass and average effective mass of the charge carrier respectively. E^i is the rate of change of conduction band minimum (CBM) or valence band maximum (VBM) as a function of strain which are computed by calculating the slope of the CBM or VBM with respect to applied strain. C_{2D} is the elastic modulus along the direction of applied stress which is calculated using the following formula [115].

$$\frac{2(E-E_0)}{S_0} = C_{2D} \times \left(\frac{\Delta l}{l_0}\right)^2 \quad (3.7)$$

Where, E_0 is the ground state energy and E is the energy of the monolayer under tensile strain. S_0 is the area of the relaxed unit cell and $\frac{\Delta l}{l_0}$ is the amount of tensile strain with respect to relaxed condition.

3.2.12 Optical Properties

Optical properties are computed by calculating the complex dielectric function $\epsilon(\omega) = \epsilon_1(\omega) + i \epsilon_2(\omega)$ first [116]. The imaginary part of the dielectric function is calculated using the following formula.

$$\epsilon_2(\omega) = \frac{2e^2\pi}{\Omega\epsilon_0} \sum_{k,v,c} |\langle \psi_k^c | \mathbf{u} \cdot \mathbf{r} | \psi_k^v \rangle|^2 \delta(E_k^c - E_k^v - \hbar\omega) \quad (3.8)$$

where, ϵ_0 is the dielectric constant of the vacuum and Ω represents the volume of the crystal. $\hbar\omega$ and \mathbf{u} represent the energy and the polarization direction of the incident photon respectively. The superscripts c and v imply the conduction and valence bands respectively. The E_k and ψ_k represent the energy and the wavefunction at the k point of conduction or valence band. The real part of the dielectric function is calculated applying Kramer's-Kronig relation using the imaginary part of the dielectric function.

$$\varepsilon_1(\omega) = 1 + \frac{2}{\pi} P \int_0^{\infty} \frac{\varepsilon_2(\omega') \omega'}{\omega'^2 - \omega^2} d\omega' \quad (3.9)$$

Where P represents the principal value of the integral. The complex refractive index, $N=n(w)+ik(w)$ is calculated using the complex dielectric function by applying the following formula.

$$\varepsilon(\omega) = \varepsilon_1(\omega) + i \varepsilon_2(\omega) = N^2 \quad (3.10)$$

$$\varepsilon_1(\omega) = n(w)^2 - k(w)^2 \quad (3.11)$$

$$\varepsilon_2(\omega) = 2n(w)k(w) \quad (3.12)$$

Optical conductivity $\sigma(\omega)$, absorption coefficient $\alpha(\omega)$, reflectivity $R(\omega)$ and electron loss function $L(\omega)$ are computed using the following formula.

$$\sigma(\omega) = -i \frac{2\omega}{4\pi} (\varepsilon(\omega) - 1) \quad (3.12)$$

$$\alpha(\omega) = \frac{\sqrt{2\omega}}{c} [\{\varepsilon_1(\omega)^2 + \varepsilon_2(\omega)^2\}^{\frac{1}{2}} - \varepsilon_2(\omega)]^{\frac{1}{2}} \quad (3.13)$$

$$R(\omega) = \left| \frac{\sqrt{\{\varepsilon_1(\omega) + i \varepsilon_2(\omega)\}} - 1}{\sqrt{\{\varepsilon_1(\omega) + i \varepsilon_2(\omega)\}} + 1} \right|^2 \quad (3.14)$$

$$L(\omega) = \text{Im}\left(-\frac{1}{\varepsilon(\omega)}\right) \quad (3.15)$$

3.2.13 Electron Transport Properties

Electron transport calculations are carried out based on Non-Equilibrium Green's Function (NEGF) within Density Functional Theory using *DMOL3* code [117]. The 'DFT Semi-core pseudopotentials' is taken as core treatment and calculations are carried out using Double Numeric Plus (DNP) basis set. Generalized Gradient Approximation (GGA) with the Perdew–Burke–Ernzerhof (PBE) is used to describe the exchange correlation interaction with a basis cut-off of 3.5 Å [105] [106]. Geometric optimization was carried out before calculation as described previously, and when NH₃ atoms are introduced, they were also geometrically relaxed on the nanoribbons.

CHAPTER 4

Results and Discussion

In this chapter, the structural, electronic, optical, and electron transport properties of three different novel hybrid monolayers of Si, Ge, and Sn atoms are characterized and the results are validated with previously reported literatures. For structural properties, optimized lattice constants, buckling height, bond length were calculated. To examine mechanical and dynamical stability of the structures in-plane lattice constants, phonon dispersion curves and cohesive energy were calculated. Energy band structure with and without considering Spin-Orbit coupling, effective mass, acoustic phonon limited charge carrier mobility, density of states, and differential charge density were computed to characterize the electronic properties of each monolayer. Then dielectric constant, absorption coefficient, electron energy loss function, optical conductivity, refractive index and reflectivity were analyzed to understand the optical properties. To characterize electron transport properties and sensing application of the monolayers transmission function and I-V characteristics were calculated for pristine monolayer, NH₃ adsorbed monolayer, and monolayers with point defects.

4.1 Geometrically Optimized Structures

First, the structural properties of the novel hybrid monolayers of Si, Ge, and Sn are investigated. Three different hybrid monolayers of Si, Ge, and Sn which are different in their relative atomic proportions have been studied. All the hybrid monolayers are buckled honeycomb structures, which are defined as a hexagonal unit cell with eight atoms. Figure 3.1(a) and 3.1(d) show the top and side views of Ge_{0.25}Sn_{0.25}Si_{0.50} monolayer respectively which consists of 25% Ge, 25% Sn and 50% Si atoms. After complete geometric optimization of the system, the computed lattice constant is 8.19 Å, bond length of Sn-Si and Ge-Si are 2.51 Å, 2.39 Å, respectively and buckling height of Sn-Si and Ge-Si are 0.67 Å and 0.63 Å, respectively. Similarly, Figure 3.1(b) and 3.1(e) show the top and side views of Si_{0.25}Ge_{0.25}Sn_{0.50} monolayer respectively consisting which consists of 25% Si, 25% Ge

and 50% Sn atoms and Figure 3.1(c) and 3.1(f) show the top and side views, respectively of $\text{Sn}_{0.25}\text{Si}_{0.25}\text{Ge}_{0.50}$ monolayer which consists of 25% Sn, 25% Si and 50% Ge atoms.

The value of different computed parameters after complete geometric relaxation of the three hybrid structures are listed in the Table 4.1. These computed values of the lattice constants of all the hybrid monolayers of Si, Ge, and Sn are consistent with the calculated values derived from Vegard's law considering the reported lattice constants of monolayer SiSn, GeSn and SiGe. To confirm this claim, lattice constants of the proposed hybrid monolayers have been calculated using the reported lattice constants of monolayer hybrids of SiGe, SiSn and GeSn as 3.963 Å, 4.29 Å, and 4.35 Å, respectively [118]-[121]. So, employing Vegard's law the calculated values of the lattice constant of monolayer $\text{Ge}_{0.25}\text{Sn}_{0.25}\text{Si}_{0.50}$, $\text{Si}_{0.25}\text{Ge}_{0.25}\text{Sn}_{0.50}$, and $\text{Sn}_{0.25}\text{Si}_{0.25}\text{Ge}_{0.50}$ are 8.253 Å, 8.64 Å, and 8.313 Å, respectively which are very close to the computed values of the lattice constants of the hybrid monolayers. If the hybrid monolayers are closely observed, there is a slight compression in the Sn-Si, Sn-Ge bonds and slight tensile stress in the Ge-Si bonds. This is due to the presence of Sn atoms which possess comparatively low electron affinity and low ionization energy than Si and Ge atoms. The bond length between Si-Ge, Ge-Sn, and Sn-Si are longer compared to that of graphene, and this longer bond length weakens the bonding between the π orbitals. Hence sp^2 hybrid orbitals further hybridize with the π orbitals, forming sp^2 - sp^3 like orbitals. This phenomenon is primarily responsible for the buckling structure of these hybrid monolayers [122], [123]. The optimized values of the structural properties are shown in Table 1.

4.2 Mechanical and dynamic stability

4.2.1 In-Plane Elastic Constants

The in-plane elastic constants (C_{11} , C_{12}), Young's modulus, Y_s and Poisson's ratio, ν of these novel hybrid monolayers of Si, Ge, and Sn atoms have been calculated and that are shown in Table 1. The positive values of in-plane lattice constants and Young's modulus of the structures indicate their mechanical stability. Tao *et al.* [124] reported mechanical stability of monolayer stanene following similar approach. For each of the monolayers, the

elastic constant along x direction, C_{11} is equal to the elastic constant along y direction, C_{22} which proves the isotropic in-plane stiffness of these materials [110]. The calculated values of these parameters are comparable to those of monolayer silicene, germanene, and stanene [110] [125]. The Young's modulus of monolayer $\text{Ge}_{0.25}\text{Sn}_{0.25}\text{Si}_{0.50}$, $\text{Si}_{0.25}\text{Ge}_{0.25}\text{Sn}_{0.50}$, and $\text{Sn}_{0.25}\text{Si}_{0.25}\text{Ge}_{0.50}$ derived from Vegard's law using the reported Young's modulus of silicene, germanene, and stanene [110] are 49.03, 45.53, and 39.57 N/m respectively which are close to our computed values.

Table 4.1: Structural properties of Novel Hybrid monolayers of Si, Ge and Sn and comparison with monolayer silicene, germanene, stanene, and graphene: Lattice constant (Å), bond length (Å), buckling height (Å), elastic constants, and cohesive energy (eV/ unit cell)

Structure	Atomic Proportion	Lattice Constant (Å)	Bond Length (Å)	Buckling Height (Å)	Elastic Constants		Young's modulus	Poisson's ratio	Cohesive Energy (eV/ unit cell)
					C_{11} (N/m)	C_{12} (N/m)	Y_s (N/m)	ν	
$\text{Ge}_{0.25}\text{Sn}_{0.25}\text{Si}_{0.50}$	Ge = 25%, Sn = 25%, Si = 50%	OA = 8.19602 OB = 8.17580 OC = 34.6128	Sn-Si = 2.518 Ge-Si = 2.396	Sn-Si = 0.6714 Ge-Si = 0.6395	63.93	20.72	56.96	0.33	-31.370
$\text{Si}_{0.25}\text{Ge}_{0.25}\text{Sn}_{0.50}$	Si = 25%, Ge = 25%, Sn = 50%	OA = 8.60555 OB = 8.59812 OC = 34.8955	Si-Sn = 2.569 Ge-Sn = 2.617	Si-Sn = 0.6496 Ge-Sn = 0.8305	48.53	13.27	50.01	0.37	-28.790
$\text{Sn}_{0.25}\text{Si}_{0.25}\text{Ge}_{0.50}$	Sn = 25%, Si = 25%, Ge = 50%	OA = 8.29414 OB = 8.25572 OC = 34.8512	Sn-Ge = 2.415 Si-Ge = 2.581	Sn-Ge = 0.6322 Si-Ge = 0.7807	52.62	18.03	43.62	0.31	-30.273
Silicene	Si = 100%	3.88 [110]	Si-Si = 2.27 [110]	Si-Si = 0.41 [110]	-	-	61.33 [110]	0.31 [110]	-
Germanene	Ge = 100%	4.03 [110]	Ge-Ge = 2.42 [110]	Ge-Ge = 0.68 [110]	-	-	42.05 [110]	0.33 [110]	-
Stanene	Sn = 100%	4.66 [110]	Sn-Sn = 2.83 [110]	Sn-Sn = 0.9 [110]	-	-	24.46 [110]	0.39 [110]	-
Graphene	C = 100%	2.46 [110]	C-C = 1.42 [110]	Planar	-	-	337.1 [110]	0.18 [110]	-

4.2.2 Phonon Dispersion Curves

In order to study the electronic and optical properties of the hybrid monolayers, it is necessary to investigate the structural stability of the nanostructures. The hybrid monolayers of group IV binary elements e.g. SiGe, SiSn, and GeSn are reported to have stable structures [121], [122]. In order to explore the stability of the novel hybrid monolayers, the phonon dispersion curves and cohesive energy of each of the monolayers

have been computed. From Figure 4.1 it is clear that all the branches possess positive vibrational frequency. The absence of imaginary frequencies in all of the branches of the phonon dispersion curves indicate that all the hybrid monolayers are dynamically stable. The phonon dispersion curves demonstrate 3 acoustical, and 21 optical branches. Among the three acoustical branches- LA, TA and ZA, the in-plane vibrational modes LA and TA show linear phonon dispersion near the Γ point, whereas the out of plane vibrational mode, ZA is quadratic near the Γ point, which indicates rapid attenuation of out of plane vibrational modes. Similar results are reported by Xu *et al.* for hybrid monolayers of Si, Ge and C [26].

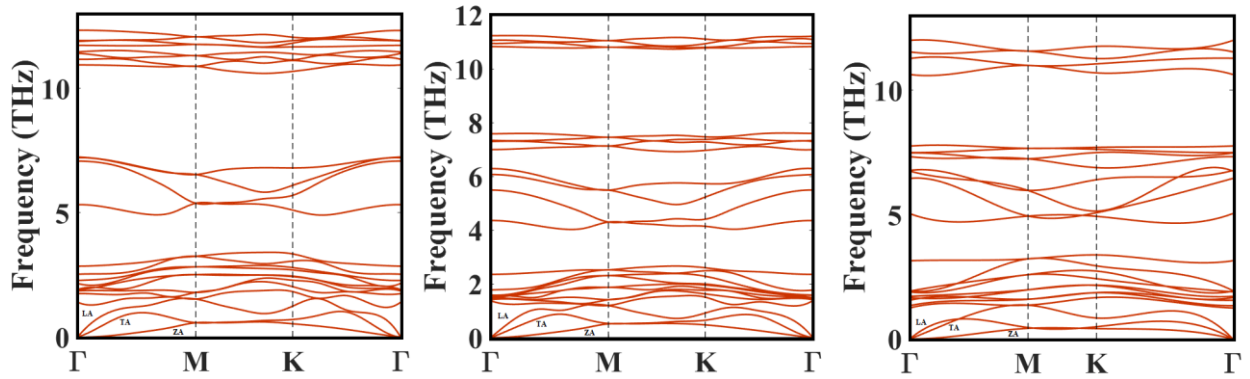


Figure 4.1: Phonon dispersion curves of monolayer hybrids of Si, Ge and Sn- (a) $\text{Ge}_{0.25}\text{Sn}_{0.25}\text{Si}_{0.50}$, (b) $\text{Si}_{0.25}\text{Ge}_{0.25}\text{Sn}_{0.50}$ and (c) $\text{Sn}_{0.25}\text{Si}_{0.25}\text{Ge}_{0.50}$ respectively.

4.2.3 Cohesive Energy

Furthermore, the cohesive energies of the hybrid monolayer have been calculated using the following formula.

$$E_{\text{cohesive}} = E_{\text{Hybrid monolayer}} - E_{\text{Si}} - E_{\text{Ge}} - E_{\text{Sn}} \quad (4.1)$$

Here, $E_{\text{Hybrid monolayer}}$ is the total energy of the hybrid monolayer, and E_{Si} , E_{Ge} , E_{Sn} are the total energy of the monolayer if Si, Ge, or Sn atoms are considered separately in the lattice structure.

The negative values of the cohesive energy indicate the thermodynamic stability of these structures, the more negative the cohesive energy is, the more stable the structure is [127].

The calculated values of cohesive energy of $\text{Ge}_{0.25}\text{Sn}_{0.25}\text{Si}_{0.50}$, $\text{Si}_{0.25}\text{Ge}_{0.25}\text{Sn}_{0.50}$ and $\text{Sn}_{0.25}\text{Si}_{0.25}\text{Ge}_{0.50}$ are -31.370, -28.790 and -30.273 eV/unit cell respectively as shown in Table 1. All the hybrid monolayers have significantly negative cohesive energy which indicates stable structures with strong atomic bonding. Among the three hybrid monolayers, $\text{Ge}_{0.25}\text{Sn}_{0.25}\text{Si}_{0.50}$ is comparatively more stable.

4.3 Electronic Properties

In this part the study, concentration will be given on the electronic properties of the novel hybrid monolayers of Si, Ge, and Sn. It is reported that graphene like 2D elemental monolayers of other group-IV materials (Si, Ge, Sn) are semimetallic with negligible energy bandgap at the K point of the Brillouin Zone (BZ) in their band structures [69]. These monolayers possess high electron mobility due to quantum confinement of the charge carriers along the plane and the presence of relativistic massless Dirac fermion which is discernible from the Dirac cone demonstrating the linear energy band dispersion relation around the K point of the Brillouin Zone (BZ). But the semimetallic property restricts their applications in the field of digital electronics. Moreover, the binary compound monolayers SiSn, GeSn, and SiGe also demonstrate similar band structures near K point of the BZ as reported by Fadaie *et al.* [118]. In the band structures of the monolayer SiSn and GeSn, there are energy bandgap opening at the K point of the BZ which is due to the breaking of the inversion symmetry.

4.3.1 Energy Band Structure

Calculations show that the hybrid ternary monolayers of Si, Ge, and Sn are semiconductors with direct energy bandgap at K point of the BZ and the presence of the Dirac cone at the K point indicates the presence of relativistic massless Dirac fermion. The breaking of the inversion symmetry in the lattice structure and strong spin-orbit coupling present in the Sn, Si, and Ge atoms are responsible for the energy splitting at K point [128]. During the simulation, the system relaxation was followed by a self-consistent field (scf) calculation and band-structure energy data was calculated with and without considering spin-orbit

coupling and plotted (E-k diagram) for equally spaced K point samples as shown in Figure 4.2.

The energy band structure of three hybrid monolayers without and with spin-orbit coupling (SOC) is shown in Figure 4.2(a), (d), (g) (blue color) and Figure 4.2(b), (e), (h) (red color) respectively and the magnified view of the bandstructures are shown in Figure 4.2(c), (f), (i). The Fermi level is set as the reference. As observed in Figure 4.2(a) and 3(b), there is a direct bandgap opening of 133 meV and 174 meV at K point of the BZ for the $\text{Ge}_{0.25}\text{Sn}_{0.25}\text{Si}_{0.50}$ monolayer, without and with considering the spin-orbit coupling respectively, and Figure 4.2(c) shows the band degeneracy in the conduction and valence band due to strong spin orbital interaction. Similar bandgap opening is also studied by Liu *et al.* and Khan *et al.* [129]-[131]. The figures also show that the linear band dispersion relation is well preserved near K point of the BZ. Shao *et. al.* calculated the values of charge carrier mobility in Silicene which shows similar linear energy band dispersion using First-Principles calculations [132] and a recent experiment has shown charge carrier mobility inside silicene field effect transistors is around $10^2 \text{ cm}^2\text{V}^{-1}\text{s}^{-1}$ [133] which is larger than many experimental mobility of 2D FETs and also this can be improved by creating more defect free materials. So, the presence of Dirac cone results in a semiconductor material with high mobility of the charge carriers [131], [134], [135]. For the $\text{Si}_{0.25}\text{Ge}_{0.25}\text{Sn}_{0.50}$ hybrid monolayer a similar direct energy bandgap of 242 meV (without spin-orbit coupling) and 283.8 meV (with spin-orbit coupling) are introduced at the K point of the BZ as shown in Figure 3(d) and 3(e), respectively. Linear band dispersion relation is also preserved with band degeneracy from spin orbital interaction as shown in Figure 4.2(f). A similar direct bandgap of 120 meV (without spin-orbit coupling) and 151 meV (with spin-orbit coupling) for the $\text{Sn}_{0.25}\text{Si}_{0.25}\text{Ge}_{0.50}$ hybrid monolayer is introduced at the K point of the BZ as shown in Figure 4.2(g) and 4.2(h), respectively preserving the linear energy band dispersion relation around the K point of the BZ with band degeneracy from spin orbital interaction as shown in Figure 4.2(i). The energy bandgap is found to increase with increasing proportion of Sn atoms. Hence, increasing proportion of Sn atoms encourages further energy bandgap due to its significant contribution to breaking of the inversion symmetry and strong spin orbital interaction. The energy bandgap of these novel hybrid monolayers of Si, Ge, and Sn atoms are also computed using Heyd–Scuseria–Ernzerhof (HSE) functionals. The shape of the bandstructures calculated using HSE functionals are

identical to those of using GGA-PBE functionals. The calculated energy bandgaps of $\text{Ge}_{0.25}\text{Sn}_{0.25}\text{Si}_{0.50}$, $\text{Si}_{0.25}\text{Ge}_{0.25}\text{Sn}_{0.50}$ and $\text{Sn}_{0.25}\text{Si}_{0.25}\text{Ge}_{0.50}$ using HSE hybrid functional are 194, 249, and 125 meV respectively which are close to the respective energy bandgaps calculated using GGA-PBE functionals. So, the reported electronic and optical properties of these novel hybrid monolayers are not largely underestimated if GGA-PBE functionals are used.

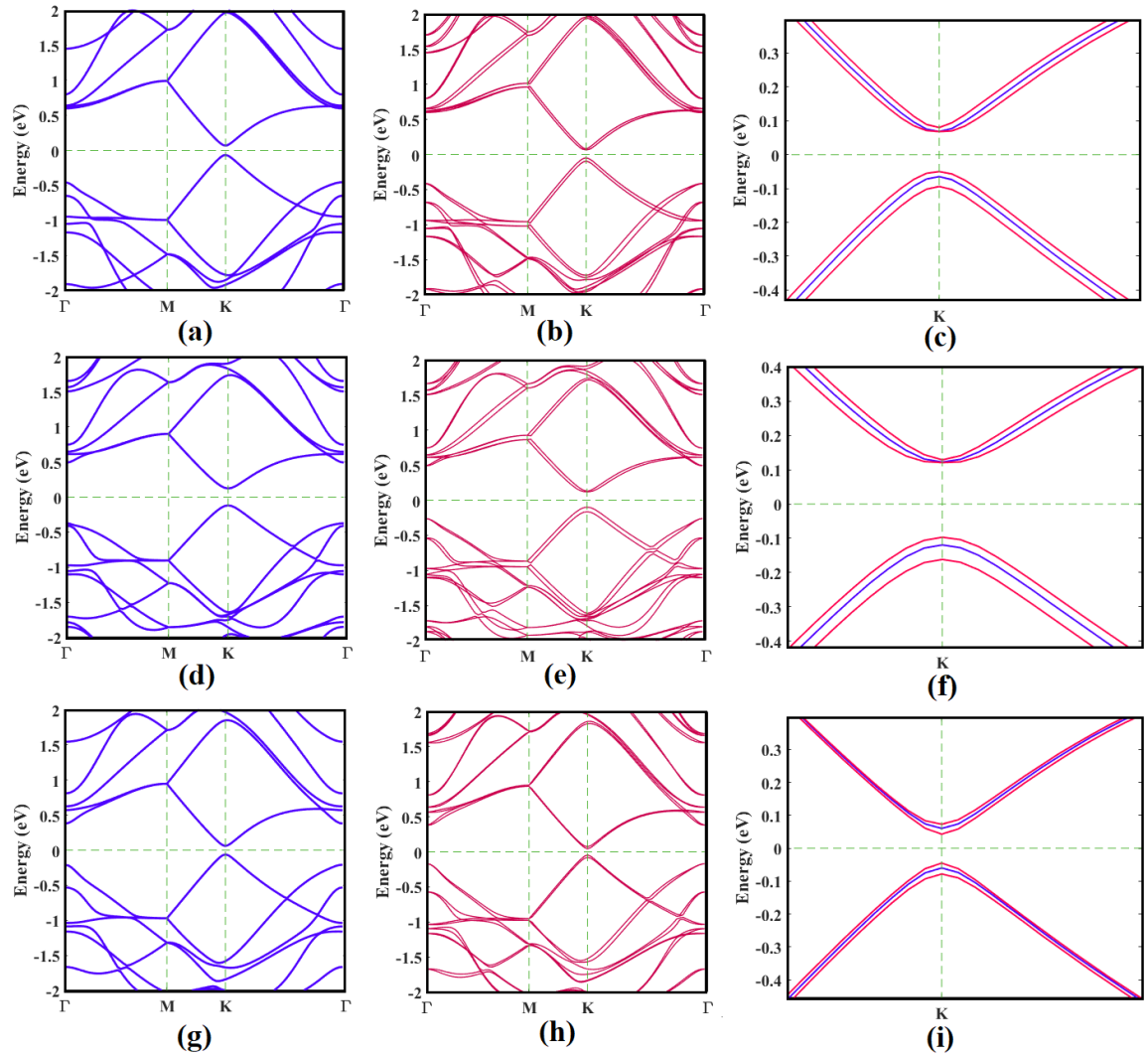


Figure 4.2: Electronic Band Structure of $\text{Ge}_{0.25}\text{Sn}_{0.25}\text{Si}_{0.50}$ (a) without SOC, (b) with SOC, (c) magnified view at K point; of $\text{Si}_{0.25}\text{Ge}_{0.25}\text{Sn}_{0.50}$ (d) without SOC, (e) with SOC (f) magnified view at K point; of $\text{Sn}_{0.25}\text{Si}_{0.25}\text{Ge}_{0.50}$ (g) without SOC, (h) with SOC, (i) magnified view at K point. The blue and red lines represent energy spectrum in the absence and presence of SOC respectively.

Jing Shi *et al.* [136] reported energy bandgaps of GeSi, SnSi, and SnGe monolayers using HSE and GGA-PBE functionals in a similar way. Table 4.2 summarizes the value of the energy bandgaps and conduction band and valence band energy splitting. Literatures reported similar kind of bandgap opening due to breaking of inversion symmetry and strong spin-orbit coupling [137]-[139]. These novel hybrid monolayers possess larger bandgap compared to other structures like graphene, silicene, germanene [139], [140].

4.3.2 Effective Mass of the Charge Carrier

Significant energy bandgap along with high carrier mobility due to the linear band dispersion relation near the K point of the BZ indicates possible applications in high speed nano-structured switching devices [141], [142]. The effective mass of the electron and hole at the K point of BZ have been calculated using parabolic band approximation. The calculated values of electron effective mass in $\text{Ge}_{0.25}\text{Sn}_{0.25}\text{Si}_{0.50}$, $\text{Si}_{0.25}\text{Ge}_{0.25}\text{Sn}_{0.50}$, and $\text{Sn}_{0.25}\text{Si}_{0.25}\text{Ge}_{0.50}$ are $0.065 \times m_0$, $0.101 \times m_0$, $0.063 \times m_0$, respectively, where m_0 is the mass of the rest electron. And the calculated values of hole effective mass in $\text{Ge}_{0.25}\text{Sn}_{0.25}\text{Si}_{0.50}$, $\text{Si}_{0.25}\text{Ge}_{0.25}\text{Sn}_{0.50}$, and $\text{Sn}_{0.25}\text{Si}_{0.25}\text{Ge}_{0.50}$ as a function of rest mass of electron are $0.063 \times m_0$, $0.97 \times m_0$, $0.061 \times m_0$, respectively. These results demonstrate a very small effective mass [143] of electron and hole which in turn result in higher charge carrier mobility as reported in literatures [130], [133].

4.3.3 Acoustic Phonon limited Charge Carrier

The calculated values of acoustic phonon limited electron mobility of $\text{Ge}_{0.25}\text{Sn}_{0.25}\text{Si}_{0.50}$, $\text{Si}_{0.25}\text{Ge}_{0.25}\text{Sn}_{0.50}$, and $\text{Sn}_{0.25}\text{Si}_{0.25}\text{Ge}_{0.50}$ monolayers are 7.556×10^6 , 6.847×10^5 , and $5.504 \times 10^5 \text{ cm}^2\text{v}^{-1}\text{s}^{-1}$, respectively. And the acoustic phonon limited hole mobility of $\text{Ge}_{0.25}\text{Sn}_{0.25}\text{Si}_{0.50}$, $\text{Si}_{0.25}\text{Ge}_{0.25}\text{Sn}_{0.50}$ and $\text{Sn}_{0.25}\text{Si}_{0.25}\text{Ge}_{0.50}$ monolayers are 5.058×10^6 , 5.49×10^5 , and $1.852 \times 10^5 \text{ cm}^2\text{v}^{-1}\text{s}^{-1}$, respectively. The results are summarized in the Table 4.2. The difference in energy as function of tensile strain is plotted in Figure 4.3(d), (e), (f) and C_{2D} is computed from the fitting parameter of the energy versus strain curve. As predicted earlier, the charge carriers' mobility in our proposed hybrid monolayers are

significantly higher and in agreement with the studies carried out on the charge carrier mobility by Zhou *et al.* [144].

Table 4.2: Electronic properties of Novel Hybrid monolayers of Si, Ge and Sn and comparison with similar 2D materials: Energy bandgap (with and without SOC), Energy band splitting due to SOC, effective mass and acoustic phonon limited mobility of the charge carrier.

Structure	Bandgap (GGA-PBE) without SOC (meV)	Bandgap (HSE) without SOC (meV)	Bandgap with SOC (meV)	Band Splitting at K point due to SOC (meV)	Effective Mass of Electron (m/m ₀)	Effective Mass of Hole (m/m ₀)	Electron Mobility (cm ² V ⁻¹ s ⁻¹)	Hole Mobility (cm ² V ⁻¹ s ⁻¹)
Ge _{0.25} Sn _{0.25} Si _{0.50}	133	194	174	CB = 12 VB = 44	0.065	0.063	7.556×10 ⁶	5.058×10 ⁶
Si _{0.25} Ge _{0.25} Sn _{0.50}	242	249	283.8	CB = 8 VB = 65	0.101	0.097	6.847×10 ⁵	5.49×10 ⁵
Sn _{0.25} Si _{0.25} Ge _{0.50}	120	125	151	CB = 30 VB = 33	0.063	0.061	5.504×10 ⁵	1.852×10 ⁵
Si _{0.50} Sn _{0.50}	210 [118]	-	-	-	-	-	-	-
Ge _{0.50} Sn _{0.50}	230 [118]	-	-	-	-	-	-	-
Silicene	-	-	-	-	First-Principles [132]		2.75×10 ⁵	2.22×10 ⁵
					Experimental [133]		10 ²	10 ²

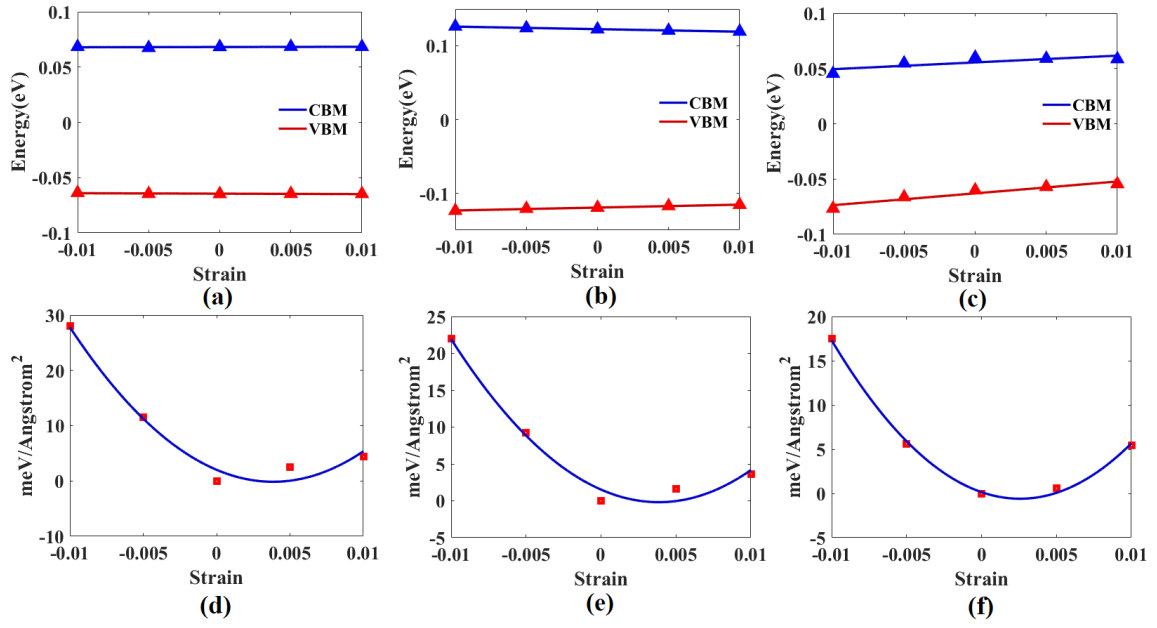


Figure 4.3: Change of CBM and VBM as a function of strain for (a) $\text{Ge}_{0.25}\text{Sn}_{0.25}\text{Si}_{0.50}$, (b) $\text{Si}_{0.25}\text{Ge}_{0.25}\text{Sn}_{0.50}$, (c) $\text{Sn}_{0.25}\text{Si}_{0.25}\text{Ge}_{0.50}$ and Shift in energy as a function of strain for (d) $\text{Ge}_{0.25}\text{Sn}_{0.25}\text{Si}_{0.50}$, (e) $\text{Si}_{0.25}\text{Ge}_{0.25}\text{Sn}_{0.50}$, (f) $\text{Sn}_{0.25}\text{Si}_{0.25}\text{Ge}_{0.50}$ hybrid monolayer.

4.3.4 Density of States and Atom Projected Density of States

In order to understand the characteristics of atomic bonds, and contribution of each of the atomic orbitals to the molecular orbital, the total density of states and atom projected density of states of these novel hybrid monolayers have been calculated and analyzed. The total and atom projected density of states of $\text{Ge}_{0.25}\text{Sn}_{0.25}\text{Si}_{0.50}$, $\text{Si}_{0.25}\text{Ge}_{0.25}\text{Sn}_{0.50}$, and $\text{Sn}_{0.25}\text{Si}_{0.25}\text{Ge}_{0.50}$ are shown in Figure 4.4(a), (b), and (c) respectively. From Figure 4.4(a), it can be seen that the total density of states of $\text{Ge}_{0.25}\text{Sn}_{0.25}\text{Si}_{0.50}$ is similar to the contribution of the P orbitals of the Si atoms. So, the electronic properties of $\text{Ge}_{0.25}\text{Sn}_{0.25}\text{Si}_{0.50}$ monolayer is dominated by Si atoms which is widely present in the structure [130], [137]. In Figure

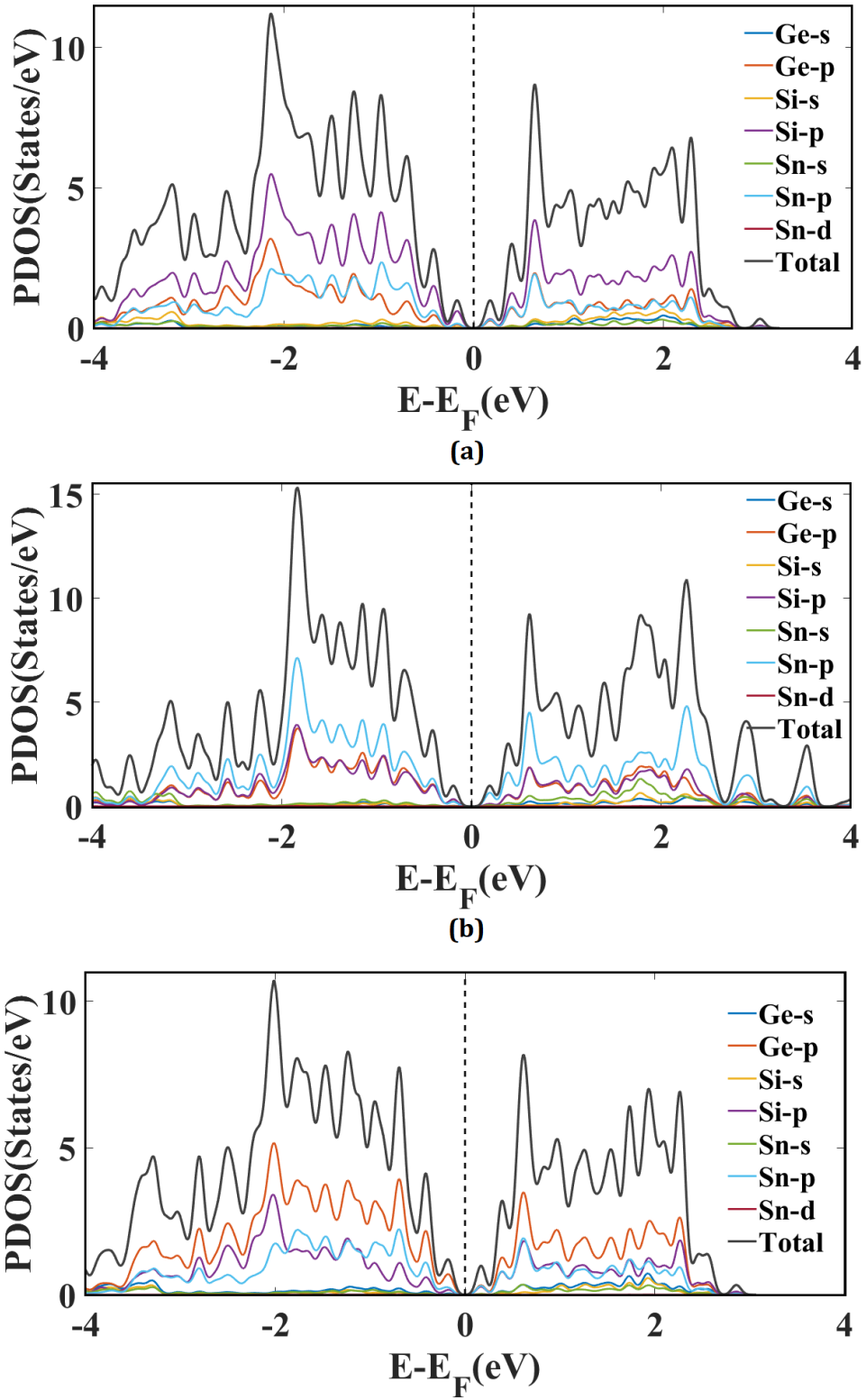


Figure 4.4: Atom projected Density of states as a function of energy for (a) $\text{Ge}_{0.25}\text{Sn}_{0.25}\text{Si}_{0.50}$, (b) $\text{Si}_{0.25}\text{Ge}_{0.25}\text{Sn}_{0.50}$, and (c) $\text{Sn}_{0.25}\text{Si}_{0.25}\text{Ge}_{0.50}$ hybrid monolayer.

4.4(a) the atom projected density of states also shows that the valence band states and the conduction band states of the $\text{Ge}_{0.25}\text{Sn}_{0.25}\text{Si}_{0.50}$ monolayer is dominated by the P orbitals of the Si, Ge, and Sn atoms with small contribution from the S orbitals, this result confirms the presence of the orbital hybridization among S and P orbitals [123] in this monolayer. Other two monolayers also depict the similar characteristics. As it can be observed from Figure 4.4(b), the total density states of the $\text{Si}_{0.25}\text{Ge}_{0.25}\text{Sn}_{0.50}$ monolayer is similar to the contribution of the P orbitals of Sn atoms indicating that the electronic properties of the $\text{Si}_{0.25}\text{Ge}_{0.25}\text{Sn}_{0.50}$ monolayer will be dictated by the Sn atoms, and the valence and the conduction bands of the total density of states are dominated by the P orbitals of the Sn, Si, and Ge atoms with small contribution from the S orbitals indicating the presence of orbital hybridization. Figure 4.4(c) shows the total and atom projected density of states of the $\text{Sn}_{0.25}\text{Si}_{0.25}\text{Ge}_{0.50}$ monolayer, where the line shape of the total density of states is similar to that of the P orbitals of the Ge atoms which tells that the electronic properties of $\text{Sn}_{0.25}\text{Si}_{0.25}\text{Ge}_{0.50}$ will be dominated by the Ge atoms. Figure 4.4(c) also indicates the presence of orbital hybridization among S and P orbitals of Si, Ge, and Sn atoms as the valence and conduction bands are dominated by the P orbitals with small contribution from S orbitals of Ge, Si, and Sn atoms. From the analysis of the density of states, it is evident that the electronic properties of the hybrid monolayers will be similar to the dominant atom present and there is sp^2 - sp^3 like orbital hybridization which is also consistent with the buckled structures of the monolayers.

4.3.5 Differential Charge Density

In order to understand the electronic and structural properties more deeply, the differential charge density (DCD) of the hybrid monolayers of Si, Ge, and Sn have been studied, which basically represents the rearrangement of the charge due to the formation of monolayers from the isolated atoms [135, [145], [146]. DCD is defined as

$$\Delta\rho = \rho_{\text{Hybrid Monolayer}} - \rho_{\text{Si}} - \rho_{\text{Ge}} - \rho_{\text{Sn}} \quad (4.2)$$

Where $\Delta\rho$ is the differential charge density, $\rho_{\text{Hybrid Monolayer}}$ is charge density of the hybrid monolayers of Si, Ge, Sn, and ρ_{Si} , ρ_{Ge} and ρ_{Sn} are charge densities of isolated Si, Ge, and Sn atoms respectively.

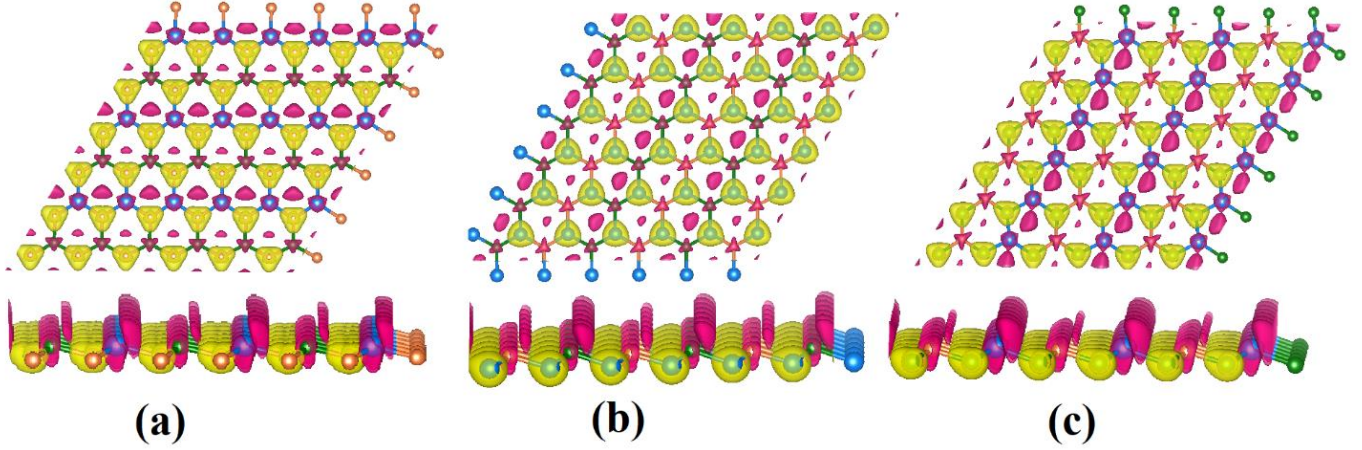


Figure 4.5: Top (top) and side (bottom) view of Differential Charge Density of (a) $\text{Ge}_{0.25}\text{Sn}_{0.25}\text{Si}_{0.50}$, (b) $\text{Si}_{0.25}\text{Ge}_{0.25}\text{Sn}_{0.50}$, and (c) $\text{Sn}_{0.25}\text{Si}_{0.25}\text{Ge}_{0.50}$ hybrid monolayer.

Figure 4.5 shows DCD for different hybrid monolayers, where the yellow and magenta colored isosurfaces depict electron accumulation and electron depletion regions respectively. Figure 4.5(a) shows the top and side views of DCD of $\text{Ge}_{0.25}\text{Sn}_{0.25}\text{Si}_{0.50}$, which illustrate electron accumulation region near Si atoms and the electrons are depleted near Ge and Sn atoms. Similarly, Figure 4.5(b) shows the top and side views of the DCD of $\text{Si}_{0.25}\text{Ge}_{0.25}\text{Sn}_{0.50}$ hybrid monolayer, from the figure it is clear that electron accumulation region around the Sn atoms and electron depletion region near Si and Ge atoms. Similar result is obtained from Figure 4.5(c) which shows an electron depletion region near Sn and Si atoms whereas electrons are accumulated around the Ge atoms of the $\text{Sn}_{0.25}\text{Si}_{0.25}\text{Ge}_{0.50}$ hybrid monolayer. Large bond lengths between Si, Ge, and Sn atoms are accountable for the redistribution of the charge carriers which further creates an internal electric field in the planar structure of the monolayers. This interaction among the atoms is responsible for breaking the inversion symmetry thus opening an energy bandgap at the K point of the BZ [145], [147], [148]. When spin-orbit coupling in the atoms is considered, these interactions strengthen further, which can be understood from the wider energy bandgap at the K point of the band structure at the presence of the spin orbital interaction. The charge density of the iso-surfaces of electron accumulation and electron depletion regions in the figure are $0.04 \text{ electron}/\text{\AA}^3$ and $0.001 \text{ electron}/\text{\AA}^3$ respectively which indicate very small charge rearrangement in the intermediate region of the three hybrid monolayers. As a result of which linear energy-momentum relation is quite well preserved in these structures [135] which ensures the presence of the relativistic massless Dirac fermion as high mobility charge carrier.

4.4 Optical Properties

Optical properties of semiconducting 2D monolayer materials are seeking more attention of the researchers due to their potential applications in optical processes, e.g. absorbing sheets, anti-reflection coating, biosensors, etc. [149]-[151]. In this study, optical properties such as dielectric function, electron loss function, absorption coefficient, reflectivity, refractive index, optical conductivity etc. for parallel and perpendicular polarization of incident light with respect to the plane of the monolayer from 0 eV to 25 eV energy of the incident light have been calculated. Although in this study many-body interactions among excited electrons and holes are not considered for the optical calculations they will not create large errors. Consideration of such interactions will not cause wide change in frequencies for these monolayers, they are expected to insignificantly change the amplitude of the optical responses. For example, Matthes *et al* [152]. have reported the optical properties of monolayer graphene, silicene, germanene, and stanene using first principles calculations with and without considering excitonic effects, and excitonic effects have very negligible effects on the optical response of those monolayers.

4.4.1 Real part of Complex Dielectric Function and Electron Energy Loss Function

The complex dielectric function is closely related to the response of the material in the presence of electromagnetic wave: the real part is related to the portion of stored electromagnetic energy in a dielectric medium and the imaginary part is related to the energy dissipation of the electromagnetic wave [149]. The real part of the dielectric function, $\text{Re}[\epsilon(\omega)]$ of the hybrid monolayers are shown in Figure 4.6(a) and (b) for perpendicularly and parallelly polarized incident light, respectively. The static dielectric constant, i.e. the value of $\text{Re}[\epsilon(\omega)]$ at $\hbar\omega=0$ eV indicates whether the material is semiconducting or metallic; very high value of static dielectric constant is related to the metallic property of the material [153]. From Figures 4.6(a) and (b) it is observed that the static dielectric constant of $\text{Ge}_{0.25}\text{Sn}_{0.25}\text{Si}_{0.50}$, $\text{Si}_{0.25}\text{Ge}_{0.25}\text{Sn}_{0.5}$, and $\text{Sn}_{0.25}\text{Si}_{0.25}\text{Ge}_{0.50}$ monolayers for perpendicularly polarized incident light are 1.448, 1.501, and 1.49, respectively and for parallelly polarized incident light are 3.289, 3.496, and 3.502, respectively. These small values of static dielectric constants reflect the semiconducting

property of the hybrid monolayers which is also confirmed by the energy band structures of the nanostructure as they have been discussed in section 4.3.1. However, the static dielectric constant for parallelly polarized light is more than twice than that for perpendicularly polarized light. The minimum value of the $\text{Re}[\epsilon(\omega)]$ is related to the collective response of the electrons inside the materials [149]. From Figure 4.6(a) it is seen that $\text{Ge}_{0.25}\text{Sn}_{0.25}\text{Si}_{0.50}$ and $\text{Sn}_{0.25}\text{Si}_{0.25}\text{Ge}_{0.50}$ monolayers show a minimum value of $\text{Re}[\epsilon(\omega)]$ around 8eV. Moreover, the negative value of $\text{Re}[\epsilon(\omega)]$ implies the forbidden region of light transmission, as in this energy range, light cannot propagate through the material [151]. Narrow forbidden region in the UV range of the electromagnetic wave is apparent from the figures of dielectric function. From Figure 4.6(a) and (b), for parallelly polarized light the $\text{Ge}_{0.25}\text{Sn}_{0.25}\text{Si}_{0.50}$, $\text{Si}_{0.25}\text{Ge}_{0.25}\text{Sn}_{0.50}$, and $\text{Sn}_{0.25}\text{Si}_{0.25}\text{Ge}_{0.50}$ monolayers show forbidden interval from 4.005 eV to 5.066 eV, 3.804 eV to 4.706 eV and 3.969 eV to 4.876 eV respectively; for perpendicularly polarized light $\text{Si}_{0.25}\text{Ge}_{0.25}\text{Sn}_{0.50}$ monolayer shows a forbidden energy interval from 7.401 eV to 7.728 eV. When $\text{Re}[\epsilon(\omega)] = 0$ occurs and changes from negative to positive for an incident light energy, the collective oscillation of the charge carriers form standing waves leads to resonant oscillation, also known as plasmonic oscillation; and the frequency at which such oscillation occurs is called plasma frequency. Near the plasma frequency the electron energy loss (E_{loss}) function also shows a peak in energy indicating the maximum loss of electron energy passing through the material [150], [151]. The Eloss function shown in Figure 4.7(a) and (b), implies the amount of energy loss in the electrons propagating through the materials. For parallel polarization, the plasma frequency of the $\text{Ge}_{0.25}\text{Sn}_{0.25}\text{Si}_{0.50}$, $\text{Si}_{0.25}\text{Ge}_{0.25}\text{Sn}_{0.50}$, and $\text{Sn}_{0.25}\text{Si}_{0.25}\text{Ge}_{0.50}$ monolayers are 5.006 eV, 4.706 eV, and 4.876 eV, respectively and also in this case the peaks in the Eloss function for $\text{Ge}_{0.25}\text{Sn}_{0.25}\text{Si}_{0.50}$, $\text{Si}_{0.25}\text{Ge}_{0.25}\text{Sn}_{0.50}$, and $\text{Sn}_{0.25}\text{Si}_{0.25}\text{Ge}_{0.50}$ monolayers are found at 5.829 eV, 4.981 eV and 4.996 eV, respectively. For perpendicular polarization, the plasma frequency and the peaks in the Eloss function of $\text{Ge}_{0.25}\text{Sn}_{0.25}\text{Si}_{0.50}$, $\text{Si}_{0.25}\text{Ge}_{0.25}\text{Sn}_{0.50}$, and $\text{Sn}_{0.25}\text{Si}_{0.25}\text{Ge}_{0.50}$ monolayers are listed in the Table 4.3. Surface plasmon resonance in 2D materials can be utilized in various applications e.g., plasmonic switches [154], ultrasensitive biochemical sensors [155] etc. The plasma frequency can be modulated by controlling the composition of the hybrid materials and the polarization of the incident light. Although many factors may be responsible for the peaks in the Eloss function such as, phonon excitation, inter and intra-band transition, inner shell ionization, the results above demonstrate that surface plasmon oscillation plays an

important role in the maximum values of the Eloss function. These results are summarized in Table 4.3.

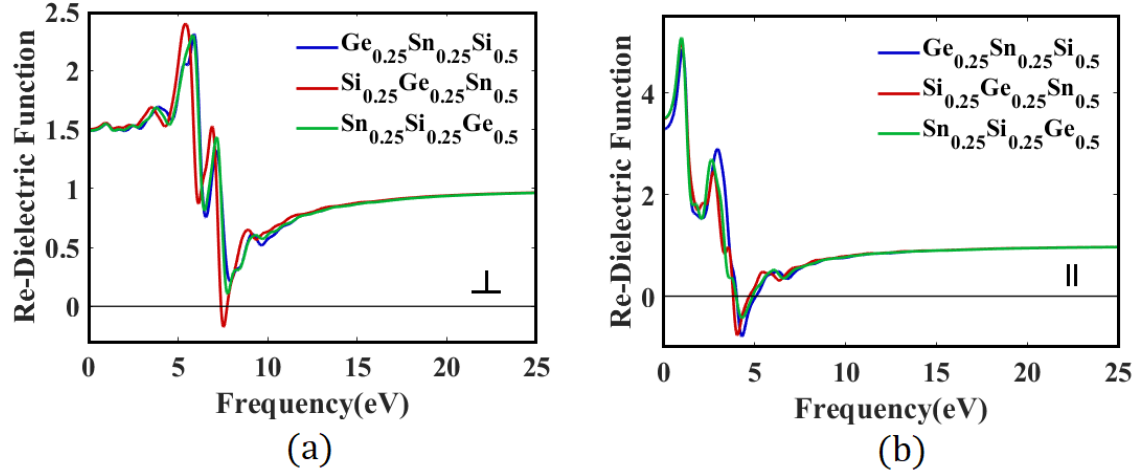


Figure 4.6: Real Part of Dielectric Function when Electromagnetic field is polarized in (a) 001(\perp) and (b) 100(\parallel) direction of Monolayer Hybrid of Si, Ge and Sn.

Table 4.3: Real part of dielectric function, peak in Eloss function, plasma frequency, forbidden region and in novel hybrid monolayers of Si, Ge and Sn

Structure	Static Dielectric Constant		Peak in Electron Loss Function (eV)		Plasma Frequency (eV)		Forbidden Region (eV)	
	$\epsilon(0)\perp$	$\epsilon(0)\parallel$	\perp	\parallel	\perp	\parallel	\perp	\parallel
$\text{Ge}_{0.25}\text{Sn}_{0.25}\text{Si}_{0.50}$	1.488	3.289	8.485	5.829	-	5.066	-	4.005 to 5.066
$\text{Si}_{0.25}\text{Ge}_{0.25}\text{Sn}_{0.50}$	1.501	3.496	7.924	4.981	7.728	4.706	7.401 to 7.728	3.804 to 4.706
$\text{Sn}_{0.25}\text{Si}_{0.25}\text{Ge}_{0.50}$	1.49	3.502	8.462	4.996	-	4.876	-	3.969 to 4.876

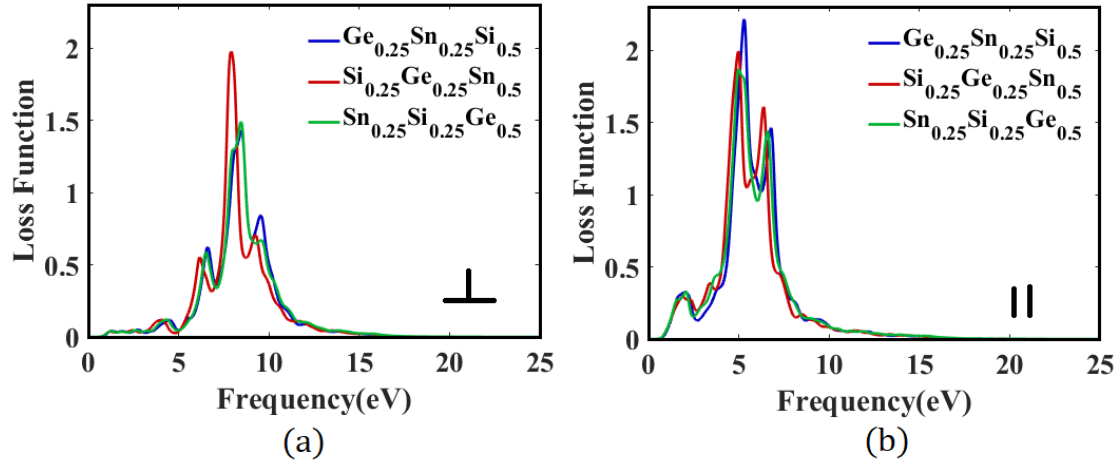


Figure 4.7: Electron Loss Function when Electromagnetic field is polarized in (e) 001(\perp) and (f) 100(\parallel) direction, of Monolayer Hybrid of Si, Ge and Sn.

4.4.2 Imaginary part of Complex Dielectric Function and Absorption Coefficient

Imaginary part of the dielectric function, $\text{Im}[\epsilon(\omega)]$ of the three hybrid monolayers are shown in Figure 4.8(a) and (b) for perpendicularly and parallelly polarized incident light, respectively. Imaginary part of the dielectric function relies on the inter-band and intra-band transition of electrons from occupied state to unoccupied state [156], and provides an indication of the energy bandgap within the nanostructures. As it can be seen from Figure 4.8(a) and (b), the $\text{Im}[\epsilon(\omega)]$ is zero up to around 0.5 eV of incident light energy, it rises immediately after 0.5 eV; this is known as fundamental absorption edge [157]. The value of this fundamental absorption edge can also be confirmed by observing the energy bandgap from the band structures of the hybrid monolayers. The hybrid monolayers demonstrate highly anisotropic response with respect to perpendicularly and parallelly polarized incident light from 0 eV to 10 eV and isotropic response for the incident light of above 10eV, which will be further demonstrated in the discussion of refractive index. The peaks of the imaginary part of the dielectric function, $\text{Im}[\epsilon(\omega)]$ is related to the inter-band and intra-band transition of electron from occupied state to unoccupied state, and this can

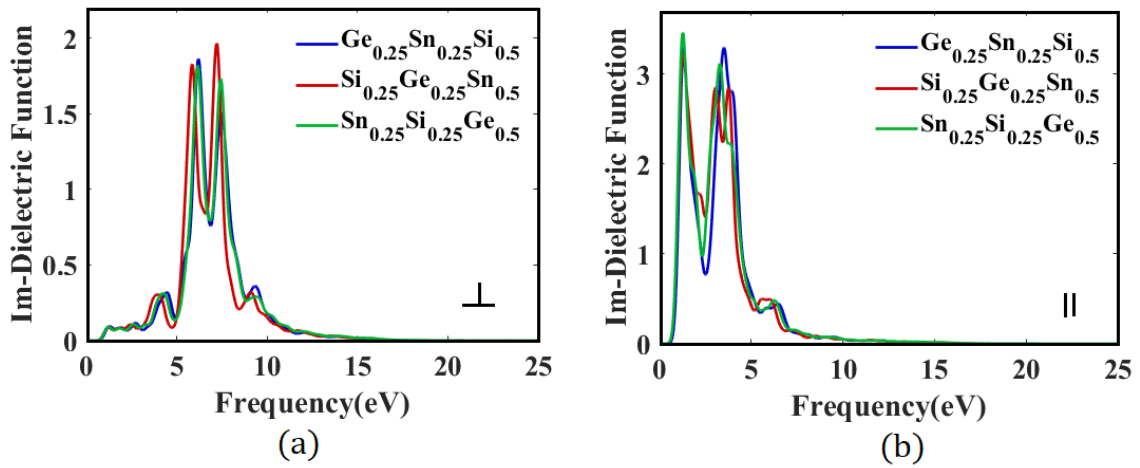


Figure 4.8: Imaginary part of Dielectric Function when Electromagnetic field is polarized in (a) 001(\perp) and (b) 100(\parallel) direction, of Monolayer Hybrid of Si, Ge and Sn.

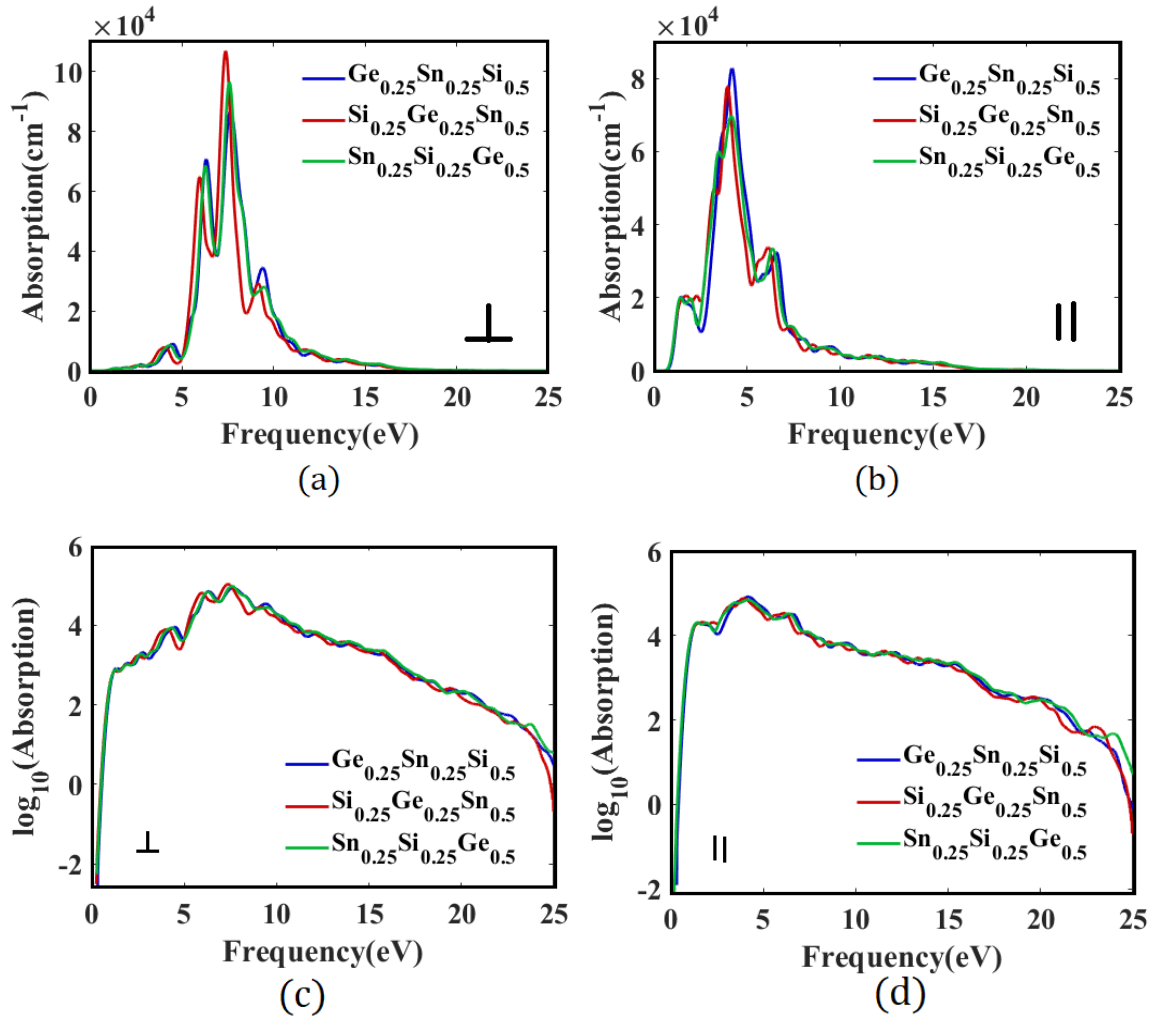


Figure 4.9: Absorption coefficient when Electromagnetic field is polarized in (a) 001(\perp) and (b) 100(\parallel) direction, Log of Absorption coefficient when Electromagnetic field is polarized in (c) 001(\perp) and (d) 100(\parallel) direction, of Monolayer Hybrid of Si, Ge and Sn.

also be confirmed by studying the absorption spectra of the hybrid monolayers [31]. The absorption spectra of the hybrid monolayers of Si, Ge and Sn as a function of energy for perpendicularly and parallelly polarized incident light are shown in Figure 4.9(a) and (b), respectively. The positions of the peaks in the absorption spectra are consistent with the positions of the peaks in the $\text{Im}[\epsilon(\omega)]$. These results are summarized in Table 4.4. As listed in Table 4.3, the forbidden energy interval of the monolayer $\text{Ge}_{0.25}\text{Sn}_{0.25}\text{Si}_{0.50}$ for parallelly polarized light is 4.005 eV to 5.006 eV, and also Figure 4.9(a) illustrates a sharp decline in absorption in this energy interval. The absorption spectra for other hybrid monolayers also show similar characteristics. For both perpendicular and parallel polarization of the incident light, absorption sharply increases around 0.12 meV, 0.23 meV, 0.11 meV for $\text{Ge}_{0.25}\text{Sn}_{0.25}\text{Si}_{0.50}$, $\text{Si}_{0.25}\text{Ge}_{0.25}\text{Sn}_{0.50}$, and $\text{Sn}_{0.25}\text{Si}_{0.25}\text{Ge}_{0.50}$ monolayers respectively which are close to the energy bandgaps measured previously. The peaks of the absorption spectra are due to direct and indirect inter-band and intra-band transitions, as a result several peaks are evident in the spectra. From the absorption spectra it is clear that, the hybrid monolayers exhibit significantly higher absorption coefficient from the near infrared (1.58 eV) region to extreme UV region (16eV) and lower absorption coefficient in the mid and far infrared, deep into the extreme UV region. Considering the above results, the hybrid monolayers are suitable as ultra-broadband optical absorber ranging from visible to extreme UV region.

Table 4.4: Imaginary part of dielectric function, absorption coefficient and Static Refractive index of Novel Hybrid monolayers of Si, Ge and Sn

Structure	Positions of peaks in Imaginary part of dielectric function (eV)		Positions of peaks in absorption spectra (eV)		Static Refractive Index	
	\perp	\parallel	\perp	\parallel	$\eta(0)\perp$	$\eta(0)\parallel$
$\text{Ge}_{0.25}\text{Sn}_{0.25}\text{Si}_{0.50}$	4.451, 6.193, 7.476, 9.363	1.307, 3.507	4.49, 6.311, 7.647, 9.402	1.477, 4.189	1.22	1.814
$\text{Si}_{0.25}\text{Ge}_{0.25}\text{Sn}_{0.50}$	3.961, 5.844, 7.218, 9.102	1.279, 3.764	4.065, 5.949, 7.388, 9.154	1.737, 3.948	1.225	1.87
$\text{Sn}_{0.25}\text{Si}_{0.25}\text{Ge}_{0.50}$	4.263, 6.156, 7.436, 9.435	1.263, 3.29	4.316, 6.276, 7.582, 9.475	1.423, 4.156	1.22	1.871

4.4.3 Complex Refractive Index

The real and imaginary part of the complex refractive index represent the refractive index and the extinction coefficient respectively, which are important for characterizing the

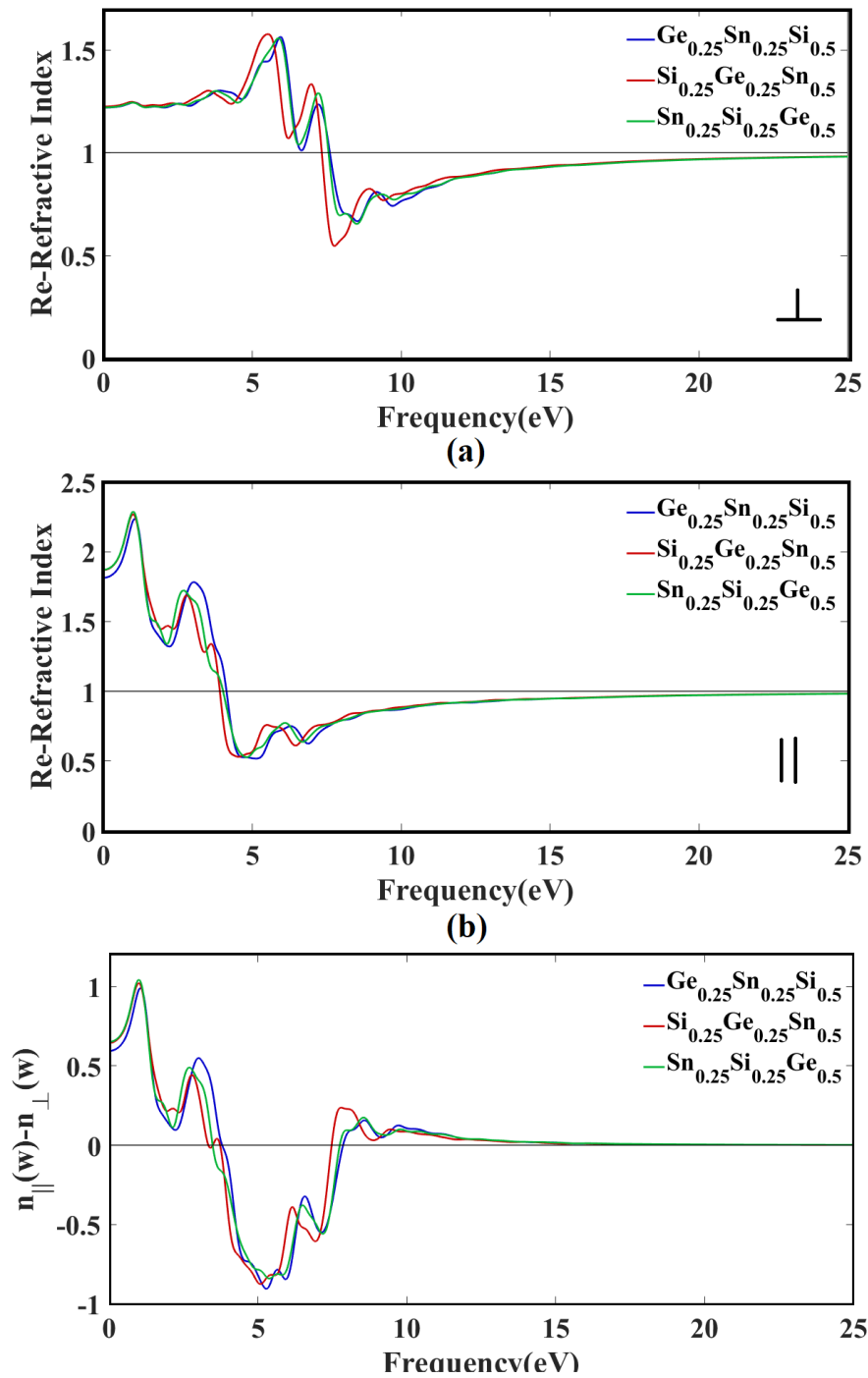


Figure 4.10: Real part of Refractive index when Electromagnetic field is polarized in (a) 001(\perp) and (b) 100(\parallel) direction, (c) Birefringence characteristics of Monolayer Hybrid of Si, Ge and Sn.

optical properties of a material. Figure 4.10(a) and (b) show the real part of the refractive index as a function of energy of the incident light for perpendicularly and parallelly polarized light, respectively for the novel hybrid monolayers of Si, Ge, and Sn. The line shapes of the real refractive index for each of the monolayers are similar, they follow similar trend of change. The values of the static refractive index are greater for parallelly polarized incident light compared to that of the perpendicularly polarized incident light since the parallelly polarized light interacts within a plane which has higher density of atoms [149], the obtained results are summarized in Table 4.4. The real refractive index spectra demonstrate anisotropic response for parallelly and perpendicularly polarized light in the range from 0 to 10 eV. As the real refractive index is different for different

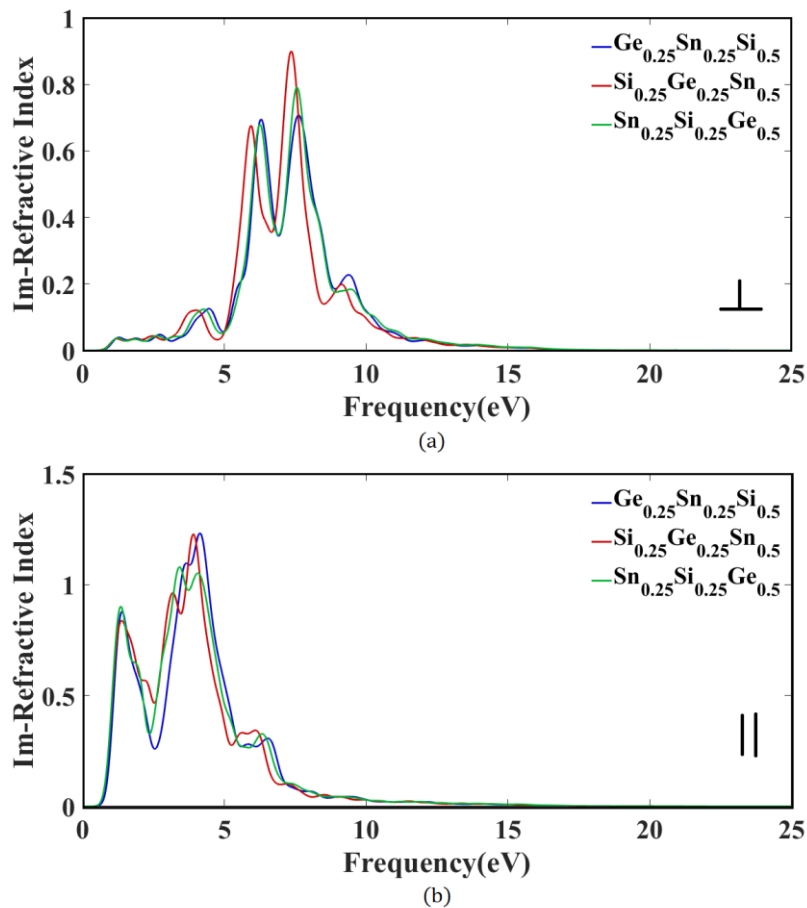


Figure 4.11: Imaginary part of Refractive index when Electromagnetic field is polarized in (a) 001(⊥) and (b) 100(∥) direction, of Monolayer Hybrid of Si, Ge and Sn.

polarization of the incident light, the velocity of the parallelly and perpendicularly polarized light will also be different, which indicates each of the hybrid monolayers will show

birefringence characteristics. The birefringence characteristics, calculated from the difference between the real part of the refractive indices for the parallelly and perpendicularly polarized incident light [149], shown in Figure 4.10(c) as a function of the energy of the incident light. These results are also consistent from the anisotropic response in the imaginary part of the dielectric function. These birefringence properties of two-dimensional materials are used to create a variety of optical applications, including optical waveplates [158] and polarization-controlled spontaneous emission [159]. Moreover, as the energy of the incident light increases, the value of the refractive index tends to reach the unity, which indicates vacuum like response of the hybrid monolayers for UV lights [153].

The imaginary part of the refractive index, extinction coefficient as a function of the energy of the incident light are shown in Figure 4.11(a) and (b) for perpendicularly and parallelly polarized light respectively, for the hybrid monolayers. The extinction coefficient is related to the dissipation of the optical energy inside the material [160], hence it is closely related to the absorption spectra and imaginary part of the dielectric function. The response shown in Figure 4.11(a), 4.11(b) follow similar trend as the plot of Figure 4.8(a), (b) and 4.9(a), (b). As the energy of the incident light increases beyond 10 eV, the extinction coefficient and absorption coefficient tend to be zero; indicating no energy absorption in deep UV region.

4.4.4 Reflectivity

Reflectivity of the novel hybrid monolayers of Si, Ge and Sn as a function of energy of the incident light is shown in Figure 4.12(a) and (b) for perpendicularly and parallelly polarized incident light, respectively. The line shape of the reflectivity of the three monolayers are almost similar. In the infrared, visible light, deep in to extreme UV ($>10\text{eV}$) spectra the value of the reflectivity is very negligible.

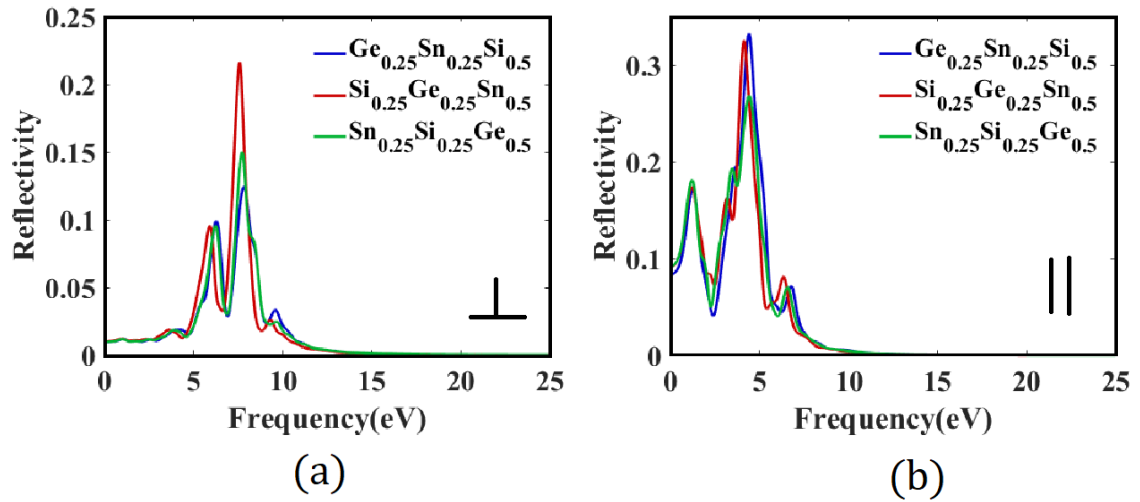


Figure 4.12: Reflectivity when Electromagnetic field is polarized in (a) 001(\perp) and (b) 100(\parallel) direction, of Monolayer Hybrid of Si, Ge and Sn.

The value of reflectivity is dominant in the UV region (5 eV-10 eV). Table 4.5 summarizes the value of maximum reflectivity and the frequency at which maximum reflection occurs. Similar anisotropic response is also visible for parallelly and perpendicularly polarized incident light from 0 eV to 10 eV. As it can be seen from these results, the reflectivity and absorption spectra are very insignificant in infrared, visible light (0 eV to 5 eV) and deep in to the extreme UV region (> 10 eV). So, the hybrid monolayers act as transparent medium of light for infrared, visible and extreme UV lights [161].

4.4.5 Optical Conductivity

Optical conductivity relates the density of current in a material with respect to the applied electric field as a function of frequency. Complex optical conductivity is closely related to the complex dielectric function. The real part of the complex optical conductivity of novel hybrid monolayers of Si, Ge, and Sn for perpendicularly and parallelly polarized incident light are shown in Figure 4.13(a) and 4.13(b), respectively. The real part of the optical conductivity is related to imaginary part of the dielectric function, extinction coefficient and absorption spectra etc. [149]. As it can be seen from Figure 4.13(a) and 4.13(b), the threshold value of the real part of the optical conductivity is consistent with the fundamental absorption edge (0.5 eV), which is closely related to the optical bandgap of the material. The line shape and position of the peaks are also consistent with the absorption spectra and the imaginary part of the dielectric function. The imaginary part of the conductivity for

perpendicularly and parallelly polarized light are shown in Figure 4.14(a) and 4.14(b) respectively for the hybrid monolayers. The imaginary part of complex conductivity is related to the real part of the dielectric function. As we can see in Figure 4.14(a) and 4.14(b), the zero crossing are consistent with the values of plasma frequency derived from the real part of the dielectric function. Table 4.5 summarizes these results. The results of the optical properties computed for our novel hybrid monolayers of Si, Ge and Sn are consistent with the reported values of optical properties of silicene, germanene and stanene [149], [162].

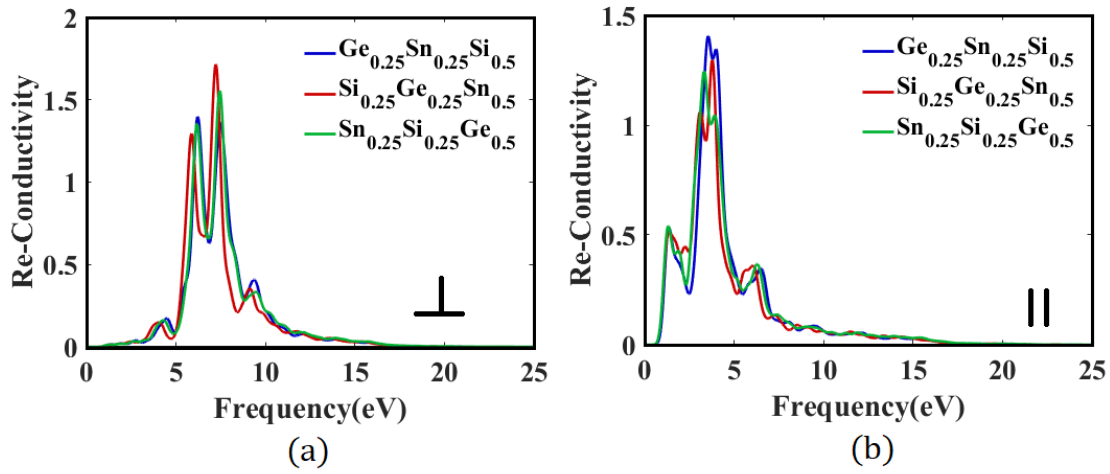


Figure 4.13: Real part of Optical Conductivity when Electromagnetic field is polarized in (a) 001(\perp) and (b) 100(\parallel) direction of Monolayer Hybrid of Si, Ge and Sn.

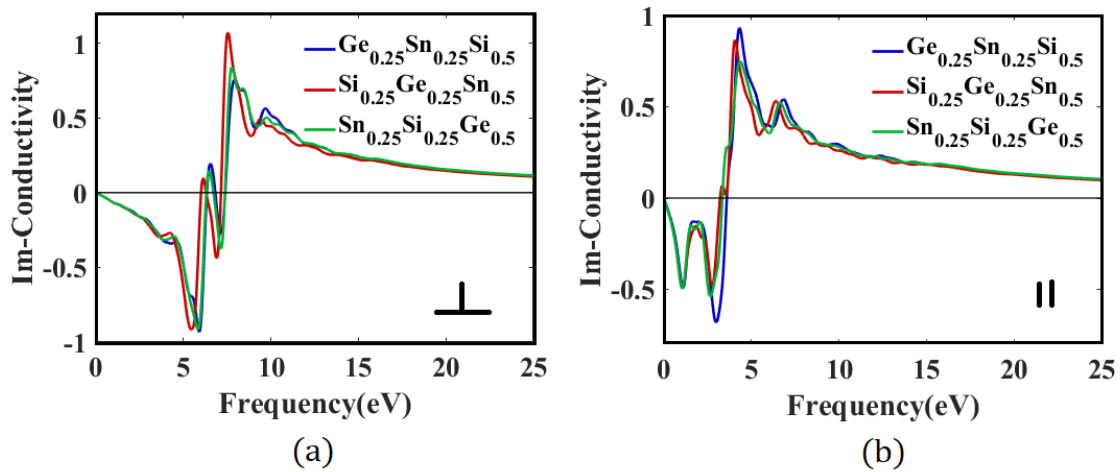


Figure 4.14: Imaginary part of Optical Conductivity when Electromagnetic field is polarized in (a) 001(\perp) and (b) 100(\parallel) direction, of Monolayer Hybrid of Si, Ge and Sn.

Table 4.5: Value of maximum reflectivity and frequency at which maximum reflection occurs, Positions of peaks in Real part of complex conductivity and Zero crossings in Imaginary part of complex conductivity in Novel Hybrid monolayers of Si, Ge and Sn

Structure	Value of Maximum Reflectivity		Frequency at which Maximum Reflectivity occurs (eV)		Positions of peaks in Real part of complex conductivity (eV)		Zero crossings in Imaginary part of complex conductivity (eV)	
	\perp	\parallel	\perp	\parallel	\perp	\parallel	\perp	\parallel
$\text{Ge}_{0.25}\text{Sn}_{0.25}\text{Si}_{0.50}$	0.1244	0.3323	7.817	4.385	4.47, 6.206, 7.49, 9.363	1.359, 3.534	7.398	3.6
$\text{Si}_{0.25}\text{Ge}_{0.25}\text{Sn}_{0.50}$	0.2163	0.2682	7.584	4.409	4.052, 5.871, 7.218, 9.115	1.37, 3.791	7.153	3.215
$\text{Sn}_{0.25}\text{Si}_{0.25}\text{Ge}_{0.50}$	0.15	0.3255	7.716	4.118	4.47, 6.206, 7.49, 9.363	1.359, 3.534	7.382	3.343

4.5 Electron Transport Properties and Sensing Applications

To investigate quantum transport phenomena of the proposed hybrid monolayers, in this study, transport devices have been modeled using armchair nanoribbon (ANR) of the hybrid monolayers of Si, Ge and Sn. In experimentally fabricated transistor or sensing devices which include 2D materials as channel or sensing materials, these monolayers are considered as nanoribbons. So, to understand the electron transport properties of designed novel hybrid monolayers of Si, Ge, and Sn atoms, we have considered armchair nanoribbons as our transport device. The edge of the ANRs are passivated with hydrogen atoms, the length and the width of the nanoribbons are 42 Å and 13 Å, respectively. There are two electrodes composed of hybrid monolayers on each side, and a scattering region resides at the center. Singh *et al.* [163] modeled similar transport devices to investigate the electron transport properties of silicene. The electrodes are considered as ideal contacts for transport calculation. The top and side views of the relaxed structures of the hydrogen (H) passivated armchair nanoribbons of $\text{Ge}_{0.25}\text{Sn}_{0.25}\text{Si}_{0.50}$, $\text{Si}_{0.25}\text{Ge}_{0.25}\text{Sn}_{0.50}$, and $\text{Sn}_{0.25}\text{Si}_{0.25}\text{Ge}_{0.50}$ monolayers are shown in Figure 4.15(a), (c), and (e), respectively.

4.5.1 NH₃ Sensing

In order to sense the presence of NH₃ using electron transport properties, three NH₃ molecules are adsorbed on top of the nanoribbons. The absorption bond length of the relaxed structure between NH₃ molecule and Ge_{0.25}Sn_{0.25}Si_{0.50}, Si_{0.25}Ge_{0.25}Sn_{0.50}, and Sn_{0.25}Si_{0.25}Ge_{0.50} nanoribbons are 2.194 Å, 2.614 Å, and 2.413 Å respectively.

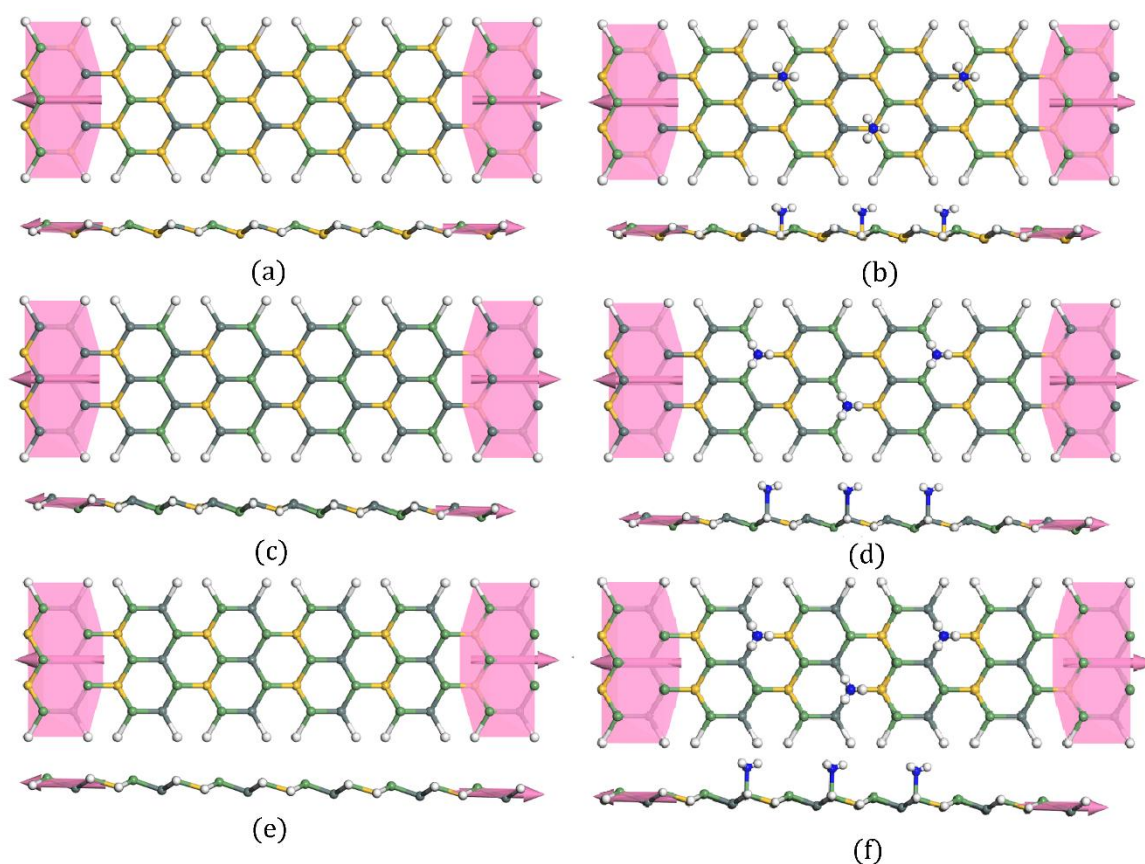


Figure 4.15: Top and side views of the Ge_{0.25}Sn_{0.25}Si_{0.50} (a) pristine (b) with NH₃ molecule and; top and side views of the Si_{0.25}Ge_{0.25}Sn_{0.50} (c) pristine (d) with NH₃ molecule; top and side views of the Sn_{0.25}Si_{0.25}Ge_{0.50} ANR electron transport device (e) pristine (f) with NH₃ molecule.

The top and side views of the relaxed structures of the H passivated armchair nanoribbons of Ge_{0.25}Sn_{0.25}Si_{0.50}, Si_{0.25}Ge_{0.25}Sn_{0.50}, and Sn_{0.25}Si_{0.25}Ge_{0.50} monolayers with NH₃ molecules are shown in Figure 4.15(b), (d) and (f), respectively and the computed differential charge density of the Ge_{0.25}Sn_{0.25}Si_{0.50}, Si_{0.25}Ge_{0.25}Sn_{0.50} and Sn_{0.25}Si_{0.25}Ge_{0.50} armchair nanoribbons in the presence of NH₃ molecules are shown in Figure 4.16(a), (b)

and 4.16(c), respectively. As it can be seen from these figures, due to adsorption of NH_3 molecules there is a redistribution of charge density in the nanoribbons. The blue regions depict electron accumulation and the yellow regions represent electron depletion regions. Due to NH_3 adsorption, there is electron accumulation near the nitrogen atoms and electron depletion regions near the hydrogen atoms and the nanoribbons. This charge redistribution is responsible for the difference in electron transport properties of the nanoribbons in the presence of NH_3 molecules.

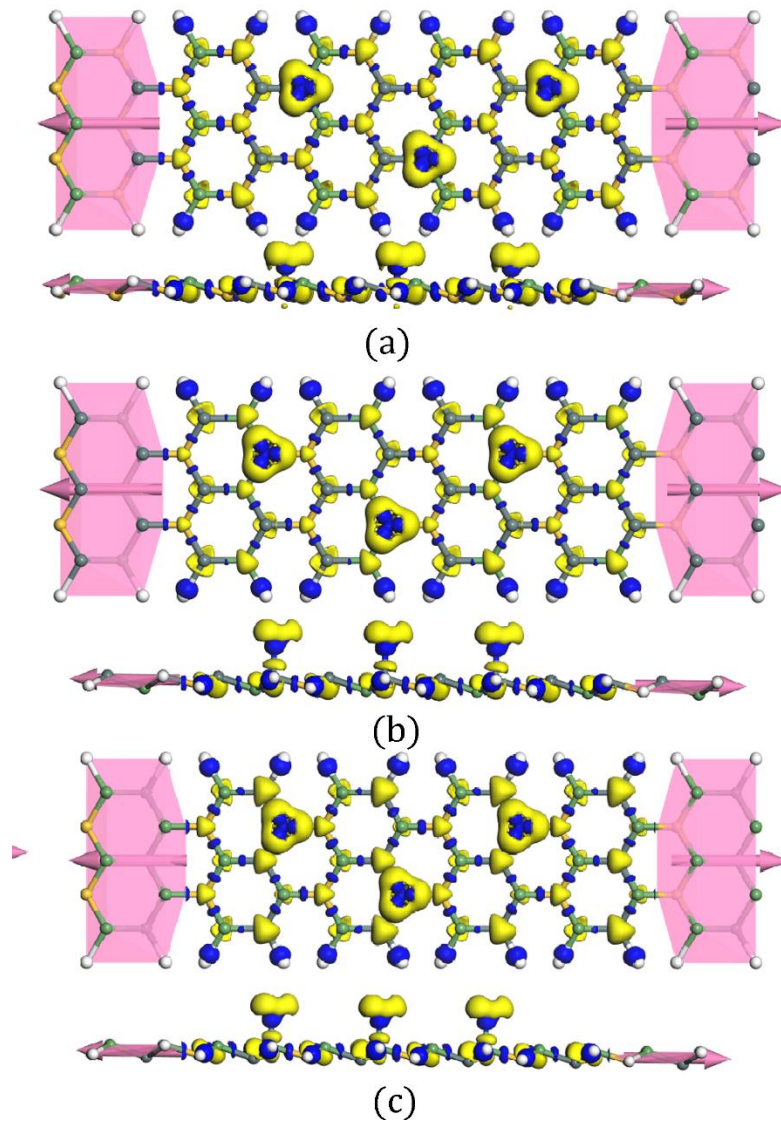


Figure 4.16: Top and side views of the Differential Charge Density in the presence of NH_3 molecule of (a) $\text{Ge}_{0.25}\text{Sn}_{0.25}\text{Si}_{0.50}$ (b) $\text{Si}_{0.25}\text{Ge}_{0.25}\text{Sn}_{0.50}$, (c) $\text{Sn}_{0.25}\text{Si}_{0.25}\text{Ge}_{0.50}$ ANR electron transport device.

To study the electron transport characteristics of the nanoribbons with and without NH_3 molecules a bias voltage from 0 V to 1 V is applied and the resulting current-voltage (I-V) characteristics of the $\text{Ge}_{0.25}\text{Sn}_{0.25}\text{Si}_{0.50}$, $\text{Si}_{0.25}\text{Ge}_{0.25}\text{Sn}_{0.50}$ and $\text{Sn}_{0.25}\text{Si}_{0.25}\text{Ge}_{0.50}$ armchair nanoribbons with and without NH_3 molecules are calculated and shown in Figure 4.17(a), (b) and (c), respectively. From the I-V characteristics, it can be understood that the applied voltage must be greater than a threshold voltage for the current to increase.

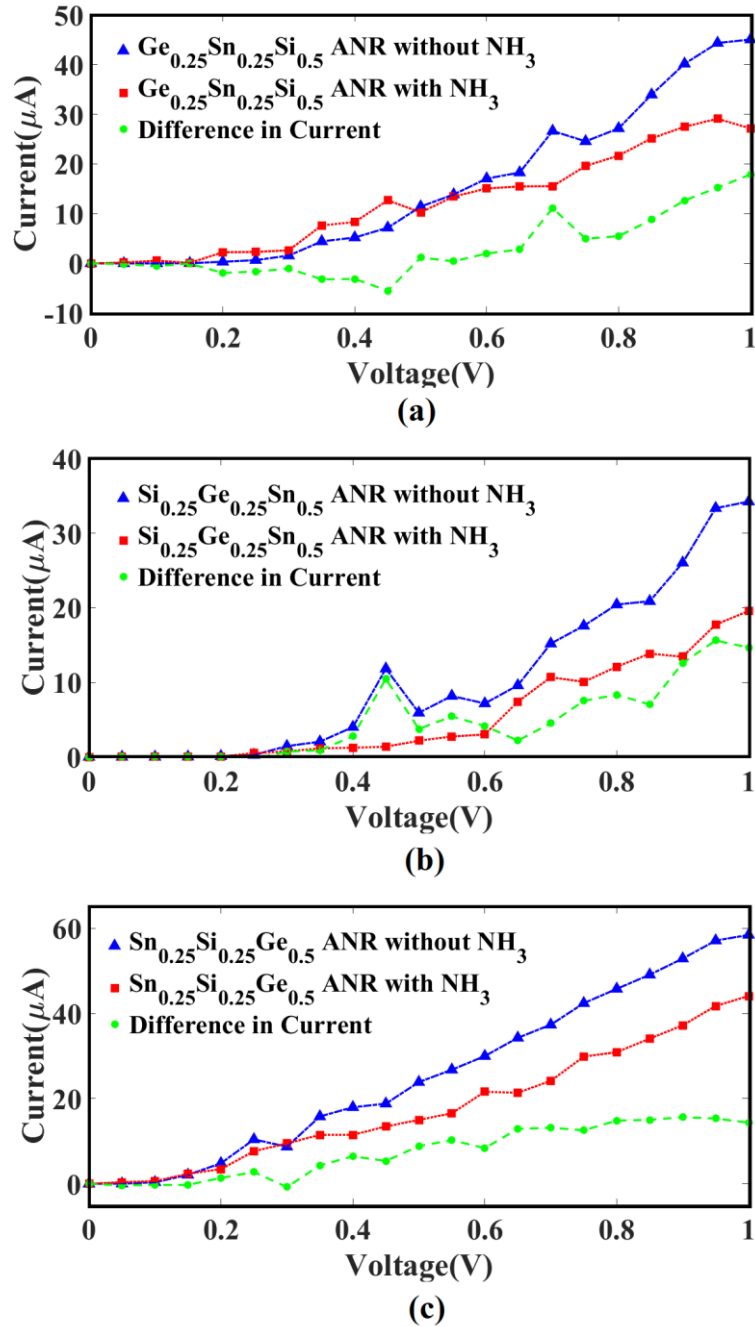
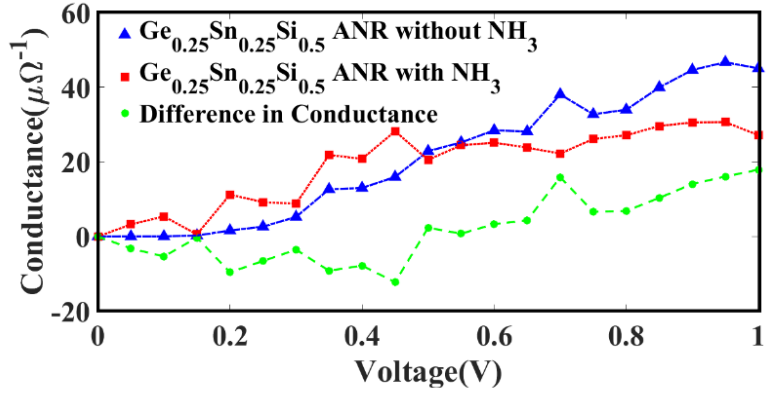
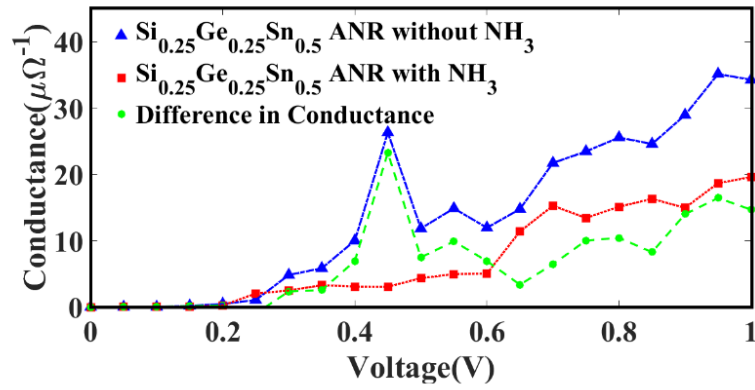


Figure 4.17: I-V characteristics of (a) $\text{Ge}_{0.25}\text{Sn}_{0.25}\text{Si}_{0.50}$, (b) $\text{Si}_{0.25}\text{Ge}_{0.25}\text{Sn}_{0.50}$, (c) $\text{Sn}_{0.25}\text{Si}_{0.25}\text{Ge}_{0.50}$ ANR

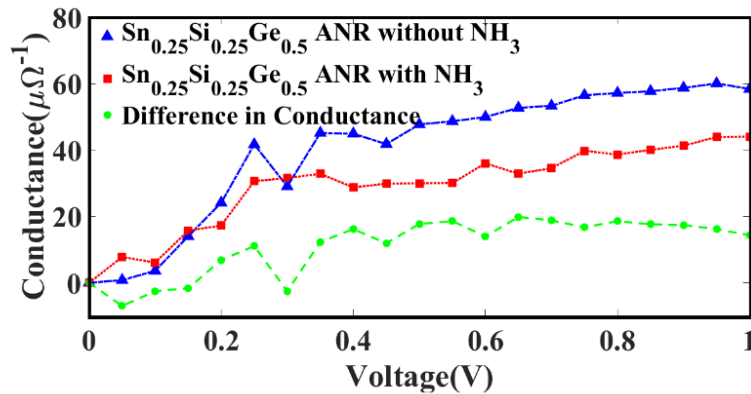
The threshold voltage of $\text{Ge}_{0.25}\text{Sn}_{0.25}\text{Si}_{0.50}$, $\text{Si}_{0.25}\text{Ge}_{0.25}\text{Sn}_{0.50}$ and $\text{Sn}_{0.25}\text{Si}_{0.25}\text{Ge}_{0.50}$ monolayers are around 0.15 V, 0.25 V, and 0.1 V, calculated from Figure 4.17(a), (b) and (c), respectively. These results further confirm the presence of energy bandgap at the energy band structure as calculated in the electronic properties and the semiconducting characteristics of nanoribbons. Similar results are observed in other studies [163], [164].



(a)



(b)



(c)

Figure 4.18: Conductance plot of (a) $\text{Ge}_{0.25}\text{Sn}_{0.25}\text{Si}_{0.50}$, (b) $\text{Si}_{0.25}\text{Ge}_{0.25}\text{Sn}_{0.50}$, (c) $\text{Sn}_{0.25}\text{Si}_{0.25}\text{Ge}_{0.50}$

As the bias voltage increases beyond the threshold voltage the current increases significantly, which confirms the high mobility of the proposed monolayers. With the presence of NH_3 molecules the value of current in $\text{Ge}_{0.25}\text{Sn}_{0.25}\text{Si}_{0.50}$ armchair nanoribbon from 0 V to 0.5 V is higher than pristine nanoribbon while beyond 0.5 V bias voltage the current is lower than the pristine counterpart.

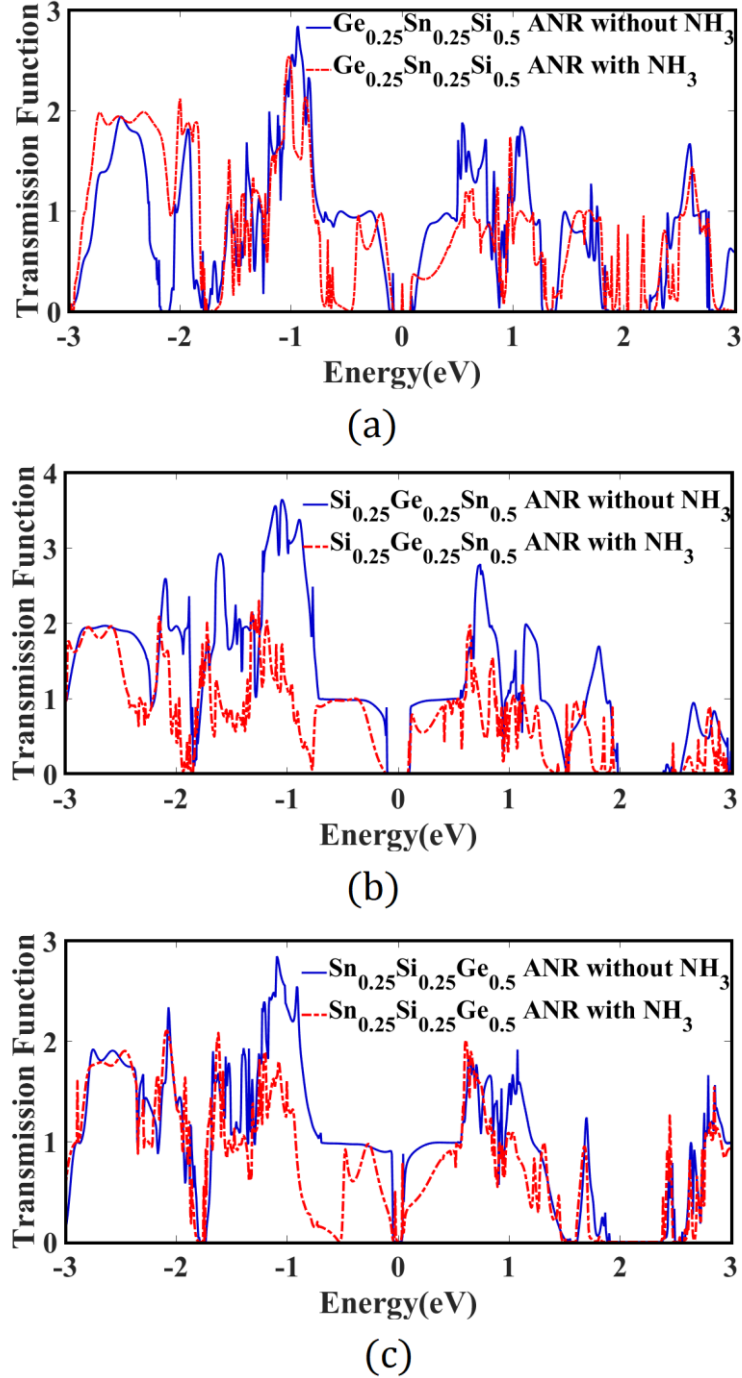


Figure 4.19: Transmission Function of (a) $\text{Ge}_{0.25}\text{Sn}_{0.25}\text{Si}_{0.50}$, (b) $\text{Si}_{0.25}\text{Ge}_{0.25}\text{Sn}_{0.50}$, (c) $\text{Sn}_{0.25}\text{Si}_{0.25}\text{Ge}_{0.50}$ electron transport device pristine (blue) and with NH_3 molecules (red).

Furthermore, for $\text{Si}_{0.25}\text{Ge}_{0.25}\text{Sn}_{0.50}$ and $\text{Sn}_{0.25}\text{Si}_{0.25}\text{Ge}_{0.50}$ armchair nanoribbons the value of current is lower in the presence of NH_3 molecules as compared to the pristine nanoribbons. The conductance as a function of voltage for $\text{Ge}_{0.25}\text{Sn}_{0.25}\text{Si}_{0.50}$, $\text{Si}_{0.25}\text{Ge}_{0.25}\text{Sn}_{0.50}$ and $\text{Sn}_{0.25}\text{Si}_{0.25}\text{Ge}_{0.50}$ armchair nanoribbons as shown in Figure 4.18(a), (b), (c) respectively. The change in the value of current or conductance can be utilized to indicate the presence of NH_3 molecules. The difference in the value of currents can be understood by studying the transmission function of the hybrid monolayers [163] with and without NH_3 molecules.

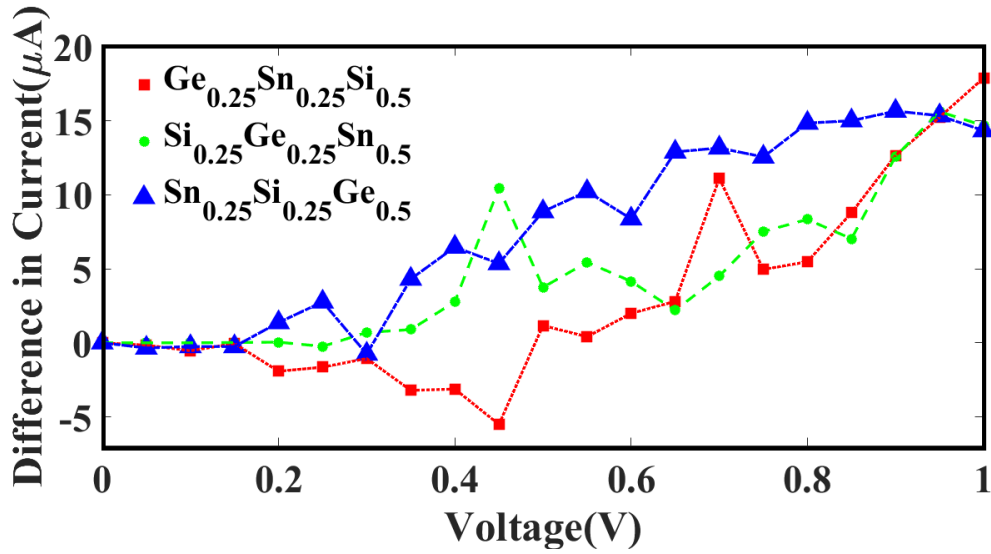


Figure 4.20: ΔI -V characteristics of (a) $\text{Ge}_{0.25}\text{Sn}_{0.25}\text{Si}_{0.50}$, (b) $\text{Si}_{0.25}\text{Ge}_{0.25}\text{Sn}_{0.50}$, (c) $\text{Sn}_{0.25}\text{Si}_{0.25}\text{Ge}_{0.50}$ ANR in the presence of NH_3 molecules.

Figure 4.19(a), (b), and (c) show the transmission function, the product of the number of sub-bands available in a particular energy state and the probability of transmission of $\text{Ge}_{0.25}\text{Sn}_{0.25}\text{Si}_{0.50}$, $\text{Si}_{0.25}\text{Ge}_{0.25}\text{Sn}_{0.50}$ and $\text{Sn}_{0.25}\text{Si}_{0.25}\text{Ge}_{0.50}$ armchair nanoribbons, respectively. The value of transmission function in the presence of the NH_3 molecules reduces significantly, and as a result the value of current in the presence of NH_3 molecules is also low compared to pristine nanoribbons. However, the transport characteristics of the armchair nanoribbons represent a nonlinear decreasing trend in conductance at some bias voltages, otherwise increases almost linearly [165]. Change in current of the hybrid nanoribbons in the presence of NH_3 molecules is shown in Figure 4.20; $\text{Sn}_{0.25}\text{Si}_{0.25}\text{Ge}_{0.50}$ armchair nanoribbon shows consistent in current over wide range of applied voltage. Similar results are reported for current with respect to bias voltage in other monolayer structures [166], [167].

Optical absorption coefficient in the presence of NH_3 molecule is also calculated and compared with the absorption coefficient of pristine monolayer. The optical absorption coefficient of $\text{Ge}_{0.25}\text{Sn}_{0.25}\text{Si}_{0.5}$, $\text{Si}_{0.25}\text{Ge}_{0.25}\text{Sn}_{0.5}$ and $\text{Sn}_{0.25}\text{Si}_{0.25}\text{Ge}_{0.5}$ monolayer in the presence of NH_3 and in pristine 2D form is shown in Figure 4.21 for perpendicular and parallel polarization of incident light. In the presence of NH_3 molecule absorption coefficient of the monolayers increase significantly which can be a signifying attribute with difference in conductance to identify the presence of NH_3 molecules on the monolayers.

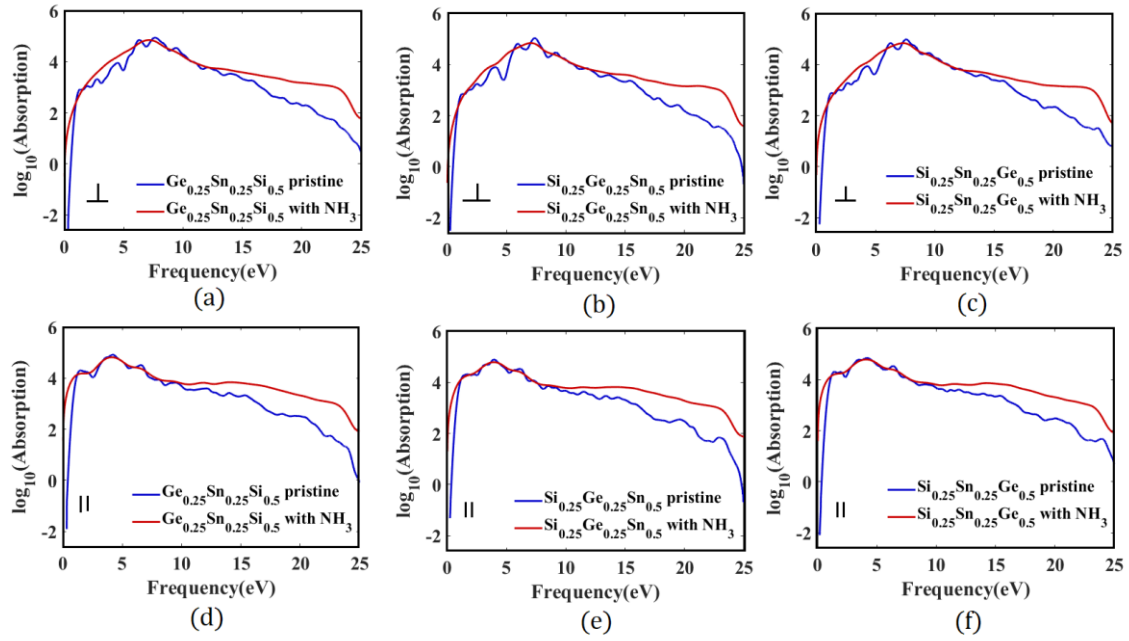


Figure 4.21: Optical absorption in log scale of (a) $\text{Ge}_{0.25}\text{Sn}_{0.25}\text{Si}_{0.5}$, (b) $\text{Si}_{0.25}\text{Ge}_{0.25}\text{Sn}_{0.5}$, (c) $\text{Sn}_{0.25}\text{Si}_{0.25}\text{Ge}_{0.5}$ monolayer for perpendicular polarization and (d) $\text{Ge}_{0.25}\text{Sn}_{0.25}\text{Si}_{0.5}$, (e) $\text{Si}_{0.25}\text{Ge}_{0.25}\text{Sn}_{0.5}$, (f) $\text{Sn}_{0.25}\text{Si}_{0.25}\text{Ge}_{0.5}$ monolayer for parallel polarization of incident light.

4.5.2 Effects of Point Defect

In order to understand the effect of point defects on electron transport properties, point vacancies on the nanoribbons are considered. The top and side views of the relaxed structures of the armchair nanoribbons of $\text{Ge}_{0.25}\text{Sn}_{0.25}\text{Si}_{0.5}$, $\text{Si}_{0.25}\text{Ge}_{0.25}\text{Sn}_{0.5}$, and $\text{Sn}_{0.25}\text{Si}_{0.25}\text{Ge}_{0.5}$ monolayers with point vacancies are shown in Figure 4.22(a), (b) and (c), respectively. To study the electron transport characteristics of the nanoribbons with and

without point vacancy a bias voltage from 0 V to 1 V is applied and the resulting current-voltage (I-V) characteristics of the $\text{Ge}_{0.25}\text{Sn}_{0.25}\text{Si}_{0.50}$, $\text{Si}_{0.25}\text{Ge}_{0.25}\text{Sn}_{0.50}$ and

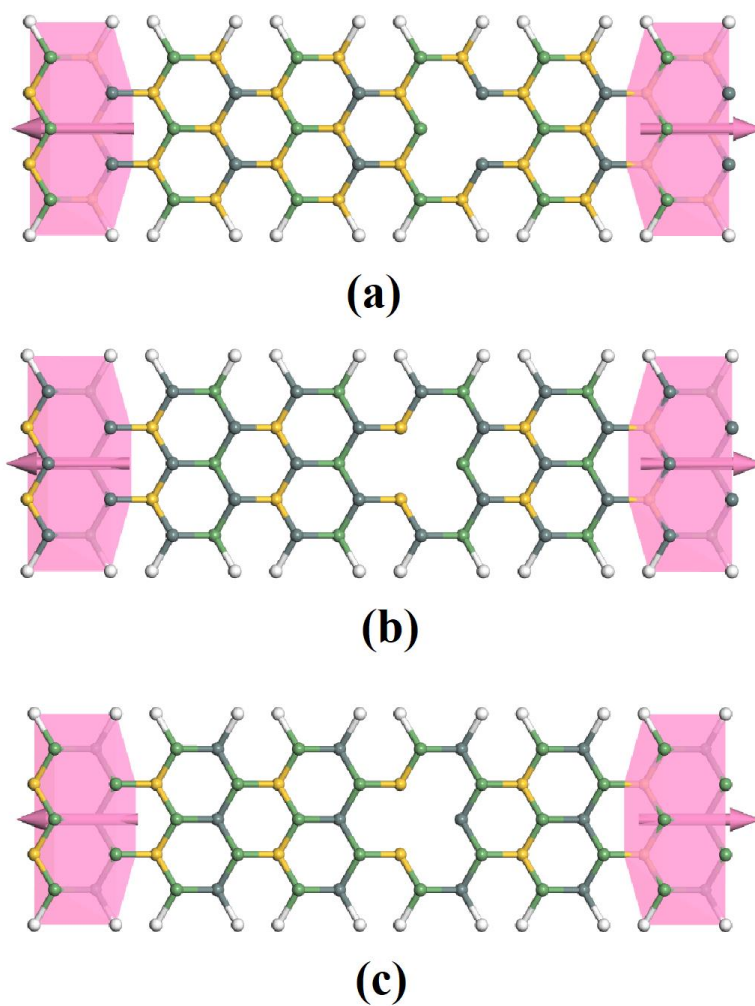


Figure 4.22: (a) $\text{Ge}_{0.25}\text{Sn}_{0.25}\text{Si}_{0.50}$, (b) $\text{Si}_{0.25}\text{Ge}_{0.25}\text{Sn}_{0.50}$, (c) $\text{Sn}_{0.25}\text{Si}_{0.25}\text{Ge}_{0.50}$ electron transport devices

$\text{Sn}_{0.25}\text{Si}_{0.25}\text{Ge}_{0.50}$ armchair nanoribbons with and without point vacancy are calculated and shown in Figure 4.23(a), (b) and (c), respectively. In the presence of point vacancies (without NH_3 molecules), the value of current in armchair nanoribbons is lower than that of the pristine nanoribbon. The difference in the value of currents can be understood by studying the transmission function as shown in Figure 4.23(d), (e) and (f), respectively of the hybrid monolayers [163] with and without defects. Similar aspects have been studied in other literatures [166], [167].

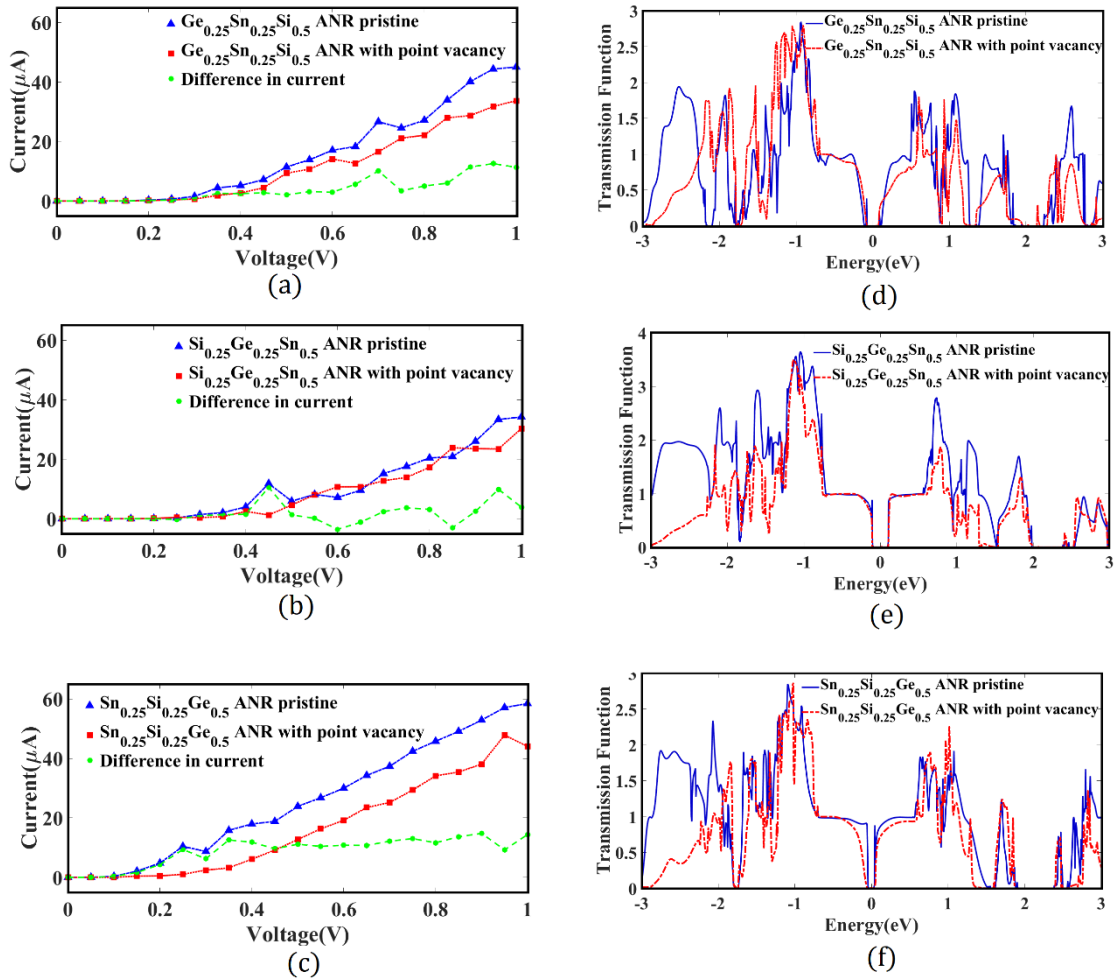


Figure 4.23: I-V characteristics of (a) $\text{Ge}_{0.25}\text{Sn}_{0.25}\text{Si}_{0.50}$, (b) $\text{Si}_{0.25}\text{Ge}_{0.25}\text{Sn}_{0.50}$, (c) $\text{Sn}_{0.25}\text{Si}_{0.25}\text{Ge}_{0.50}$ ANR; , and Transmission Function of (d) $\text{Ge}_{0.25}\text{Sn}_{0.25}\text{Si}_{0.50}$, (e) $\text{Si}_{0.25}\text{Ge}_{0.25}\text{Sn}_{0.50}$, (f) $\text{Sn}_{0.25}\text{Si}_{0.25}\text{Ge}_{0.50}$ electron transport device pristine (blue) and with point defect (red).

CHAPTER 5

Conclusion

5.1 Summary

In summary, three different novel hybrid monolayers of Si, Ge and Sn atoms have been modeled and their structural, electronic, optical and electron transport characteristics have been characterized using first principles calculations. All of the proposed hybrid monolayers are mechanically and dynamically stable which are examined by studying in-plane elastic constants, phonon dispersion curves, and cohesive energy. These atomically thin novel alloys are semiconductor materials having direct energy bandgap ranging from 120 meV to 283.8 meV due to breaking of inversion symmetry and spin-orbital interaction and also preserves linear energy-momentum relation around K point of the BZ. The effective mass of the charge carriers inside the hybrid monolayers are very low ranging from $0.063 \times m_0$ to $0.101 \times m_0$, where m_0 is the rest mass of the electron. And the computed acoustic phonon limited mobility of the charge carriers is very high ($\sim 10^5 \text{ cm}^2\text{V}^{-1}\text{s}^{-1}$) in these materials. Study of the atom projected density of states and differential charge density ensures the presence of sp^2 - sp^3 orbital hybridization due to the charge transfer within the atomic structure. Investigation of the optical properties of the hybrid monolayers demonstrate remarkable characteristics. Thorough study of these materials indicates the presence of tunable plasma frequency, high optical absorption ($\sim 10^4 \text{ cm}^{-1}$) over wide range frequency, high refractive indices (~ 1.8) from visible to UV and birefringence characteristics etc. The study of the electron transport characteristics of the proposed hybrid nanoribbons confirm the semiconducting property of the monolayers and also show the potential application of these nanoribbons as the sensors of NH_3 molecules. Transport characteristics of these materials in the presence of point defects was also carried out to understand the effect of imperfections of the nanoribbons. With such extra-ordinary characteristics, these stable forms of 2D hybrid monolayers of Si, Ge and Sn atoms would be a potential addition in the field of nanoscaled electronics, optoelectronics and sensing applications.

5.2 Scope for Future Works

This thesis provides an insight on the structural, electronic, optical, and electron transport properties of novel hybrid monolayers of Si, Ge, Sn atoms. This study can certainly facilitate further study about such atomically thin novel materials. In the following part, some suggestions for future work are presented:

- Future studies may include thermal and mechanical characterization of such hybrid monolayers of Si, Ge, and Sn atoms based on Molecular Dynamics
- The outcome of external effects, such as, strain, electric field, forming heterostructures, functionalization with molecules, doping, defect engineering can be studied to modulate the electronic and optical properties of these monolayers.
- In this study, optical properties are studied and understood in detail. Some key optical properties can be utilized to design novel devices, such as, plasmonic resonance characteristics can be exploited to design sensors, plasmonic waveguides. Anisotropic optical response can be utilized to design polarized optical filter etc. Optical properties of other atomically thin materials can be modulated by making bilayer or multilayer heterostructures with these monolayers.
- Electron transport characteristics are calculated in this thesis using ideal contacts. In future various real contacts such as Au, Pt etc. can be considered and the electron transport properties can be calculated.

List of References

- [1] Cao, Wei, et al. "2-D layered materials for next-generation electronics: Opportunities and challenges." *IEEE Transactions on Electron Devices* 65.10 (2018): 4109-4121.
- [2] Ling, Zhi Peng. "Two-Dimensional (2D) Materials for Next-Generation Nanoelectronics and Optoelectronics: Advances and Trends." *Advances in Optoelectronic Materials* (2021): 65-96.
- [3] Marani, Roberto, and Anna Gina Perri. "The next generation of FETs: CNTFETs." *arXiv preprint arXiv:1511.01356* (2015).
- [4] Mack, Chris A. "Fifty years of Moore's law." *IEEE Transactions on semiconductor manufacturing* 24.2 (2011): 202-207.
- [5] Mamaluy, Denis, and Xujiao Gao. "The fundamental downscaling limit of field effect transistors." *Applied Physics Letters* 106.19 (2015): 193503.
- [6] Schwierz, Frank, Hei Wong, and Juin J. Liou, eds. *Nanometer CMOS*. Pan Stanford Publishing, 2010.
- [7] Schwierz, Frank, and Juin J. Liou. *Modern microwave transistors: theory, design, and performance*. Wiley-Interscience, 2003.
- [8] Schwierz, Frank, and Juin J. Liou. "RF transistors: Recent developments and roadmap toward terahertz applications." *Solid-State Electronics* 51, no. 8 (2007): 1079-1091.
- [9] Taur, Yuan, and Tak H. Ning. *Fundamentals of modern VLSI devices*. Vol. Cambridge: Cambridge University Press, 1998.
- [10] Wilk, Glen D., Robert M. Wallace, and J. M. Anthony. "High- κ gate dielectrics: Current status and materials properties considerations." *Journal of applied physics* 89, no. 10 (2001): 5243-5275.
- [11] Ferain, Isabelle, Cynthia A. Colinge, and Jean-Pierre Colinge. "Multigate transistors as the future of classical metal-oxide-semiconductor field-effect transistors." *Nature* 479, no. 7373 (2011): 310-316.
- [12] Ravindran, Ajith, et al. "Gate all around nanowire TFET with high ON/OFF current ratio." *Materials Today: Proceedings* 4.9 (2017): 10637-10642.
- [13] Pandey, Deepak K. *Study of novel materials for nanoelectronics: A scanning probe microscope study of graphene and graphite oxide*. Diss. Purdue University, 2010.

- [14] Sun, Z., & Chang, H. (2014). Graphene and graphene-like two-dimensional materials in photodetection: mechanisms and methodology. *ACS nano*, 8(5), 4133-4156.
- [15] Ferrari, A. C., Bonaccorso, F., Fal'Ko, V., Novoselov, K. S., Roche, S., Bøggild, P., ... & Kinaret, J. (2015). Science and technology roadmap for graphene, related two-dimensional crystals, and hybrid systems. *Nanoscale*, 7(11), 4598-4810.
- [16] C.J. McClellan, S.V. Suryavanshi, C.D. English, K.K.H. Smithe, C.S. Bailey, R.W. Grady, E. Pop, "2D Device Trends," Accessed on: 01/07/2022. [Online]
- [17] Atabaki, Amir H., et al. "Integrating photonics with silicon nanoelectronics for the next generation of systems on a chip." *Nature* 556.7701 (2018): 349-354.
- [18] Aly, Mohamed M. Sabry, et al. "Energy-efficient abundant-data computing: The N3XT 1,000 x." *Computer* 48.12 (2015): 24-33.
- [19] Tang, Yanhao, and Kin Fai Mak. "2D materials for silicon photonics." *Nature nanotechnology* 12.12 (2017): 1121-1122.
- [20] Tang, Q., & Zhou, Z. (2013). Graphene-analogous low-dimensional materials. *Progress in materials science*, 58(8), 1244-1315.
- [21] Voon, L. L. Y., & Guzmán-Verri, G. G. (2014). Is silicene the next graphene?. *MRS bulletin*, 39(4), 366-373.
- [22] Taghioskoui, Mazdak. "Trends in graphene research." *Materials today* 12.10 (2009): 34-37.
- [23] Novoselov, K. S., et al. "Electronic properties of graphene." *physica status solidi (b)* 244.11 (2007): 4106-4111.
- [24] Guo, Shiyang, et al. "Ultrathin tellurium dioxide: emerging direct bandgap semiconductor with high-mobility transport anisotropy." *Nanoscale* 10.18 (2018): 8397-8403.
- [25] Zhang, Q. Q., Jia, P. Z., Chen, X. K., Zhou, W. X., & Chen, K. Q. (2020). Thermal transport properties in monolayer group-IV binary compounds. *Journal of Physics: Condensed Matter*, 32(30), 305301.
- [26] Xu, Z., Li, Y., & Liu, Z. (2016). First-principles calculations of structural, electronic, and thermodynamic properties of monolayer Si_{1-x}Ge_xC sheet. *RSC advances*, 6(115), 113903-113910.
- [27] Timofeev, V. A., Nikiforov, A. I., Tuktamyshev, A. R., Mashanov, V. I., Loshkarev, I. D., Bloshkin, A. A., & Gutakovskii, A. K. (2018). Pseudomorphic GeSiSn, SiSn and Ge layers in strained heterostructures. *Nanotechnology*, 29(15), 154002.

- [28] Novoselov, Kostya S., et al. "Two-dimensional gas of massless Dirac fermions in graphene." *nature* 438.7065 (2005): 197-200.
- [29] Geim, Andre Konstantin. "Graphene: status and prospects." *science* 324.5934 (2009): 1530-1534.
- [30] Song, Li, et al. "Large scale growth and characterization of atomic hexagonal boron nitride layers." *Nano letters* 10.8 (2010): 3209-3215.
- [31] Chen, Xianping, et al. "The electronic and optical properties of novel germanene and antimonene heterostructures." *Journal of Materials Chemistry C* 4.23 (2016): 5434-5441.
- [32] Banerjee, Sanjay K., et al. "Graphene for CMOS and beyond CMOS applications." *Proceedings of the IEEE* 98.12 (2010): 2032-2046.
- [33] Pereira, Vitor M., and AH Castro Neto. "Strain engineering of graphene's electronic structure." *Physical Review Letters* 103.4 (2009): 046801.
- [34] Zhong, Xiaoliang, et al. "First-principles study of strain-induced modulation of energy gaps of graphene/BN and BN bilayers." *Physical review B* 83.19 (2011): 193403.
- [35] Novoselov, K. S., Geim, A. K., Morozov, S. V., Jiang, D. E., Zhang, Y., Dubonos, S. V., ... & Firsov, A. A. (2004). Electric field effect in atomically thin carbon films. *science*, 306(5696), 666-669.
- [36] Ahmed, Touhid, Abhijit Biswas, and Samia Subrina. "Enhanced Performance of Strained Graphene Wrapped Channel Cylindrical FET." *2021 IEEE Region 10 Symposium (TENSYMP)*. IEEE, 2021.
- [37] Ioniță, Mariana, et al. "Graphene and functionalized graphene: Extraordinary prospects for nanobiocomposite materials." *Composites Part B: Engineering* 121 (2017): 34-57.
- [38] Lemme, M. C., Echtermeyer, T. J., Baus, M., & Kurz, H. (2007). A graphene field-effect device. *IEEE Electron Device Letters*, 28(4), 282-284.
- [39] Han, Melinda Y., Barbaros Özyilmaz, Yuanbo Zhang, and Philip Kim. "Energy band-gap engineering of graphene nanoribbons." *Physical review letters* 98, no. 20 (2007): 206805..
- [40] Evaldsson, Martin, Igor V. Zozoulenko, Hengyi Xu, and T. Heinzl. "Edgedisorder-induced Anderson localization and conduction gap in graphene nanoribbons." *Physical Review B* 78, no. 16 (2008): 161407.66

- [41] Cervantes-Sodi, F., G. Csanyi, S. Piscanec, and A. C. Ferrari. "Edge functionalized and substitutionally doped graphene nanoribbons: Electronic and spin properties." *Physical Review B* 77, no. 16 (2008): 165427.
- [42] Castro, Eduardo V., K. S. Novoselov, S. V. Morozov, N. M. R. Peres, JMB Lopes Dos Santos, Johan Nilsson, F. Guinea, A. K. Geim, and AH Castro Neto. "Biased bilayer graphene: semiconductor with a gap tunable by the electric field effect." *Physical Review Letters* 99, no. 21 (2007): 216802.
- [43] Gava, Paola, Michele Lazzeri, A. Marco Saitta, and Francesco Mauri. "Ab initio study of gap opening and screening effects in gated bilayer graphene." *Physical Review B* 79, no. 16 (2009): 165431.
- [44] Ohta, Taisuke, Aaron Bostwick, Thomas Seyller, Karsten Horn, and Eli Rotenberg. "Controlling the electronic structure of bilayer graphene." *Science* 313, no. 5789 (2006): 951954.
- [45] Zhang, Yuanbo, Tsung-Ta Tang, Caglar Girit, Zhao Hao, Michael C. Martin, Alex Zettl, Michael F. Crommie, Y. Ron Shen, and Feng Wang. "Direct observation of a widely tunable bandgap in bilayer graphene." *Nature* 459, no. 7248 (2009): 820-823.
- [46] Rotenberg, Eli, Aaron Bostwick, Taisuke Ohta, Jessica L. McChesney, Thomas Seyller, and Karsten Horn. "Origin of the energy bandgap in epitaxial graphene." *Nature materials* 7, no. 4 (2008): 258-259.
- [47] Zhou, S. Y., G-H. Gweon, A. V. Fedorov, P. N. First, W. A. De Heer, D-H. Lee, F. Guinea, AH Castro Neto, and A. Lanzara. "Substrate-induced bandgap opening in epitaxial graphene." *Nature materials* 6, no. 10 (2007): 770-775..
- [48] Bostwick, Aaron, Taisuke Ohta, Thomas Seyller, Karsten Horn, and Eli Rotenberg. "Quasiparticle dynamics in graphene." *Nature Physics* 3, no. 1 (2006): 36-40.
- [49] Peng, Xiangyang, and Rajeev Ahuja. "Symmetry breaking induced bandgap in epitaxial graphene layers on SiC." *Nano letters* 8, no. 12 (2008): 4464-4468
- [50] Nourbakhsh, Amirhasan, et al. "Bandgap opening in oxygen plasma-treated graphene." *Nanotechnology* 21.43 (2010): 435203.
- [51] Xu, Xiaozhi, et al. "Interfacial engineering in graphene bandgap." *Chemical Society Reviews* 47.9 (2018): 3059-3099.
- [52] Guan, Zhaoyong, Shuang Ni, and Shuanglin Hu. "Band gap opening of graphene by forming a graphene/PtSe₂ van der Waals heterojunction." *RSC advances* 7.72 (2017): 45393-45399.

- [53] Raza, Hassan, and Edwin C. Kan. "Armchair graphene nanoribbons: Electronic structure and electric-field modulation." *Physical Review B* 77.24 (2008): 245434.
- [54] Wang, Shuiyuan, et al. "Two-dimensional ferroelectric channel transistors integrating ultra-fast memory and neural computing." *Nature Communications* 12.1 (2021): 1-9.
- [55] Ren, Hao, et al. "Graphene nanoribbon as a negative differential resistance device." *Applied Physics Letters* 94.17 (2009): 173110.
- [56] Martins, Thiago B., et al. " σ -and π -Defects at graphene nanoribbon edges: building spin filters." *Nano letters* 8.8 (2008): 2293-2298.
- [57] Yang, Jian-Fei, et al. "Bias-Controlled Giant Magnetoresistance through Cyclopentadienyl–Iron Multidecker Molecules." *The Journal of Physical Chemistry C* 116.37 (2012): 19996-20001.
- [58] Sugawara, Tadashi, and Michio M. Matsushita. "Spintronics in organic π -electronic systems." *Journal of Materials Chemistry* 19.12 (2009): 1738-1753.
- [59] Zhai, Xin-Ping, et al. "2D materials towards ultrafast photonic applications." *Physical Chemistry Chemical Physics* 22.39 (2020): 22140-22156.
- [60] Cheng, Jinbing, et al. "Recent advances in optoelectronic devices based on 2D materials and their heterostructures." *Advanced Optical Materials* 7.1 (2019): 1800441.
- [61] Yu, Zhihao, et al. "Analyzing the carrier mobility in transition-metal dichalcogenide MoS₂ field-effect transistors." *Advanced Functional Materials* 27.19 (2017): 1604093.
- [62] Li, Xuemei, et al. "Large area hexagonal boron nitride monolayer as efficient atomically thick insulating coating against friction and oxidation." *Nanotechnology* 25.10 (2014): 105701.
- [63] Sorkin, V., and Y. W. Zhang. "The deformation and failure behaviour of phosphorene nanoribbons under uniaxial tensile strain." *2D Materials* 2.3 (2015): 035007.
- [64] Lalmi, B., Oughaddou, H., Enriquez, H., Kara, A., Vizzini, S., Ealet, B., & Aufray, B. (2010). Epitaxial growth of a silicene sheet. *Applied Physics Letters*, 97(22), 223109.
- [65] Friedlein, R., & Yamada-Takamura, Y. (2015). Electronic properties of epitaxial silicene on diboride thin films. *Journal of Physics: Condensed Matter*, 27(20), 203201.
- [66] Liu, Z. L., Wang, M. X., Xu, J. P., Ge, J. F., Le Lay, G., Vogt, P., ... & Jia, J. F. (2014). Various atomic structures of monolayer silicene fabricated on Ag (111). *New Journal of Physics*, 16(7), 075006.

- [67] Bianco, E., Butler, S., Jiang, S., Restrepo, O. D., Windl, W., & Goldberger, J. E. (2013). Stability and exfoliation of germanane: a germanium graphane analogue. *ACS nano*, 7(5), 4414-4421.
- [68] Zhu, F. F., Chen, W. J., Xu, Y., Gao, C. L., Guan, D. D., Liu, C. H., ... & Jia, J. F. (2015). Epitaxial growth of two-dimensional stanene. *Nature materials*, 14(10), 1020-1025.
- [69] Balendhran, S., Walia, S., Nili, H., Sriram, S., & Bhaskaran, M. (2015). Elemental analogues of graphene: silicene, germanene, stanene, and phosphorene. *small*, 11(6), 640-652.
- [70] Ahmed, T., Sakib, H., & Subrina, S. (2019). SiGe/AsSb bilayer heterostructures: structural characteristics and tunable electronic properties. *Nanotechnology*, 31(3), 035701.
- [71] Sakib, H., Ahmed, T., & Subrina, S. (2018, December). Uniaxial strain on monolayer SiGe: Strain tunable electronic properties. In *2018 10th International Conference on Electrical*
- [72] Zhang, Q. Q., Jia, P. Z., Chen, X. K., Zhou, W. X., & Chen, K. Q. (2020). Thermal transport properties in monolayer group-IV binary compounds. *Journal of Physics: Condensed Matter*, 32(30), 305301.
- [73] Xu, Z., Li, Y., & Liu, Z. (2016). First-principles calculations of structural, electronic, and thermodynamic properties of monolayer Si_{1-x}Ge_xC sheet. *RSC advances*, 6(115), 113903-113910.
- [74] Kim, Hyungjin, et al. "Inhibited nonradiative decay at all exciton densities in monolayer semiconductors." *Science* 373.6553 (2021): 448-452.
- [75] Shim, Jiwook, et al. "Detection of methylation on dsDNA using nanopores in a MoS₂ membrane." *Nanoscale* 9.39 (2017): 14836-14845.
- [76] Tamersit, Khalil, and Fayçal Djeflal. "Double-gate graphene nanoribbon field-effect transistor for DNA and gas sensing applications: simulation study and sensitivity analysis." *IEEE Sensors Journal* 16.11 (2016): 4180-4191.
- [77] P. Hohenberg and W. Kohn, "Inhomogeneous Electron Gas," *Physical Review*, vol. 136, no. 3B, pp. B864–B871, 1964.
- [78] W. Kohn and L. J. Sham, "Self-Consistent Equations Including Exchange and Correlation Effects," *Physical Review*, vol. 140, no. 4A, pp. A1133–A1138, 1965.

- [79] J. P. Perdew and Y. Wang, "Accurate and simple analytic representation of the electron-gas correlation energy," *Physical Review B*, vol. 45, no. 23, pp. 13244–13249, 1992.
- [80] J. P. Perdew, K. Burke, and Y. Wang, "Generalized gradient approximation for the exchange–correlation hole of a many-electron system," *Physical Review B*, vol. 54, no. 23, pp. 16533–16539, 1996.
- [81] J. P. Perdew, K. Burke, and M. Ernzerhof, "Generalized Gradient Approximation Made Simple," *Physical Review Letters*, vol. 77, no. 18, pp. 3865–3868, 1996.
- [82] C. Lee, W. Yang, and R. G. Parr, "Development of the Colle-Salvetti correlation-energy formula into a functional of the electron density," *Physical Review B*, vol. 37, no. 2, pp. 785–789, 1988.
- [83] P. a. M. Dirac, "Note on Exchange Phenomena in the Thomas Atom," *Mathematical Proceedings of the Cambridge Philosophical Society*, vol. 26, no. 3, pp. 376–385, 1930.
- [84] D. M. Ceperley and B. J. Alder, "Ground State of the Electron Gas by a Stochastic Method," *Physical Review Letters*, vol. 45, no. 7, pp. 566–569, 1980.
- [85] S. H. Vosko, L. Wilk, and M. Nusair, "Accurate spin-dependent electron liquid correlation energies for local spin density calculations: a critical analysis," *Canadian Journal of Physics*, vol. 58, no. 8, pp. 1200–1211, 1980.
- [86] A. St.-Amant, W. D. Cornell, P. A. Kollman, and T. A. Halgren, "Calculation of molecular geometries, relative conformational energies, dipole moments, and molecular electrostatic potential fitted charges of small organic molecules of biochemical interest by density functional theory," *Journal of Computational Chemistry*, vol. 16, no. 12, pp. 1483–1506, 1995.
- [87] Heyd, Jochen, and Gustavo E. Scuseria. "Efficient hybrid density functional calculations in solids: Assessment of the Heyd–Scuseria–Ernzerhof screened Coulomb hybrid functional." *The Journal of chemical physics* 121.3 (2004): 1187-1192.
- [88] Salomon, Oliver, Markus Reiher, and Bernd Artur Hess. "Assertion and validation of the performance of the B3LYP* functional for the first transition metal row and the G2 test set." *The Journal of chemical physics* 117.10 (2002): 4729-4737.
- [89] Adamo, Carlo, and Vincenzo Barone. "Toward reliable density functional methods without adjustable parameters: The PBE0 model." *The Journal of chemical physics* 110.13 (1999): 6158-6170.

- [90] L. Kleinman and J. C. Phillips, "Crystal Potential and Energy Bands of Semiconductors. II. Self-Consistent Calculations for Cubic Boron Nitride," *Physical Review*, vol. 117, no. 2, pp. 460–464, 1960.
- [91] D. R. Hamann, M. Schlüter, and C. Chiang, "Norm-Conserving Pseudopotentials," *Physical Review Letters*, vol. 43, no. 20, pp. 1494–1497, 1979.
- [92] Feynman, Richard Phillips. "Forces in molecules." *Physical review* 56.4 (1939): 340.
- [93] J. Bardeen and W. Shockley, "Deformation Potentials and Mobilities in Non-Polar Crystals," *Physical Review*, vol. 80, no. 1, pp. 72-80, Oct 1950.
- [94] C. Herring and E. Vogt, "Transport and Deformation-Potential Theory for Many-Valley Semiconductors with Anisotropic Scattering," *Physical Review*, vol. 101, no. 3, pp. 944-961, 1956.
- [95] G. Bir and G. Pikus, *Symmetry and Strain-Induced Effects in Semiconductors*. New York - Toronto: J.Wiley & Sons, 1974.
- [96] M. Fischetti and S. Laux, "Band Structure, Deformation Potentials, and Carrier Mobility in Si, Ge, and SiGe Alloys," *J.Appl.Phys.*, vol. 80, no. 4, pp. 2234-2252, 1996.
- [97] L. P. Kadanoff and G. Baym, *Quantum Statistical Mechanics*. Benjamin, New York, 1962.
- [98] S. Datta, *Electronic Transport in Mesoscopic Systems*. Cambridge University Press, 1997.
- [99] S. Datta, *Quantum Transport: Atom to Transistor*. Cambridge University Press, 2005.
- [100] S. Datta, "The Non-equilibrium Green's Function (NEGF) Formalism: An Elementary Introduction," in Proc. Digest. International Electron Devices Meeting IEDM '02, p. 703, 2002.
- [101] S. Datta, "Nanoscale Device Modeling: The Green's Function Method," *Superlattices & Microstructures*, vol. 28, no. 4, p. 253, 2000.
- [102] Kohn, Walter, and Lu Jeu Sham. "Self-consistent equations including exchange and correlation effects." *Physical review* 140.4A (1965): A1133.
- [103] Giannozzi, Paolo, et al.. "QUANTUM ESPRESSO: a modular and open-source software project for quantum simulations of materials." *Journal of physics: Condensed matter* 21.39 (2009): 395502.
- [104] Clark, S. J., Segall, M. D., Pickard, C. J., Hasnip, P. J., Probert, M. I., Refson, K., & Payne, M. C. (2005). First principles methods using CASTEP. *Zeitschrift für Kristallographie-Crystalline Materials*, 220(5-6), 567-570.

- [105] J. P. Perdew and Y. Wang, *Phys. Rev. B: Condens. Matter Mater. Phys.*, 1992, 45, 13244.
- [106] J. P. Perdew, K. Burke and M. Ernzerhof, *Physical review letters*, 1996, 77,3865.
- [107] W. Yu, Z. Zhu, C.-Y. Niu, C. Li, J.-H. Cho, and Y. Jia, “Anomalous doping effect in black phosphorene using first-principles calculations,” *Physical Chemistry Chemical Physics*, vol. 17, no. 25, pp. 16351–16358, 2015.
- [108] J. P. Perdew and Y. Wang, “Accurate and simple analytic representation of the electron-gas correlation energy,” *Physical Review B*, vol. 45, no. 23, pp. 13244–13249, 1992.
- [109] Wu, Xiaojun, Yong Pei, and Xiao Cheng Zeng. "B2C graphene, nanotubes, and nanoribbons." *Nano letters* 9.4 (2009): 1577-1582.
- [110] John, Rita, and Benita Merlin. "Theoretical investigation of structural, electronic, and mechanical properties of two dimensional C, Si, Ge, Sn." *Crystal Structure Theory and Applications* 5.3 (2016): 43-55.
- [111] M. Methfessel and A. T. Paxton, “High-precision sampling for Brillouin-zone integration in metals,” *Physical Review B*, vol. 40, no. 6, pp. 3616–3621, 1989.
- [112] P. E. Blöchl, O. Jepsen, and O. K. Andersen, “Improved tetrahedron method for Brillouin-zone integrations,” *Physical Review B*, vol. 49, no. 23, pp. 16223–16233, 1994.
- [113] K. Momma and F. Izumi, “VESTA 3 for three-dimensional visualization of crystal, volumetric and morphology data,” *Journal of Applied Crystallography*, vol. 44, no. 6, Art. no. 6, 2011.
- [114] Shockley, W., and J. Bardeen. "Energy bands and mobilities in monatomic semiconductors." *Physical Review* 77.3 (1950): 407.
- [115] Xi, J., Long, M., Tang, L., Wang, D., & Shuai, Z. (2012). First-principles prediction of charge mobility in carbon and organic nanomaterials. *Nanoscale*, 4(15), 4348-4369.
- [116] Chen, X., Jiang, J., Liang, Q., Meng, R., Tan, C., Yang, Q., ... & Zeng, H. (2016). Tunable electronic structure and enhanced optical properties in quasi-metallic hydrogenated/fluorinated SiC heterobilayer. *Journal of Materials Chemistry C*, 4(31), 7406-7414.
- [117] Computer codeDMOL: Biosym Technologies Inc., San Diego, CA,1995.
- [118] Fadaie, M., Shahtahmassebi, N., Roknabad, M. R., & Gulseren, O. (2017). Investigation of new two-dimensional materials derived from stanene. *Computational Materials Science*, 137, 208-214.

- [119] Jamdagni, Pooja, *et al.*. "Stability and electronic properties of SiGe-based 2D layered structures." *Materials Research Express* 2.1 (2015): 016301.
- [120] Yu, Wen-Zhe, Jia-An Yan, and Shang-Peng Gao. "Bandgap Characters and Ferromagnetic/Antiferromagnetic Coupling in Group-IV Monolayers Tuned by Chemical Species and Hydrogen Adsorption Configurations." *Nanoscale research letters* 10.1 (2015): 351.
- [121] Zhou, Hongcai, *et al.*. "First-principles prediction of a new Dirac-fermion material: silicon germanide monolayer." *Journal of Physics: Condensed Matter* 25.39 (2013): 395501.
- [122] Ezawa, M. (2013). Spin valleytronics in silicene: Quantum spin Hall–quantum anomalous Hall insulators and single-valley semimetals. *Physical Review B*, 87(15), 155415.
- [123] Tan, J., Chen, K., & Tang, L. M. (2019). Out-of-plane spontaneous polarization and superior photoelectricity in two-dimensional SiSn. *Journal of Physics: Condensed Matter*, 32(6), 065003.
- [124] Tao, Lele, *et al.* "Tension-induced mechanical properties of stanene." *Modern Physics Letters B* 30.12 (2016): 1650146.
- [125] Mortazavi, Bohayra, *et al.* "First-principles investigation of mechanical properties of silicene, germanene and stanene." *Physica E: Low-dimensional Systems and Nanostructures* 87 (2017): 228-232.
- [126] Yao, C. J., Huang, H. F., Yao, Y., Wu, Y. Z., & Hao, X. (2021). Coexistence of polar distortion and conduction in doped 2D group-IV ferroelectrics: SiGe, SiSn, and GeSn. *Journal of Physics: Condensed Matter*, 33(14), 145302.
- [127] Naseri, M. (2018). Investigation on the stability and electronic properties of Penta-XP5 (X= Al, Ga, In) monolayer semiconductors by using first principles calculations. *Chemical Physics Letters*, 706, 99-106.
- [128] Xue, H., Gao, F., Yu, Y., Chong, Y., Shvets, G., & Zhang, B. (2018). Spin-valley-controlled photonic topological insulator. *arXiv preprint arXiv:1811.00393*.
- [129] Liu, C. C., Jiang, H., & Yao, Y. (2011). Low-energy effective Hamiltonian involving spin-orbit coupling in silicene and two-dimensional germanium and tin. *Physical Review B*, 84(19), 195430.
- [130] Khan, Asir Intisar, *et al.*. "Stanene-hexagonal boron nitride heterobilayer: Structure and characterization of electronic property." *Scientific reports* 7.1 (2017): 16347.

- [131] Zhao, Jijun, *et al.*. "Rise of silicene: A competitive 2D material." *Progress in Materials Science* 83 (2016): 24-151.
- [132] Shao, Zhi-Gang, *et al.* "First-principles calculation of intrinsic carrier mobility of silicene." *Journal of Applied Physics* 114.9 (2013): 093712.
- [133] Tao, Li, *et al.* "Silicene field-effect transistors operating at room temperature." *Nature nanotechnology* 10.3 (2015): 227-231.
- [134] Zhang, Qingyun, and Udo Schwingenschlögl. "Emergence of Dirac and quantum spin Hall states in fluorinated monolayer As and AsSb." *Physical Review B* 93.4 (2016): 045312.
- [135] Jin, Cui, *et al.*. "Modulation of silicene properties by AsSb with van der Waals interaction." *RSC Advances* 7.10 (2017): 5827-5835.
- [136] Shi, Jing, *et al.* "Electronic, elastic and piezoelectric properties of two-dimensional group-IV buckled monolayers." *Chinese Physics Letters* 34.8 (2017): 087701.
- [137] Song, Z., Liu, C. C., Yang, J., Han, J., Ye, M., Fu, B., ... & Yao, Y. (2014). Quantum spin Hall insulators and quantum valley Hall insulators of BiX/SbX (X= H, F, Cl and Br) monolayers with a record bulk bandgap. *NPG Asia Materials*, 6(12), e147-e147.
- [138] Klimovskikh, I. I., Otrokov, M. M., Voroshnin, V. Y., Sostina, D., Petaccia, L., Di Santo, G., ... & Shikin, A. M. (2017). Spin-orbit coupling induced gap in graphene on Pt (111) with intercalated Pb monolayer. *ACS nano*, 11(1), 368-374.
- [139] Zhou, S. Yi, *et al.*. "Substrate-induced bandgap opening in epitaxial graphene." *Nature materials* 6.10 (2007): 770.
- [140] Ni, Z., Liu, Q., Tang, K., Zheng, J., Zhou, J., Qin, R., ... & Lu, J. (2012). Tunable bandgap in silicene and germanene. *Nano letters*, 12(1), 113-118.
- [141] Chow, W. L., Yu, P., Liu, F., Hong, J., Wang, X., Zeng, Q., ... & Liu, Z. (2017). High mobility 2D palladium diselenide field-effect transistors with tunable ambipolar characteristics. *Advanced Materials*, 29(21), 1602969.
- [142] Fang, Hui, *et al.*. "High-performance single layered WSe₂ p-FETs with chemically doped contacts." *Nano letters* 12.7 (2012): 3788-3792.
- [143] Peng, Xihong, Qun Wei, and Andrew Copple. "Strain-engineered direct-indirect bandgap transition and its mechanism in two-dimensional phosphorene." *Physical Review B* 90.8 (2014): 085402.
- [144] Zhou, D., Zheng, Y., Pu, C., Wang, Z., & Tang, X. (2018). Computational Prediction to Two-Dimensional SnAs. *Chinese Physics Letters*, 35(10), 107101.

- [145] Chen, Xianping, *et al.*. "The electronic and optical properties of novel germanene and antimonene heterostructures." *Journal of Materials Chemistry C* 4.23 (2016): 5434-5441.
- [146] Nigam, Sandeep, *et al.*. "Modulation of bandgap by an applied electric field in silicene-based hetero-bilayers." *Physical Chemistry Chemical Physics* 17.17 (2015): 11324-11328.
- [147] Li, Sheng-shi, *et al.*. "Tunable electronic properties induced by a defect-substrate in graphene/BC 3 heterobilayers." *Physical Chemistry Chemical Physics* 16.41 (2014): 22861-22866.
- [148] Li, Xinru, *et al.*. "Intriguing electronic properties of two-dimensional MoS₂/TM₂CO₂ (TM= Ti, Zr, or Hf) hetero-bilayers: type-II semiconductors with tunable bandgaps." *Nanotechnology* 26.13 (2015): 135703.
- [149] John, R., & Merlin, B. (2017). Optical properties of graphene, silicene, germanene, and stanene from IR to far UV—A first principles study. *Journal of Physics and Chemistry of Solids*, 110, 307-315.
- [150] Boochani, A., Akhtar, A., Amiri, M., Luna, C., Rai, D. P., Bashiri, S., ... & Elahi, S. M. (2017). Effects of hydrogen and nitrogen impurities on electronic, structural and optical properties of 2D ZnS graphene based. *Journal of Materials Science*, 52(17), 10393-10405.
- [151] Lashgari, H., Boochani, A., Shekaari, A., Solaymani, S., Sartipi, E., & Mendi, R. T. (2016). Electronic and optical properties of 2D graphene-like ZnS: DFT calculations. *Applied Surface Science*, 369, 76-81.
- [152]. Matthes, L., O. Pulci, and F. Bechstedt. "Optical properties of two-dimensional honeycomb crystals graphene, silicene, germanene, and stanene from first principles." *New Journal of Physics* 16.10 (2014): 105007.
- [153] Boochani, A., Nowrozi, B., Khodadadi, J., Solaymani, S., & Jalali-Asadabadi, S. (2017). Novel graphene-like Co₂VAl (111): case study on magnetoelectronic and optical properties by first-principles calculations. *The Journal of Physical Chemistry C*, 121(7), 3978-3986.
- [154] Gómez-Díaz, J. S., & Perruisseau-Carrier, J. (2013). Graphene-based plasmonic switches at near infrared frequencies. *Optics express*, 21(13), 15490-15504.
- [155] Wu, L., Guo, J., Wang, Q., Lu, S., Dai, X., Xiang, Y., & Fan, D. (2017). Sensitivity enhancement by using few-layer black phosphorus-graphene/TMDCs heterostructure in surface plasmon resonance biochemical sensor. *Sensors and Actuators B: Chemical*, 249, 542-548.

- [156] Nourozi, B., Aminian, A., Fili, N., Zangeneh, Y., Boochani, A., & Darabi, P. (2019). The electronic and optical properties of MgO mono-layer: Based on GGA-mBJ. *Results in Physics*, 12, 2038-2043.
- [157] Bouarissa, N. (2000). The effect of hydrostatic pressure on the electronic and optical properties of InP. *Solid-State Electronics*, 44(12), 2193-2198.
- [158] Yang, H., Jussila, H., Autere, A., Komsa, H. P., Ye, G., Chen, X., ... & Sun, Z. (2017). Optical waveplates based on birefringence of anisotropic two-dimensional layered materials. *Acs Photonics*, 4(12), 3023-3030.
- [159] Jung, J. W., Choi, H. S., Lee, T., Lee, Y. J., Hong, S. H., Kang, J. W., & Cho, C. H. (2021). Polarization-controlled amplified spontaneous emission in 2D semiconductors with birefringent microcavity. *Applied Physics Letters*, 119(14), 143101.
- [160] Yeganeh, M., Saraf, H. H., Kafi, F., & Boochani, A. (2020). First principles investigation of vibrational, electronic and optical properties of graphene-like boron carbide. *Solid State Communications*, 305, 113750.
- [161] Sarmazdeh, M. M., Mendi, R. T., Zelati, A., Boochani, A., & Nofeli, F. (2016). First-principles study of optical properties of InN nanosheet. *International Journal of Modern Physics B*, 30(19), 1650117.
- [162] Bechstedt, Friedhelm, et al. "Optical properties of silicene and related materials from first principles." *Silicene*. Springer, Cham, 2018. 73-98.
- [163] Singh, S., De Sarkar, A., Singh, B., & Kaur, I. (2017). Electronic and transport behavior of doped armchair silicene nanoribbons exhibiting negative differential resistance and its FET performance. *RSC advances*, 7(21), 12783-12792.
- [164] Li, H., Wang, L., Liu, Q., Zheng, J., Mei, W. N., Gao, Z., ... & Lu, J. (2012). High performance silicene nanoribbon field effect transistors with current saturation. *The European Physical Journal B*, 85(8), 1-6.
- [165] Gracia-Espino, E., López-Urías, F., Terrones, H., & Terrones, M. (2016). Electron transport study on functionalized armchair graphene nanoribbons: DFT calculations. *RSC advances*, 6(26), 21954-21960.
- [166] Akbari, E., Buntat, Z., Afroozeh, A., Pourmand, S. E., Farhang, Y., & Sanati, P. (2016). Silicene and graphene nano materials in gas sensing mechanism. *RSC advances*, 6(85), 81647-81653.

[167] Iordanidou, K., Houssa, M., van den Broek, B., Pourtois, G., Afanas'ev, V. V., & Stesmans, A. (2016). Impact of point defects on the electronic and transport properties of silicene nanoribbons. *Journal of Physics: Condensed Matter*, 28(3), 035302.